FUNCTIONAL STUDIES OF STEM CELLS IN THE PARASITIC FLATWORM *SCHISTOSOMA MANSONI*

APPROVED BY THE SUPERVISORY COMMITTEE

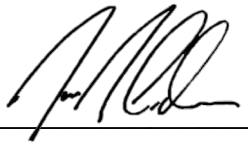

James J. Collins III, PhD

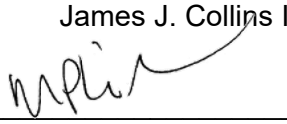

Margaret Phillips, PhD

David Mangelsdorf, PhD

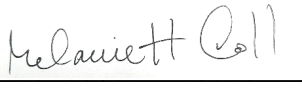

Melanie Cobb, PhD

DEDICATION

I would like to dedicate this thesis to the B.P.L. and M.O., for it was their friendship and mentorship that initially ignited my passion for science

FUNCTIONAL STUDIES OF STEM CELLS IN THE PARASITIC FLATWORM *SCHISTOSOMA MANSONI*

By

GEORGE R. WENDT

DISSERTATION

Presented to the Faculty of the Cell and Molecular Biology Graduate Program

The University of Texas Southwestern Medical Center at Dallas

In Partial Fulfillment of the Requirements

For the Degree of

DOCTOR OF PHILOSOPHY

The University of Texas Southwestern Medical Center

Dallas, Texas

December 2020

ACKNOWLEDGEMENTS

I would like to acknowledge my two families: the one I grew up with and the one I work with every day in the lab as both contributed greatly to my success as a scientist.

My parents instilled in me at an early age the importance of getting a good education so that I could have the things that they did not; namely, they hoped for me and my brother that we never ended up living in a trailer in a swamp. In retrospect, they probably thought I'd become a doctor or a lawyer or an engineer, rather than spend 7 or so years in grad school only to end up in academia. To their credit, though, they are still proud of me. My brother was by best friend growing up and he still is one of my favorite people in the world. While I decided to pursue studies in flatworm biology, he decided to go into software engineering and web development. Fortunately for me, this means that he gets to field all the tech support questions from my extended family. I will happily field any flatworm-related questions, should they arise.

My lab family has made these last five years some of the best years of my life so far. There is no other group of people I would rather work alongside. Since Jim's questionable decision to hire me back in 2015, he has proceeded to assemble a stellar team of hardworking, bright scientists who are also darned-good people, too. Indeed, all my best friends today work in the Collins lab with me, and they are likely the main reason I love this job so much. And as cliché as it is, it is true that if you find a job doing something you love, you will never work a day in your life.

FUNCTIONAL STUDIES OF STEM CELLS IN THE PARASITIC FLATWORM *SCHISTOSOMA MANSONI*

GEORGE R. WENDT

The University of Texas Southwestern Medical Center at Dallas, 2020

Supervising Professor: JAMES J. COLLINS III, PhD

Schistosomes are parasitic flatworms that infect over 200 million people, primarily in poverty-stricken developing countries, causing extensive morbidity and mortality. Schistosomes have a great deal in common with other parasitic flatworms such as liver flukes and tapeworms. Namely, they are characterized by a syncytial “skin” known as the tegument that is critical for their survival within their hosts, they possess somatic stem cells referred to as neoblasts, and they are incredibly successful parasites. Until now, there has been little appreciation for the interrelationships between the tegument, neoblasts, and successful parasitism.

Our recent work, however, suggested that schistosome neoblasts give rise to cells that are associated with the parasite’s tegument. In order to determine whether schistosome neoblasts produced the tegument, we developed novel labeling techniques and found that neoblasts give rise to progenitor cells that ultimately maintain the tegument. We also developed a fluorescence activated cell sorting protocol that we used to isolate neoblasts and tegument progenitors and obtain their transcriptomes. With this transcriptome data, we identified two regulators of tegument maintenance, *zfp-1* and *zfp-1-1*, that are functionally conserved in free-living flatworms, suggesting a common molecular program for “skin” production in all flatworms. Additionally, our

work suggested that *zfp-1-1* specifically and tegument maintenance generally may be valid therapeutic targets.

We next wondered whether schistosome neoblasts were responsible for making or maintaining any non-tegumental tissues in the adult parasite. To study this, we employed single cell RNAseq to create a gene expression atlas of 43,642 cells from adult parasites. This atlas gave us molecular markers for 68 distinct clusters of cells ranging from muscles and neurons to reproductive tissues such as the ovary. It also allowed us to identify a previously unknown sub-population of neoblasts that appears to exist at the top of a schistosome gut lineage. In an effort to study these neoblasts, we found that the schistosome homolog of the nuclear receptor *hnf4* is required for normal gut homeostasis and that loss-of-function of *hnf4* prevents parasite blood feeding and abrogates disease pathology *in vivo*.

Taken together, this work demonstrates how studying basic developmental processes (i.e. stem cell differentiation) in a pathogenic organism can lead to not only insights into evolutionary biology (the machinery that regulates skin production appears to be conserved across flatworms), but it can also suggest novel therapeutic targets (namely *zfp-1-1* and tegument maintenance as well as *hnf4* and gut homeostasis).

TABLE OF CONTENTS

PRIOR PUBLICATIONS

Collins JJ 3rd, **Wendt GR**, Iyer H, Newmark PA. Stem cell progeny contribute to the schistosome host-parasite interface. Elife. 2016;5:e12473. Published 2016 Mar 22. doi:10.7554/eLife.12473

Wendt GR, Collins JJ 3rd. Schistosomiasis as a disease of stem cells. Curr Opin Genet Dev. 2016;40:95-102. doi:10.1016/j.gde.2016.06.010

Wendt GR, Collins JN, Pei J, et al. Flatworm-specific transcriptional regulators promote the specification of tegumental progenitors in Schistosoma mansoni. Elife. 2018;7:e33221. Published 2018 Mar 20. doi:10.7554/eLife.33221

Wendt G, Collins JJ. Labeling of the Schistosoma mansoni Tegument. Methods Mol Biol. 2020;2151:65-74. doi:10.1007/978-1-0716-0635-3_6

Wendt G, Zhao L, Chen R, Liu C, O'Donoghue AJ, Caffrey CR, Reese ML, Collins JJ 3rd. A single-cell RNA-seq atlas of Schistosoma mansoni identifies a key regulator of blood feeding. Science. 2020 Sep 25;369(6511):1644-1649. doi: 10.1126/science.abb7709

LIST OF FIGURES

FIGURE 6.7: *hnf4* is required for pathology.

LIST OF ABBREVIATIONS

DALY: disability-adjust life years

NMRI: Naval Medical Research Institute

DMEM: Dulbecco's Modified Eagle Medium

RNAi: RNA interference

dsRNA: double stranded RNA

EdU: 5-Ethynyl-2'-deoxyuridine

qPCR: quantitative PCR

RNAseq: RNA sequencing

TEM: transmission electron microscopy

PBSTx: phosphate buffered saline + 0.3% triton-X100

TAMRA: 5-Carboxytetramethylrhodamine

ISH: *in situ* hybridization

FISH: fluorescence *in situ* hybridization

WISH: whole mount *in situ* hybridization

SDS PAGE: sodium dodecyl sulfate polyacrylamide gel electrophoresis

AF488: Alexa Fluor 488

FACS: fluorescence activated cell sorting

scRNAseq: single cell RNA sequencing

PCA: principal component analysis

UMAP: uniform manifold approximation and projection

CHAPTER ONE

INTRODUCTION

Schistosomiasis

Schistosomiasis is a neglected tropical disease caused by parasitic flatworms of the genus *Schistosoma.* The disease afflicts over 230 million people, predominantly in developing countries in Africa, the Middle East, and Southeast Asia [1]. Annual mortality estimates range between 20 thousand and 200 thousand [2], but the true cost of disease is probably best understood by examining its morbidity. Some studies suggest that among tropical diseases, schistosomiasis is second to malaria in terms of morbidity as measured by disability-adjust life years (DALY) [3]. These data clearly show that schistosomiasis is a dire global health problem, but serious limitations exist with respect to treatment, prevention, and elimination [4].

Treatment of schistosomiasis relies upon a single drug, praziquantel. The advantages and disadvantages of praziquantel treatment is more extensively reviewed by Cioli et al. [5], but will be summarized here for the sake of completeness. Praziquantel has many positive traits. First, it is reasonably effective with a 60-90% cure rate with a single dose of 40mg/kg and it is also efficacious against many (but not all) other parasitic flatworms. Second, it is remarkably safe, being described as “the safest of all anthelminthic drugs” by Cioli et al. It is even recommended for use in pregnant women [6]. Third, praziquantel is a relatively convenient drug that can be administered in a single dose without medical supervision. Finally, praziquantel is inexpensive, costing approximately $0.25 USD per dose [7]. In spite of these advantages, however, praziquantel has significant drawbacks. Most concerning is the possibility of the development of drug resistance. Because it is extensively used as monotherapy to treat schistosomiasis in regions with heavy transmission, and because the treatment and control of

schistosomiasis relies so heavily upon praziquantel, the emergence of resistance is a grave concern [8]. Besides resistance, praziquantel also suffers from several other drawbacks. The mechanism of action is unclear [9-11] which could hamper our ability to understand how resistance might arise and how to combat it. Additionally, praziquantel is relatively ineffective against the rapidly growing juvenile parasites found in the host's bloodstream ~28 days post-infection [12]. This lack of efficacy against juvenile parasites could have implications for praziquantel ineffectiveness in regions of high transmission where persons are likely to be constantly re-infected and therefore frequently carry insensitive juvenile schistosomes [13].

Praziquantel represents the primary therapeutic approach towards treating schistosomiasis, but what about prevention and elimination? Ultimately, this would require preventing transmission of the parasite, which could potentially be accomplished with the development of a vaccine. Efforts to combat schistosomiasis with vaccines have been review by Tebeje et al [14] but will be briefly discussed here for the sake of completeness. Multiple approaches to vaccine development have been undertaken. Attenuated vaccines (delivered via irradiated larvae) have been used in non-human primates [15], sheep [16], and cattle [17]. While these were efficacious in these model systems, there were key drawbacks including cost, storage, and safety [14, 18]. Recombinant vaccines (protein and DNA) have also been extensively studied, with over 100 vaccine candidates identified and more than 25 tested in model organisms [14]. Unfortunately, most of these vaccines have been tested in mouse models which may have intrinsic disadvantages as a model organism to study schistosome vaccines [19]. As such, future research into schistosome vaccines may require more research in non-human primates or perhaps even in human volunteers. Recent work has demonstrated that human volunteer studies can be safely carried out [20], setting the stage for further vaccine research that circumvents model organism related issues.

Other efforts to control schistosomiasis have focused on decreasing the chances of persons coming in contact with infectious larvae. One way to do this is to eliminate the snails that serve as the intermediate hosts of schistosomes. Molluscicides haven been used to this end for over 100 years [21, 22]. Though this method has been effective in many instances, there are significant concerns regarding cost and environmental impact [23-25]. Some of these issues can be circumvented by releasing other organisms (deliberately or otherwise) that either compete with or feed upon the snails required for transmission. This has been a key factor in the elimination of schistosomiasis from several countries, including many in the Caribbean such as St. Kitts and Nevis, Puerto Rico, the Dominican Republic, Guadeloupe, and Martinique [25-28]. There are significant drawbacks to biological control, however, especially when introducing non-native species [29]. Still, there is great potential for utilizing biological control, especially when the agents utilized are originally from the environment being treated [30, 31]. Besides targeting snails directly, another effective strategy has been to alter the habitats where they reside, either displacing the snails or preventing schistosome eggs from reaching the habitats where the snails reside [21, 32-34]

The intent of this section is to convey a sense of the current status of schistosomiasis and its treatment, prevention and elimination today. It is clear that, while many great strides have been made in attacking this global health scourge, much work yet remains to be done. One significant obstacle that stands in the way of schistosomiasis is our relatively poor understanding of the schistosome itself. Improving our understanding of the basic biology of the schistosome is therefore a ripe area for further investigation.

Schistosome biology

Like many other trematodes, schistosomes undergo a complex multiple host lifecycle (**Figure 1.1**). A more extensive description of the lifecycle can be found in Basch 1991 [35] but will be summarized here for completeness. Schistosome eggs hatch to give rise to the first larval stage, known as a miracidium (plural: miracidia) (**Figure 1.1A**). The miracidia is a ciliated larval stage that moves through aquatic environments in order to find a permissive snail intermediate host, namely snails of the genus *Biomphalaria*. Upon finding a suitable snail, the miracidia penetrates inside the snail where it transforms into a mother sporocyst (**Figure 1.1B**). The mother sporocyst then gives rise to daughter sporocysts which are capable of asexual embryogenesis, giving rise to either new daughter sporocysts or the next stage of the life cycle: the infectious cercariae (**Figure 1.1C**). Cercariae are flagellated motile larvae which swim through the water in search of a definitive host. Upon finding a suitable host, they burrow through the host's skin and enter the bloodstream. During this process, they lose their flagella and transform into the next stage, referred to as the schistosomula. These schistosomula migrate through the host's bloodstream, ending up in the mesenteric vasculature around the liver and intestines (for most species that infect humans) or the vesical venous plexus around the bladder (for *S. haematobium*). Another unique feature of schistosomes is that, unlike all other flatworms, they are dioecious, possessing discrete male and female sexes. Upon reaching the mesenteric vasculature (or vesical venous plexus), the parasites rapidly increase in size and male and female parasites pair together (termed in copula). The female parasite resides inside a groove on the ventral surface of the male parasite (referred to as the gynaecophoric canal) where the pair begin sexual reproduction. The females ultimately produce a prodigious amount of eggs (hundreds to thousands daily, depending on the species), which must ultimately exit the bloodstream and enter the intestinal lumen (or bladder lumen for *S. haematobium*) in order to escape to the environment (**Figure 1.1D**). This is an inefficient process, with most eggs ending up trapped in host tissues including the liver and intestinal walls. The parasites themselves are not immunogenic, but their eggs result in profound inflammation in the tissues where they

become trapped. This inflammation is ultimately responsible for the pathology and symptomology of the disease (including hepatic fibrosis, portal hypertension, ascites, hematemesis, hematuria) [1].

Outside of the parasite's lifecycle, relatively little is understood about their fundamental biology, but much of which is known can be found summarized in Basch 1991 [35]. Before the molecular revolution, schistosome biologists were largely limited to electron microscopy and biochemistry. Despite these limitations, some key features of schistosome biology were discovered many decades ago. Classical studies have extensively examined the ultrastructure of many different tissues of the parasite in multiple stages of the lifecycle [36-41], necessary groundwork for more recent studies that have identified molecular markers of several tissues within the animal [42-44]. A great deal of the inner workings of schistosome metabolism was also described using classical biochemistry. Early experiments studying blood feeding found that schistosomes, especially females, consume incredible amounts host red blood cells [45] and the hemoglobin in these red blood cells is an important source of amino acids [46]. More recent work regarding blood feeding has shed additional light onto schistosome metabolism [47]. Because the schistosome's gut is a blind-ending tube, the parasites expel digestive waste products via regurgitation. Studies of the regurgitated substances ("vomitus") have identified many of the enzymes, especially proteases, that play important roles in blood digestion [48, 49]. Further studies of these enzymes have been instrumental in identifying schistosome-specific functions (i.e. blood feeding) that can be targeted for therapeutic effects [50-52]

As with many other animals, next generation sequencing has been a boon to the field. Multiple species of schistosome have had their genomes sequenced [53-57], revealing insights into adaptations to parasitism such as deficiencies in genes required to produce some classes of lipids. Additional studies of lipid metabolism have found conflicting evidence regarding beta oxidation. One study suggests that beta oxidation is required in the female parasite for egg

production [58], whereas other work suggests that beta oxidation does not occur in schistosomes and cannot on the virtue that they lack critical beta oxidation enzymes in their genome [59]. Glucose metabolism in schistosomes has also been studied for decades. Different stages of the lifecycle depend on aerobic versus anaerobic respiration. Cercariae rely predominantly on aerobic glycolysis to breakdown glycogen stores [35] whereas adult parasites uptake glucose from their host and produce energy via anaerobic glycolysis [60, 61].

Tegument biology and evolution

One of the most remarkable accomplishments of the schistosome is their ability to survive inside the host's bloodstream, surrounded by the immune system. Indeed, this environment has been described as "the most hostile environment imaginable" [36]. How do these parasites survive (often for decades at a time [62-64]) without succumbing to blood clotting or immune assault? The answer may lay in the parasite's skin-like tegument (**Figure 1.2**). The tegument is syncytium that surrounds the parasite, acting as the interface between the parasite and the host. It lacks most basic cellular components (such as nuclei, endoplasmic reticulum, and ribosomes). Instead, it connects through small cytoplasmic projections to thousands of cell bodies (sometimes termed "cytons") that sit below the parasite's body wall muscles. These cell bodies contain the cellular components that the tegument lacks (e.g. nuclei and ribosomes) and therefore serve as the source of important components such as proteins and secretory products [36, 65].

The adult schistosome lives inside the host's blood and as such must contend with very specific challenges, such as blood clotting, nutrient uptake, and immune assault (**Figure 1.2A**). The tegument appears to have adapted to help the schistosome survive and even thrive in the face of these challenges. Structurally, the tegument is unique in that the surface is not a single

lipid bilayer, but rather a stacked bilayer (classically referred to as “heptalaminate” [66]) (**Figure 1.2B**). It is thought that the outermost membrane is constantly shed and renewed, perhaps hiding the parasite from the immune system by preventing robust adhesion of antibodies, complement, or immune cells [67]. Indeed, there appears to be very little inflammation at the site of the parasite in vivo [68], suggesting a robust means of immune evasion. Many different mechanisms have been proposed to explain this immune evasion including: the ability of the parasite to “hide” by taking up host antigens [69-72], the ability to non-specifically bind the Fc domain of antibodies [73, 74], the ability to inhibit complement activation [75], and the ability to cleave immune-activating molecules such as sphingosine 1-phosphate [76, 77]. The schistosome tegument also appears to have important anti-coagulant function. Several proteins localized to the tegument surface are able to either activate endogenous host thrombolytic pathways [78, 79], cleave host prothrombotic proteins [80, 81], and breakdown host prothrombotic small molecules such as ATP, ADP, and polyphosphate [82-84]. In addition helping evade the immune system and prevent the formation of blood clots, the schistosome tegument also plays important roles in parasite metabolism [85]. Glucose and amino acids can be taken up directly from the parasite’s surrounding via tegument-localized transporters [86, 87]. The tegument also appears to play roles in osmoregulation [88] and waste excretion [89]

The incredible biology mediated by the tegument becomes even more fascinating when one considers its evolutionary origins. The tegument is found not only in schistosomes, but also in all parasitic flatworms. Virtually all parasitic flatworms, including schistosomes, are members of a clade of Platyhelminthes known as the Neodermata (plural, neodermatans) [90-92]. As the name implies, the neodermatans (“new skin”) are united by the presence of a syncytial tegument. Much like in schistosomes, the tegument is thought to play critical roles in other parasitic flatworms as well. Cestodes (often called tapeworms) seem to have lost their gut in favor of acquiring nutrients directly through their tegument [93]. Another potential adaptive

feature of the tegument is its ability to rapidly remodel when these parasitic flatworms transition between different hosts [66, 94, 95], suggesting that the tegument may facilitate the harsh transitions these parasites might encounter when transitioning between (in the case of the schistosome) aquatic and intravascular environments. Given all of this, and because the tegument is found in all neodermatans and not in any of their free-living relatives, the tegument is often thought of as a major evolutionary feature that allowed for parasitism to arise in Platyhelminthes [91, 94-96]. It is unfortunate, then, that we understand so little about how the tegument is formed or maintained in any parasitic flatworms.

In the case of the schistosome, we know that upon initial infection of the definitive host, mesenchymal cells appear to fuse to the tegument surface [66, 97]. Past this, however, we know next to nothing about tegument formation or maintenance. Is the tegument a static tissue, formed in the juvenile and then stable throughout the life of the animal inside the host? Or is there physiological turnover of tegumental cells that necessitates the parasite constantly generating new tegumental cells? Could this process be targeted in order to disrupt the parasite's protective "skin"? Given that the tegument is the feature that unites the Neodermata, answering these questions may not only shed light onto the evolution of parasitism in Platyhelminthes, but it might also suggest novel therapeutic targets that could help combat important diseases caused by schistosomes and other important flatworm pathogens.

Flatworm stem cells

A better understanding of schistosome biology can be obtained by examining the biology of some of their free-living relatives. When one hears flatworm, one often thinks "planaria". Planarians are fascinating animals and excellent models of regenerative biology for over 100 years [98]. Early pioneers of planarian biology morphologically described unique cells termed

“neoblasts” and demonstrated that the regenerative capabilities of planarians are radiation sensitive (and therefore derive from cell proliferation) [99] but it was not until the last several decades that scientists were able to show that these neoblasts were somatic stem cells and that they were the basis of planarian regeneration [98, 100-102]. It was eventually shown that a single neoblast was capable of reconstituting an entire neoblast-depleted animal [102]. In addition to their role in regeneration, neoblasts are required for the homeostatic maintenance of all the tissues in the animal [103]. Without neoblasts, the planarian will eventually die [99].

Following development of RNAi protocols in planarians [104] and the methodical exploitation of this technique to study neoblasts [105], our understanding of how neoblasts mediate regeneration, especially on a molecular level, has expanded exponentially. We now know genes that regulate specific functions of neoblasts. A planarian homolog of the RNA binding protein PIWI was found to be a specific marker of and required for planarian neoblasts [101]. The transcription factors *ovo* and *POU2/3* are required for eye and excretory system regeneration, respectively [106, 107]. Given the fact that not all individual neoblasts are capable of reconstituting a new animal and that different genes regulate the neoblast mediated regeneration of different tissues, it eventually raised the question of whether heterogeneity might exist within the neoblast pool. Single-cell studies of neoblasts eventually revealed that neoblasts are molecularly and functionally heterogenous [108-110].

Neoblasts are not just a feature of planarians [111]. More evolutionarily basal flatworms such as Macrostomum lignano also possess neoblast-like cells [112] that are regulated by many of the same molecules that regulate planarian neoblasts[113]. Neoblast-like cells were described in tapeworms several decades ago (reviewed by Koziol and Brehm [114]). More recently, it has been observed that neoblast-like cells are widespread throughout neodermatans [115-119]. If the presence of neoblasts, like the tegument, is ubiquitous in neodermatans, what role might they play in the adaptation to parasitism? Given the complex and bizarre life cycles of

many of these parasitic flatworms, it is tempting to speculate that having a large pool of highly plastic stem cells may allow for rapid adaptation of these parasites to new environments inside and outside of new hosts. But what about in the adult animal? Though tapeworms have been found to possess limited regenerative abilities [119] and schistosome neoblasts are capable of proliferating in response to injury [120], there is no evidence of robust planarian-like regeneration in parasitic flatworms. So what is it that neoblasts are doing in neodermatans?

Our recent work may provide a hint into the function of adult neoblasts in schistosomes [121]. We found that the primary output of adult schistosome neoblasts is a population of cells that express the tegument-associated protein *TSP-2* [122, 123]. While it is not clear what, if any, function neoblasts play in tegument biology, it is exciting to speculate that they may be involved in the maintenance and repair of the parasite's protective surface. If this hypothesis is correct, it raises several interesting questions: if neoblasts and the tegument are broadly conserved in neodermatans, are the neoblasts in all adult parasitic flatworms responsible for tegument maintenance? If neoblasts are responsible for maintaining the tegument, are they a valid therapeutic target in the treatment and prevention of diseases caused by neodermatans? If neoblasts are not responsible for maintaining the tegument in other parasitic flatworms, then what else might do they do? This body of work represents the most extensive studies to date of the neoblasts in any adult parasite and begins to answer many of these important questions.

CHAPTER 2

METHODS

Parasite acquisition and culture

Adult *S. mansoni* (NMRI strain, 6–7 weeks post-infection) were obtained from infected female mice by hepatic portal vein perfusion with 37°C DMEM (Sigma-Aldrich, St. Louis, MO) plus 10% Serum (either Fetal Calf Serum or Horse Serum) and heparin. Parasites were cultured as previously described [121]. Unless otherwise noted, all experiments were performed with male parasites. Experiments with and care of vertebrate animals were performed in accordance with protocols approved by the Institutional Animal Care and Use Committee (IACUC) of UT Southwestern Medical Center (approval APN: 2017-102092).

RNA interference

Chapter 3:

For *tsp-2* RNAi experiments, 10 freshly perfused 6-7-week-old male parasites (either as single worms or paired with females) were treated with 20 μg/ml dsRNA for 3 days in Basch Media 169. dsRNA was generated by *in vitro* transcription and was replaced every day. On the 3rd day, the worms were given fresh media. Thereafter, every 3 days the worms received fresh media and 20 μg/ml dsRNA for a total of 28 days and then the parasites were fixed as previously described [116].

Chapter 4:

For the candidate RNAi screen, 10 freshly perfused 6-7-week-old male parasites (either as single worms or paired with females) were treated with 30 μg/ml dsRNA for 7 days in Basch Media 169. dsRNA was generated by *in vitro* transcription and was replaced every day. On the 8th day, the worms were given fresh media. Thereafter, every 4th day the worms received 60

μg/ml dsRNA (~24 hours of exposure to dsRNA before the media was changed) for a total of 17 days. On day 17, the worms were pulsed with 10 μM EdU for 4 hours before being fixed as previously described [116].

For EdU pulse-chase RNAi experiments, 10 freshly perfused 6-7-week-old male parasites (either as single worms or paired with females) were treated with 30 μg/ml dsRNA for 7 days in Basch Media 169. dsRNA was generated by *in vitro* transcription and was replaced every day. On the 8th day, the worms were given fresh media. Thereafter, every 4th day the worms received 60 μg/ml dsRNA (~24 hours of exposure to dsRNA before the media was changed) for a total of 28 days. On day 21, the worms were pulsed with 10 μM EdU for 4 hours after which the media was changed. On day 28, the worms were fixed as previously described [116].

Chapter 5:

For specific details of RNAi experiments, see below. Generally, all experiments utilized freshly perfused male parasites that were between 6 and 7 weeks old. dsRNA treatments were all carried out at 30 μg/ml in Basch Media 169. dsRNA was generated by *in vitro* transcription and was replaced daily for the first 3 days then every 3 days thereafter. EdU pulses were performed at 5μM for 4 hours before either fixation or chase as previously described[116].

For parasites used with RNA assays (qPCR and RNAseq), RNAi-treated animals were immediately immersed in Trizol (Fisher Scientific 15-596-026) and snap frozen at -80°C at the end of the experiment

Chapter 6:

For specific details of RNAi experiments, see below. Generally, all experiments utilized freshly perfused male parasites that were between 6 and 7 weeks old. dsRNA treatments were all carried out at 30 μg/ml in Basch Media 169. dsRNA was generated by *in vitro* transcription and

was replaced daily for the first 3 days then every 3 days thereafter. EdU pulses were performed at 5μM for 4 hours before either fixation or chase as previously described[116].

For parasites used in TEM imaging, RNAi-treated animals were fixed in TEM fixative (described below) at the end of the experiment.

For parasites with dextran labeling of the gut, RNAi-treated animals were incubated with fluorescent dextran (Life Technologies D3312) 12 hours prior to fixation in 4% formaldehyde in PBSTx

For parasites used with RNA assays (qPCR and RNAseq), RNAi-treated animals were immediately immersed in Trizol (Fisher Scientific 15-596-026) and snap frozen at -80°C at the end of the experiment

For parasites used in bright-field imaging of blood in the gut, worms were placed on a coverslip immediately prior to imaging.

For parasites used in protease assays, RNAi-treated animals were removed from media and snap-frozen at -80°C at the end of the experiment.

For parasites used in transplants, 5-week-old parasites were treated daily with dsRNA for seven days prior to being injected into recipient mice.

As a negative control for all RNAi experiments, we used a non-specific dsRNA containing two bacterial genes [124]. Constructs used for RNAi synthesis were cloned as previously described [124]. For brevity, oligonucleotide sequences are omitted; please contact the author if needed.

Parasite labeling and imaging

Dextran labeling:

For dextran labeling of the tegument, freshly perfused male parasites were collected in the bottom of a 15 ml conical tube, all residual media was removed, and 100 µl of 5 mg/ml solution of biotin-TAMRA-dextran (Life Technologies D3312) dissolved in ultrapure water was added to ~50 parasites. These worms were constantly agitated by gentle vortexing for 3-4 minutes, and then doused with 10 ml of fixative solution (4% formaldehyde in PBSTx (PBS + 0.3% triton-X100)) to stop the labeling. The fixative solution was removed and replaced with 10 ml of fresh fixative solution to dilute residual dextran. The worms were fixed for 4 hours in the dark with mild agitation. Worms were then washed with 10 ml of fresh PBSTx for 10 minutes. Dextran-labeled worms were then labeled with Alexa Fluor 488-conjugated phalloidin (Lifetech A12379) (1:40 dilution in 1% bovine serum albumin in PBSTx) overnight or dehydrated in methanol and processed for in situ hybridization (ISH) or immunofluorescence.

For dextran labeling of the parasite gut, 10 male RNAi-treated parasites were given 10µL/mL of 5 mg/mL (in water) solution of biotin-TAMRA-dextran (Life Technologies D3312) and cultured 12 hours. The parasites were then fixed in fixative solution (4% formaldehyde in PBSTx (PBS + 0.3% triton-X100)) for 4 hours in the dark with mild agitation. Worms were then washed with 10 ml of fresh PBSTx for 10 minutes, then dehydrated in 100% methanol and stored at -20dC until used in fluorescence in situ hybridization (FISH) as described[116, 121].

Whole-mount *in situ* hybridization:

Colorimetric and fluorescence whole-mount *in situ* hybridization (WISH) analyses were performed as previously described [116, 121]. To strongly label the entire cytoplasm of tegumental cells by FISH, in some instances we pooled probes recognizing the tegument-specific markers *calpain, gtp-4, annexin, and npp-5.*

EdU labeling:

In vivo and *in vitro* EdU labeling and detection experiments were performed as previously described [116]. However, for the 5-week *in vivo* EdU pulse-chase experiments, mice were only exposed to ~30 cercariae to assure the mice would not succumb to schistosome infection prior to the end of the experiment.

Immunofluorescence:

Worms processed for *in situ* hybridization or dextran labeling were incubated in blocking solution (0.1 M Tris pH 7.5, 0.15 M NaCl and 0.1% Tween-20 with 5% Horse Serum and 0.5% Roche Western Blocking Reagent [125]) for 1 hour at room temperature and incubated overnight in affinity purified anti-*TSP-2* [123] diluted 1:1000 in blocking solution at 4^{o}C. The following day samples were washed 6x 20 m in PBSTx, incubated overnight in a 1:1000 dilution of AlexaFluor 488 goat anti-rabbit antibody (Thermo Fisher Scientific A11034) in blocking solution, and washed in PBSTx.

All fluorescently labeled parasites were counterstained with DAPI (1 µg/ml), cleared in 80% glycerol, and mounted on slides with Vectashield (Vector Laboratories).

Imaging:

Confocal images of fluorescently labeled samples was performed on either a Zeiss LSM700 or a Nikon A1 Laser Scanning Confocal Microscope. Unless otherwise mentioned all fluorescence images represent maximum intensity projections. To perform cell counts, cells were manually counted in maximum intensity projections derived from confocal stacks. We used two types of measurements to normalize cell counts between samples. In cases where we determined the number of cells in a particular region of the parasite (e.g., tegument) we collected confocal stacks and normalized the number of cells by total volume of the stack in µm^3. In cases where we determined the total number of labeled foci throughout the entire depth

of the parasite (e.g. EdU counts), we collected confocal stacks and normalized the number of cells to the length of the parasite in the imaged region in mm.

Brightfield images were acquired on a Zeiss AxioZoom V16 equipped with a transmitted light base and a Zeiss AxioCam 105 Color camera.

Transmission electron microscopy samples were prepared from RNAi-treated parasites that were immersed in fixative (2.5% glutaraldehyde in 0.1M sodium cacodylate buffer pH 7.4 with 2mM $CaCl_2$) and then amputated at the head and the tail in order to retain ~5mm of trunk. After three rinses with 0.1 M sodium cacodylate buffer, the parasite trunks were embedded in 3% agarose and sliced into small blocks ($1mm^3$), rinsed with the fixative three times and post-fixed with 1% osmium tetroxide and 0.8 % Potassium Ferricyanide in 0.1 M sodium cacodylate buffer for one and a half hours at room temperature. Samples were rinsed with water and *en bloc* stained with 4% uranyl acetate in 50% ethanol for two hours. They were then dehydrated with increasing concentration of ethanol, transitioned into propylene oxide, infiltrated with Embed-812 resin and polymerized in a 60°C oven overnight. Blocks were sectioned with a diamond knife (Diatome) on a Leica Ultracut 7 ultramicrotome (Leica Microsystems) and collected onto copper grids, post stained with 2% aqueous Uranyl acetate and lead citrate. Images were acquired on a Tecnai G2 spirit transmission electron microscope (FEI, Hillsboro, OR) equipped with a LaB_6 source at 120kV using a Gatan ultrascan CCD camera.

Western blotting

To generate protein lysates, RNAi treated male parasites were separated with 0.5% tricaine, their heads and testes were amputated, the remaining somatic tissue was homogenized in 100 µl of sample buffer (236 mM Tris pH 6.7, 128 mM H_3PO_4, 4% SDS, 20% Glycerol, 10 mM DTT, and protease inhibitors (Roche cOmplete, Mini, EDTA-free)).

Homogenized samples were incubated at 42°C for 45 min and alkylated with N-ethylmaleimide for 40 minutes at 37°C. Protein concentrations were determined by BCA assays, 40 µg of lysate was separated by SDS PAGE, proteins were transferred to nitrocellulose membranes, membranes were blocked in Li-Cor Odyssey Blocking Buffer, incubated in rabbit anti-*TSP-2* (1:5000) and mouse anti-Actin (0.25 µg/ml, Monoclonal JLA20, Developmental Studies Hybridoma Bank), washed in TBST, and incubated in secondary antibodies (1:10,000 goat anti-rabbit IRDye 680 RD, 1:15,000 goat anti-mouse IgM IRDye 800CW, Li-Cor). Blots were imaged using a Li-Cor Odyssey Infrared Imager.

Fluorescence Activated Cell Sorting

Chapter 4:

Freshly perfused worms were either exposed to 100 Gy of Gamma Irradiation on a J.L. Shepard Mark I-30 Cs^{137} source or left alone to serve as controls, then cultured for one week. After one week, males were separated from female worms by incubation in a 0.25% solution of tricaine [116]. Male worms were amputated to remove the head and testes, and the bodies of the worms were collected. These worm bodies were briefly minced with a razor blade and then suspended in a 0.5% solution of Trypsin/EDTA (Sigma T4174) in PBS. The worms were then triturated for approximately 15 minutes until the solution became turbid and no large pieces of worms were left. Trypsin was inactivated by adding an equal volume of Basch media, then samples were centrifuged at 500 *g* for 10 m at 4°C. Next the worms were resuspended in 1 ml of Basch media with 10 µl of RQ1 DNAse (Promega M6101) and incubated for 10 minutes at RT. The worms were centrifuged again at 500 *g* for 10 minutes at 4°C. Worms were resuspended in staining media (0.5% BSA, 2 mM EDTA in PBS) and incubated in anti-*TSP-2* polyclonal antibody (1:1000 dilution) for 45 minutes in the dark at 4°C. The worms were

centrifuged again at 500 *g* for 10 minutes at 4°C. The worms were then resuspended in staining media and incubated in Hoechst 33342 (18 µg/ml) (Sigma B2261) and goat anti-rabbit AF488 (Thermo Fisher Scientific A11034) (1:1000 dilution) for 1 hour at RT in the dark. The worms were centrifuged once again at 500 *g* for 10 minutes at 4°C. Worms were then resuspended in staining media containing Hoechst 33342 (18 µg/ml) and propidium iodide (1 µg/ml) (Sigma-Aldrich P4170) and then filtered through a 40 µm cell strainer. Filtered cells were then sorted on a FACSAria Fusion (BD Biosystems) with a 100 µm nozzle either into staining media for confocal imaging or directly into Trizol LS (Thermo Fisher Scientific 10296-010) for RNAseq experiments. For all FACS experiments, a Hoechst threshold was applied to exclude debris and improve the efficiency of sorting.

Chapter 6:

Freshly perfused adult male and sexually mature adult female worms were separated by incubation in a 0.25% solution of tricaine [116] for approximately 5 minutes. Sexually immature adult virgin female worms were separately perfused from single-sex infected mice. Male, mature female, or virgin female worms were suspended in a 0.5% solution of Trypsin/EDTA (Sigma T4174) in PBS. The worms were then triturated for approximately 10 minutes (mature and virgin females) or 15 minutes (males) until the solution became turbid and no large pieces of worms were left. The trypsin was inactivated by adding an equal volume of serum-containing media. The dissociated worms were then centrifuged at 500 *g* for 10 m at 4°C. Next the worms were resuspended in 1 ml of Basch media with 10 µL of RQ1 DNAse (Promega M6101) and incubated for 10 minutes at RT. The dissociated worms were centrifuged again at 500 *g* for 10 minutes at 4°C. The cells were then resuspended in 1mL of staining media (0.2% BSA, 2mM EDTA in PBS, pH7.40) and incubated in Hoechst 33342 (18 µg/ml) (Sigma B2261) for 1 hour at RT in the dark. 9mL of staining media was then added to the worms and then the whole suspension was filtered through a 40 µm cell strainer. The worms were centrifuged once again at 500 *g* for 10 minutes at

4°C. Worms were then resuspended in 1mL of staining media containing Hoechst 33342 (18 µg/ml) and propidium iodide (1 µg/ml) (Sigma-Aldrich P4170) and then filtered once more through a 40 µm cell strainer into a 12x75mm FACS tube. Filtered cells were then sorted on a FACSAria II custom (BD Biosystems) with 305/405/488/561/633nm lasers. Sorts were performed with a 100 µm nozzle and cells were sorted into sorting media (0.2% BSA in PBS, pH7.40). Live single cells (PI negative, singlet by comparing forward scatter height to forward scatter width) were sorted using a 100 µm nozzle and cells were sorted into sorting media (0.2% BSA in PBS, pH7.40). For all FACS experiments, a Hoechst threshold was applied to exclude debris and improve the efficiency of sorting.

Quantitative PCR and RNA sequencing

RNA collection and purification:

RNA collection was performed as previously described[121]; briefly, fresh parasites (for single-cell RNAseq), decapitated male RNAi-treated parasites (for chapter 4), or whole male RNAi-treated parasites (everything else) were collected in Trizol. RNA was purified from samples utilizing Direct-zol RNA miniprep kits (Zymo Research R2051).

Quantitative PCR:

Quantitative PCR analyses were performed as previously described [116, 121]. cDNA was synthesized using iScript™ cDNA synthesis kit (Bio-Rad 1708891) and qPCR was performed as previously described[126] utilizing iTaq™ Universal SYBR® Green Supermix (Bio-Rad 1725122) and a QuantStudio 3 Real-Time PCR System (Applied Biosystems); For brevity, oligonucleotide sequences are omitted; please contact the author if needed.

FACS-purified cell RNAseq:

RNA was extracted from purified cells (>40000 “Neoblast”, >4000 “TSP-2^{+}”, and 80000 “IR Rest” cells per biological replicate) collected from three independent FACS runs using Trizol LS (Thermo Fisher Scientific 10296-010). Libraries for RNAseq analysis were generated using the SMART-seq2 kit (Clontech) and reads obtained by Illumina sequencing. The total number of reads per gene was determined by mapping the reads to the *S. mansoni* genome using STAR (version 020201) [127]. *S. mansoni* genome sequence and GTF files used for mapping were acquired from Wormbase Parasite [128]. Pairwise comparisons of differential gene expression were performed with DESeq2 (version 1.12.2) [129]. To determine which genes showed the highest level of enrichment in the various cell populations we also performed Model Based clustering using the MBCluster.seq package in R [130]. This clustering analysis was only performed on genes that had more than 200 total reads from the Neoblast, *TSP-2*$^{+}$, and IR-REST cell populations. For RNAseq analysis of *zfp-1-1(RNAi)* parasites, Illumina reads for three biological replicates were mapped to the schistosome genome using STAR and differential gene expression changes were measured using DESeq2.

Whole parasite RNAseq:

RNAseq on *hnf4(RNAi)* parasites was performed as previously described[126] using TruSeq Stranded mRNA Library Prep (illumina 20020594) to prepare libraries, which were sequenced on a NextSeq 550 (illumina). The total number of reads per gene was determined by mapping the reads to the *S. mansoni* genome (v7) using STAR (version 020201)[127]. *S. mansoni* genome sequence and GTF files used for mapping were acquired from Wormbase Parasite[131]. Pairwise comparisons of differential gene expression were performed with DESeq2 (version 1.12.2)[129]. Volcano plots were made with using the “volc” function from ggplot2. To remove genes expressed at lower levels, genes with a base-mean expression value less than 50 were excluded from analysis. Furthermore, genes that were differentially expressed ($p_{adj} < 0.05$) that were not assigned to the automatically assigned to the “gut” cluster during initial clustering were

manually examined in the single-cell RNAseq data and those that were expressed in the gut were reclassified to the “gut” cluster. Raw and some processed data from single cell RNAseq and *hnf4* RNAi RNAseq experiments have been deposited in the NCBI Gene Expression are available from NCBI GEO with accession number GSE146737.

Protein alignments and phylogenetic trees

To estimate the evolutionary relationship between the various flatworm *ZFP-1* family members, protein sequences of these family members were aligned using Guidance (http://guidance.tau.ac.il) (settings: MSA Algorithm = MAFFT; --maxiterate 1000 –genafpair; number of alternative guide-trees: 100). Columns in the sequence alignment with a confidence score below 0.050 were removed and a tree was generated using RAxML (version 8.0.0) (options –T 4 –f a –p 11111 –x 1111 -# 1000 –m PROTGAMMAAUTOF). Sequences used for phylogenetic analysis were recovered from Wormbase Parasite [128] (https://parasite.wormbase.org), Planmine [132](http://planmine.mpi-cbg.de), the *Gyrodactylus salaris* genome database (http://invitro.titan.uio.no/gyrodactylus/index.html) [133], and the *Macrostomum lignano* genome initiative database [134] (http://www.macgenome.org). A FASTA formatted file can be found in Supplementary File 7. *S. mansoni ZFP-1* and *ZFP-1-1* DNA binding motifs were predicted using the ZFModels web server at http://stormo.wustl.edu/ZFModels/ [135].

Single-cell RNA sequencing

Single-cell RNA sequencing library preparation and atlas generation:

FACS-sorted cells were centrifuged again at 500 *g* for 10 minutes at 4°C then resuspended in 0.2% BSA in PBS. Libraries were created using a Chromium Controller (10x Genomics) according to manufacturer guidelines and sequenced in using a NextSeq 500 (illumina). Sequencing data was processed and mapped to the *Schistosoma mansoni* genome (v7) using Cell Ranger (10x Genomics). Unfiltered data from Cell Ranger was imported into Seurat (v3.1.1)[136, 137] and cells were filtered as follows: Female (nFeature_RNA (> 750), nCount_RNA (1500-20000), Percent Mitochondrial (<3%); Male/Virgin female (nFeature_RNA (> 750), nCount_RNA (1000-20000), Percent Mitochondrial (<3%)). Mitochondrial genes were identified as those with the prefix “Smp_9”. Each of the 9 individual datasets was normalized (NormalizeData) and variable features were identified (FindVariableFeatures, selection.method = "vst", nfeatures = 2000). From here, integration anchors were identified (FindIntegrationAnchors, dims 1:78), the data was integrated (IntegrateData, dims = 1:78, features.to.integrate = features), and scaled (ScaleData). We then ran RunPCA, RunUMAP (reduction = "pca", dims = 1:78, n.neighbors = 40), FindNeighbors (reduction = "pca", dims = 1:78), FindClusters (resolution = 5). The number of principal components (78) used for this analysis was defined by JackStraw. Analysis of the resulting single cell map found that clusters 27 and 50 contained few enriched markers, therefore we removed the 964 cells present in these clusters and reran the analysis with 78 principal components. From here we generated the final UMAP projection plot with RunUMAP (n.neighbors = 36, min.dist = 0.70, dims = 1:80). Next, we generated clusters (FindClusters, resolution = 5) and manually inspected the unique genes expressed in each of the clusters. In some cases we found that some of the 85 resulting clusters did not express a core set of unique genes, therefore, these clusters were merged into a single cluster of cells as follows: Neoblasts (clusters 0,1,2,6,7,37), Neoblast progeny (cluster 4,8), Neuron 1 (clusters 10, 60, 68), Neuron 6 (clusters 24, 26), Parenchyma (clusters 11, 12, 51), flame cells (clusters 14, 41), S1 Cells (clusters 3, 9, 32, 42) and tegument (clusters 36, 63). After merging we were left with a final map of 68 clusters of 43,642 cells. In some cases, we noted large differences or unexpected similarities in

several cell populations between which we reasoned could be attributable to technical factors (i.e. male dissociation takes longer than female dissociation) which could disproportionately affect some cell types in male parasites vs. female parasites (i.e. more muscle cells were recovered from female parasites than from males, despite male parasites possessing more muscle cells per animal). In order to confirm our clustering results and also to ensure that other factors such as differences in read depth did not impact our analysis, we collapsed major cluster types (neurons, neoblasts, etc.) and reanalyzed our data using the sctransform (that uses a negative binomial normalization rather than log transformation used in our initial analysis) function from Seurat v3.1[138] (**Figure 2.1**). Briefly, we ran SCTransform on all nine of our samples individually with default setting. Next we ran SelectIntegrationFeatures on all nine of our samples (nfeatures = 3000) to create a list of integration features ("sct features"). We then ran PrepSCTIntegration on all nine of our samples (anchor.features = "sct features") using default settings. After this we ran FindIntegrationAnchors on all nine of our samples (normalization.method = "SCT", anchor.features = "sct features") using the default settings to generate our integration anchors ("integration anchors"). We then ran IntegrateData (anchorset = "integration anchors", normalization.method = "SCT") with default settings. Next we ran RunPCA on the dataset (npcs = 200). Finally, we ran RunUMAP (n.neighbors = 50, min.dist = 0.20, dims = 1:200) and verified that our between-sample and between sex clustering results were largely the same. We still observed fewer than anticipated muscle cells in male samples, which we attribute to the relatively harsher dissociation conditions experienced by male parasites. Similar biases in cell recovery have been described in the dissociation of related flatworms [109].

Single-cell RNAseq heatmaps and dot plots:

Heat maps for Figures 5.5 and 5.6C were generated as follows: first, all neuron clusters (**Figure 5.1J**) or all muscle clusters (**Figure 5.1E**) were used to make a new Seurat object with the subset() command. Then the markers of these objects were found using the FindAllMarkers()

command with the parameters test.use = “roc”, only.pos = TRUE. The subset of genes to use for the heatmap was then determined by using the subset() command on those markers with the parameters avg_diff>0 and power >0.9 (neuron) or >0.8 (muscle) for each gene. Heatmaps were generated with the DoHeatmap() command on the new Seurat objects with the subset of genes for the heatmap using default parameters.

The dot plot for Figure 6.3D was generated as follows: first, clusters were simplified by collapsing all 31 neuron clusters into a single cluster (“Neurons”), all parenchyma clusters into a single cluster (“Parenchyma”), all muscle clusters into a single cluster (“Muscle”), all tegument clusters into a single cluster (“Tegument”), all germline clusters (“GSCs”, “GSC progeny”, “late female germ cells”, and “late male germ cells”) into a single cluster (“Germline”), all neoblast progeny cells (“neoblast progeny” and “hes2+”) into a single cluster (“Neoblast Progeny”), all tegument progenitor cells (“early tsp-2+”, “egc+”, “meg-1+”, “zfp-1-1+”, and “sm13+”) into a single cluster (“Tegument Progenitors”), all vitelline cells (“S1”, “S1 progeny”, “early vitellocytes”, “late vitellocytes”, and “mature vitellocytes”) into a single cluster (“Vitellaria”), and two neoblast clusters (“neoblast 1” and “neoblast 2”) into a single cluster (“Neoblasts”). Next, a dotplot was generated using the DotPlot() function in Seurat v3.1 with the 25 most down-regulated genes following *hnf4* RNAi. The size of the dot corresponds to the percentage of the cells in the cluster (indicated on the vertical axis) that express the given gene (indicated on the horizontal axis), whereas the color of the dot indicates the average expression level of the gene in the cluster.

A searchable database of scRNAseq data can be accessed at www.collinslab.org/schistocyte. Raw and some processed data from single cell RNAseq and *hnf4* RNAi RNAseq experiments have been deposited in the NCBI Gene Expression are available from NCBI GEO with accession number GSE146737.

Protease activity assays

To measure cysteine protease cathepsin activity [139], five worms of each RNAi condition were ground and sonicated in 300 µL assay buffer (0.1 M citrate-phosphate, pH 5.5). The lysate was centrifuged at 15,000*g* for 5 minutes and the pellet was discarded. The total protein concentration was calculated using the bicinchoninic acid assay with bovine serum albumin as the protein standard. Each well in the assay had 1 µg of protein. The assay buffer was 0.1 M citrate-phosphate, pH 5.5 with 2 mM DTT. CA-074 (Cayman Chemical, 24679-500) and E-64 (Alfa Aesar, J62933) controls were set up by incubating the sample with 10 µM of each inhibitor for 30 min at room temperature. The final substrate concentration of Z-FR-AMC (R&D Systems, ES009) was 10 µM. The release of the AMC fluorophore was recorded in a Synergy HTX multi-mode reader (BioTek Instruments, Winooski, VT) with excitation and emission wavelengths at 340nm and 460nm, respectively.

To measure aspartic protease cathepsin activity, five worms of each RNAi condition were ground and sonicated in 300 µL assay buffer (0.1 M citrate-phosphate, pH 5.5). The lysate was centrifuged at 15,000*g* for 5 mins and the pellet was discarded. Each well in the assay had 1 µg of protein. The assay buffer was 0.1 M citrate-phosphate, pH 3.5. Pepstatin A (MP Biomedicals, 0219536805) and E-64 controls were set up by incubating the sample with 10µM of either inhibitor for 30 minutes at room temperature. The final substrate concentration of mca-GKPILFFRL-K(dnp) (CPC Scientific, SUBS-017A) was 10µM. The release of the AMC fluorophore was recorded in a Synergy HTX multi-mode reader (BioTek Instruments, Winooski, VT) with excitation and emission wavelengths at 320nm and 400nm, respectively.

Surgical transplantation of schistosomes

Surgical transplantation was performed as previously described[120] with the following modifications. Seven days prior to surgery, 5-week-old parasites were recovered from mice and treated with 30 μg/ml dsRNA for 7 days in Basch Media 169. Before mice were anesthetized, 10 pairs (male and female) were sucked into a 1ml syringe, the syringe was fitted with a custom 25G extra thin wall hypodermic needle (Cadence, Cranston, RI), the air and all but ~200 μL of media were purged from the needle, and the syringe was placed needle down in a test tube to settle the parasites to the bottom of the syringe. Mice were kept on infrared heating pads for the duration of the surgery. Following wound closure, mice received a single subcutaneous 20 μL dose of a 1 mg/mL solution of Buprenorphine SR-LAB CIII for analgesia and were allowed to recover on a warm heating pad. Mice were group housed and individual mice were tracked by ear punches. On either day 22 or day 30 post-transplantation mice were sacrificed and perfused to recover parasites. Male and female parasites were counted and fixed for 4 hours in 4% formaldehyde in PBSTx. Recipient livers were removed and fixed for 72 hours in 4% formaldehyde in PBS. The percentage parasite recovery was determined by dividing the total (male and female) number of worms transplanted by the total number of parasites recovered following perfusion. Livers from individual mice were sectioned and processed for Hematoxylin and Eosin staining by the UT Southwestern Molecular Pathology Core.

Statistical analyses

All two-way comparisons were analyzed using Welch's t-test. All three-way comparisons were analyzed using one-way ANOVA. RNAseq data was analyzed by the Benjamini-Hochberg corrected Wald test in DeSeq2. The statistical enrichment of the various clusters of genes that were down-regulated following *zfp-1-1(RNAi)* ($\log_2$ <-0.5, padj < 0.05) was measured using a Fisher's exact test in R. Data used for the analysis are available online at PMID 29557781. *p* values are indicated in the figure legends or available online at PMID 32973030. Power

calculations for transplantation experiments were performed based on previously published data [120] (75% recovery vs. 0% recovery, alpha 0.05, beta 0.8)

CHAPTER 3

ADULT SCHISTOSOME STEM CELLS PRODUCE THE TEGUMENT

Modified from Wendt et al. 2018

Introduction

While neoblasts have been extensively characterized in planarians, molecular analysis of neoblasts in schistosomes is comparatively lacking. Planarian neoblasts are capable of giving rise to all tissues present in the animal as evidenced by the fact that a single neoblast can repopulate a lethally irradiated animal [102, 140]. The developmental potential of schistosome neoblasts was unclear. It had been shown that schistosome neoblasts could produce gut cells [116] but mainly produced cells that express the tegument-associated genes such as *tsp-2* [121]. It was not clear, however, what relationship these *tsp-2*$^{+}$ cells had with the tegument. Could these *tsp-2*$^{+}$ cells be tegument cells? Given the evolutionary and medical importance of the tegument, understanding whether or how schistosome neoblasts produced the tegument would be of great interest.

The schistosome tegument and associated cell bodies can be labeled specifically with fluorescently conjugated dextran

A prerequisite for studying the development of the tegument is the ability to visualize both the outer tegument and its associated cell bodies microscopically. However, this presently can only be accomplished by transmission electron microscopy [36], which is not compatible with methodologies to visualize the expression of molecular markers. Therefore, we explored a variety of live cell dyes and delivery techniques to identify an approach to specifically label the

schistosome tegument fluorescently (**Figure 3.1A**). We found that soaking live parasites in a hypotonic solution of 10 kDa fluorescent dextran specifically labeled the tegument surface (**Figure 3.1B**), cytoplasmic projections (**Figure 3.1C**), and the tegumental cell bodies (**Figure 3.1D**) that sit beneath the parasite's body wall muscles (**Figure 3.1E-F**). Since isotonic dextran solutions failed to label the tegument, we suspect that specific labeling requires damage to the outer tegumental membranes. Consistent with classic ultrastructural studies, these tegmental cell bodies extend one or more projections towards the tegumental surface [141, 142] (**Figure 3.1E-F**) and appear to form an elaborate interconnected network of cellular projections and cell bodies (**See "Movie 1" at PMID 29557781**). Since the narrowest tegumental cytoplasmic projections are much larger (~100 nm) [142] than the diameter of the fluorescent-dextran conjugate, it is likely that this approach is capable of labeling all cells directly attached to the tegument.

Definitive tegumental cells express *calpain*, *npp-5, annexin* and *gtp-4* but not *tsp-2*

To study the development of the tegument, we next sought to identify molecular markers expressed in tegumental cells and, therefore, performed FISH experiments on dextran-labeled parasites. Examination of a panel of candidate tegument-specific factors assembled from the literature [143-147] found that mRNAs for *calp*, *npp-5, annexin* and *gtp-4* were exclusively expressed in dextran positive cells at the levels of the tegument (**Figure 3.2A-D**), suggesting these genes encode markers of tegumental cells. We had previously demonstrated that cells expressing the mRNA for the tegument-specific factor *tsp-2* are rapidly produced by neoblasts and then rapidly turned over [121]. Since a variety of proteomic and immunological studies have demonstrated that the *TSP-2* protein is associated with the tegument [122, 123, 143, 146, 147], we were surprised that virtually all *tsp-2* mRNA-expressing cells were dextran-negative despite, in many cases, being found in close proximity to dextran-labeled tegumental cell bodies (**Figure 3.2E**). Similarly, we did not observe extensive co-localization of *tsp-2* with the tegumental markers

calpain, npp-5, *annexin* and *gtp-4* in adult parasites (**Figure 3.2F-I**). We made similar observations with another tegument-enriched factor *sm13* (**Figure 3.3**) that is exclusively expressed in *tsp-2*$^{+}$ cells [121]. Together, these data suggest that *tsp-2* mRNA is not expressed at high-levels in definitive tegumental cells.

tsp-2^{+} cells include putative progenitors to the definitive tegument

To reconcile the observation that *tsp-2* is not expressed in the definitive tegument with the extensive literature linking the *TSP-2* protein to the tegument surface, we performed immunofluorescence with an anti-*TSP-2* antibody [123]. We verified the specificity of this antibody by Western-blot following *tsp-2* RNAi treatment (**Figure 3.4A**). Similar to previous studies [122, 123], we observed high levels of *TSP-2* protein localized on the tegumental surface (**Figure 3.4B**). Upon the optimization of labeling conditions, we also noted that *TSP-2* protein could be detected in *tsp-2* mRNA-expressing cell bodies and their projections which extend toward the tegument surface (**Figure 3.4C-D**). We also detected lower levels of *TSP-2* in tegumental cell bodies expressing a mixture of tegument-specific mRNAs (*annexin*, *gtp-4*, *npp-5*, and *calp*) (**Figure 3.4C-D**) or labeled with dextran (**Figure 3.4E**). Although lower levels of *TSP-2* were typically found in tegumental cell bodies, higher levels of the protein were observed on the apical sides of these cells and in the projections extending to the tegument surface (**Figure 3.4C-E, "Movie 2" at PMID 29557781**). Additionally, we observed rare cells expressing markers of definitive tegumental cells, *TSP-2* protein, and low levels of *tsp-2* mRNA (**Figure 3.4F**). Based on these data, an attractive model is that *tsp-2* mRNA-expressing cells include a population of tegumental precursors and that as these cells differentiate to mature tegumental cells, the *TSP-2* protein remains stable while the *tsp-2* mRNA is down-regulated.

To explore the model that *tsp-2*$^+$ cells include a population of tegumental precursors, we examined the kinetics of the differentiation of neoblasts to *tsp-2*$^+$ cells and tegumental cells by performing pulse-chase experiments with the thymidine analog 5-Ethynyl-2'-deoxyuridine (EdU). In these experiments, we injected schistosome-infected mice with EdU to label proliferative neoblasts and then examined the kinetics by which these cells differentiate to produce both *tsp-2*$^+$ and definitive tegumental cells. If *tsp-2*$^+$ cells include precursors to the definitive tegument we anticipate: (I) that EdU would chase into the nuclei of *tsp-2*$^+$ cells prior to the definitive tegumental cells and (II) that as EdU signal is lost from the *tsp-2*$^+$ cell compartment we would observe a concomitant increase in the fraction of EdU$^+$ tegumental cells. Consistent with this model, at day 3 following an EdU pulse 45% of *tsp-2*$^+$ cells are EdU$^+$, whereas just 0.1% of definitive tegumental cells are EdU$^+$ at this time point. After day 3, however, the fraction of EdU$^+$*tsp-2*$^+$ cells began to drop, and the fraction of EdU$^+$ tegumental cells jumped to 12% by D5 before peaking at around 20% between day 7 and day 11 (**Figure 3.5A-B**). By day 35 the fraction of EdU$^+$ tegumental cells dropped to 2.2%, suggesting that tegumental cells are subject to physiological turnover inside a mammalian host. These data, together with our *TSP-2* immunolabeling studies, are consistent with a model in which neoblasts produce a population of short-lived *tsp-2*$^+$ progenitor cells that differentiate and fuse with the tegument (**Figure 3.5C**). Thus, tegumental cells appear to rely on neoblasts for their continual maintenance.

Discussion

This chapter describes a key advancement in the study of the schistosome tegument. Namely, we developed a technique to fluorescently label the tegument that was compatible with downstream labeling techniques including FISH and immunofluorescence. Using this technique, we were able to demonstrate that the previously-identified *tsp-2*$^+$ neoblast progeny [121] were not tegument cells, but rather apparent progenitors to the tegument. Interestingly, this biology, where

a neoblast specifies a progenitor cell that travels through the parenchyma towards the surface of the animal where it becomes the mature “skin”, very closely resembles that of the planarian [148], suggesting the possibility of a conserved pathway for “skin” production in flatworms. Still, the data here are not definitive; to show that *tsp-2*$^{+}$ neoblast progeny are *bona fide* tegument progenitor cells, we needed to specifically ablate the *tsp-2*$^{+}$ cells and show that the tegument was no longer produced. To accomplish this would necessitate more information about this putative tegument lineage.

CHAPTER 4

FLATWORM-SPECIFIC TRANSCRIPTIONAL REGULATORS PROMOTE THE SPECIFICATION OF TEGUMENTAL PROGENITORS IN SCHISTOSOMA MANSONI

Modified from Wendt et al. 2018

Introduction

Having previously shown that a lineage likely exists between neoblasts, *tsp-2*$^{+}$ neoblast progeny, and tegument cells, the next step was to validate the lineage. Without knowing what genes are expressed in the putative tegument lineage, it is very difficult to make an educated guess about which genes might regulate the lineage. The next goal, then, was to get transcriptomes from neoblasts and *tsp-2*$^{+}$ cells. FACS purification of flatworm stem cells has already been carried out in planarians, so we pursued a FACS-based purification approach followed by RNAseq analysis of purified populations.

FACs purification and molecular characterization of neoblasts and *TSP-2*$^{+}$ cells

As a first step towards understanding how tegument development and tissue homeostasis is regulated on a molecular level, we set out to characterize the expression of genes in both neoblasts and *tsp-2*$^{+}$ cells. Although our previous work exploited the radiation sensitivity of neoblasts and *tsp-2*$^{+}$ cells to identify candidate cell-type specific markers [116, 121], we were interested in directly measuring gene expression in these cells. To this end, we developed a FACS methodology to purify both proliferative neoblasts and *TSP-2*$^{+}$ tegumental progenitors from single-cell suspensions of schistosome somatic tissues (**Figure 4.1A**).

Since schistosome neoblasts appear to be the only proliferative somatic cell type [116], we adapted a methodology developed for FACS purifying neoblasts from free-living planarian flatworms using the live cell DNA-binding dye Hoechst 33342 [149]. In this approach, S/G2/M phase neoblasts can be purified from non-cycling (2N DNA content) cells due to their elevated DNA content (> 2N) as measured by Hoechst 33342 labeling intensity. Tetraspanins are transmembrane proteins often localized to the cell surface [150]. Since our anti-*TSP-2* antibody is directed to a putative extracellular loop of *TSP-2* [123], we also employed this antibody to FACS purify *TSP-2*$^+$ cells. Performing FACS on cell populations labeled with both Hoechst 33342 and anti-*TSP-2*, we could clearly resolve cells with >2N DNA content (putative neoblasts) and 2N cells with high levels of anti-*TSP-2* labeling (**Figure 4.1B**). Cells with >2N DNA content possessed typical neoblast morphology (small cells with a high nuclear:cytoplasmic ratio), whereas 2N cells with the highest levels of *TSP-2*$^+$ labeling possessed a lower nuclear:cytoplasmic ratio and labeled strongly for *TSP-2* on their surface (**Figure 4.1C**). We also noted a large population of cells with intermediate levels of *TSP-2* labeling (i.e., cells with 10^2-10^4 in relative *TSP-2* labeling intensity, **Figure 4.1B**). Visual examination of these cells found that they did not possess high levels of TSP-2 surface labeling. Instead, these "*TSP-2* Intermediate" cells had either no *TSP-2* surface labeling or had pieces of TSP-2-labeled debris attached to their surface. Since *TSP-2* is present at high-levels on the outer tegument, we believe these cells are falsely scored as *TSP-2*$^+$ due to the contamination of *TSP-2*$^+$ tegumental debris in our FACS preparations.

To unambiguously confirm the identity of the neoblast and *TSP-2*$^+$ cell populations, we also performed FACS with parasites 7 days post-treatment with 100 Gy of γ-irradiation, which is sufficient to deplete both neoblasts and *tsp-2*$^+$ cells but spare other differentiated cell types in the worms [116, 121]. Both the neoblasts and *TSP-2*$^+$ cell populations are eliminated following irradiation, confirming the specificity of our sorting procedure (**Figure 4.1B**). We also FACS-purified 2N *TSP-2*$^-$ irradiation insensitive cells, which we refer to hereafter as "IR Rest" cells

(**Figure 4.1B**). Consistent with the idea that the IR Rest cells represent various differentiated cell types in the parasite, the FACS-purified cells displayed a range of cellular morphologies (e.g., ciliated cells) and nuclear:cytoplasmic ratios (**Figure 4.1C**).

To define cell-type specific expression profiles, we performed RNAseq on purified neoblasts, *TSP-2*$^{+}$ cells, and IR Rest cell populations (**Figure 4.1B-C**). We performed pair-wise comparisons to define relative differences in gene expression between these three cell populations (**See "Supplementary File 1" at PMID 29557781**) and used model-based clustering [130] (**Figure 4.1D**) to identify genes whose expression was specifically enriched in each cell population (**See "Supplementary File 2" at PMID 29557781**). From this clustering analysis, we found clusters of genes whose expression was enriched to varying degrees in the IR Rest (clusters 1, 11, 15), neoblast (cluster 6 and to a lesser extent 10), and *TSP-2*$^{+}$ cell populations (cluster 3, 14, 5, 8). Examination of genes in these clusters identified anticipated cell-type specific markers: the IR Rest-enriched cluster 15 included genes whose expression is associated with differentiated cells such as neurons (i.e. *neuropeptide f receptor*, *neuroendocrine protein 7b2*); the neoblast-enriched cluster 6 included known neoblast-specific factors including *fgfra, nanos2,* and a variety of cell cycle-associated regulators; and the *TSP-2*$^{+}$-enriched clusters 3, 14, 8 included *tsp-2* and a variety of genes previously shown to be expressed in *tsp-2*$^{+}$ cells including *sm13, sm25, cationic amino acid transporter*, and *dysferlin* (**Figure 4.1E**) [121]. We also identified clusters of genes whose expression was enriched in two of the three cell populations. For instance, cluster 13 included genes enriched in both neoblasts and *TSP-2*$^{+}$ cells. Among the genes in cluster 13 was the *S. mansoni p53* homolog that was previously demonstrated to be highly expressed in both neoblasts and *tsp-2*$^{+}$ cells [121].

Since we found that *TSP-2*-labled cells expressed tegument-enriched genes (**Figure 3.4C-F**) we also reasoned that our FACS data might include markers of definitive tegument. Indeed, we noted that the *TSP-2*-enriched cluster 5 included all four of our validated markers of

definitive tegumental cells (*calp*, *npp-5*, *annexin*, and *gtp-4*) (**Figure 4.1E**). To explore the significance of this observation, we performed an *in-situ* hybridization screen to characterize the expression of genes present in *TSP-2*-enriched clusters, giving specific attention to genes present in cluster 5. Examining the expression of genes both at the level of the tegument and deeper inside the parenchyma where most *tsp-2*$^{+}$ cells reside (**Figure 4.2A**), we found that 26/29 genes in clusters 3, 14, 5, 8 that gave discernable expression patterns were expressed in either *tsp-2*$^{+}$ cells or 6definitive tegumental cells (**Figure 4.2B-C, "Supplementary File 3" at PMID 29557781**). Among these genes, 13/19 in cluster 5 alone were expressed in definitive tegumental cells (**See "Supplementary File 3" at PMID 29557781**), suggesting that genes in this cluster appear to be enriched for tegument-specific transcripts. We also noted from these analyses that *tsp-2*$^{+}$ cells are heterogeneous on a molecular level: cells deeper in the parenchyma tended to express a dynein heavy chain homolog, whereas more superficial *tsp-2*$^{+}$ cells expressed *sm13* and *sm25*. Similarly, we found a pair of transcripts encoding Endophilin B1 homologs that were expressed at high levels in a subset of mature tegumental cell bodies (**Figure 4.2B**). This heterogeneity could highlight populations of cells at different stages of commitment to the tegumental lineage. Taken together, these data suggest that clusters 3, 5, 8, 14 are enriched for transcripts expressed in either *tsp-2*$^{+}$ cells or definitive tegumental cells, providing an additional line of evidence connecting *tsp-2*$^{+}$ cells and the definitive tegument.

An RNAi screen identifies *zfp-1* and *zfp-1-1* as potential regulators of tegument development

To define genes that regulate the development of the tegument lineage, we used our neoblast and *TSP-2*$^{+}$-enriched datasets to select candidates for an RNAi screen of genes encoding putative transcription factors, RNA binding proteins, signaling molecules, and schistosome specific proteins. For this screen, we performed RNAi on adult parasites and

examined the numbers of neoblasts (by EdU-labeling) and *tsp-2*$^+$ cells (by FISH) (**Figure 4.3A**). We reasoned that genes required for general neoblast maintenance/proliferation would be essential for the maintenance of both EdU$^+$ neoblasts and *tsp-2*$^+$ cells (e.g., *histone H2B,* **Figure 4.3B**), whereas genes important for tegument development would be essential for the maintenance of *tsp-2*$^+$ cells but dispensable for neoblast maintenance. From these experiments, we identified several factors essential for neoblast maintenance, including: a homolog of the human breast cancer type 1 susceptibility protein (BRCA1), a homolog of the BRCA1 associated RING domain 1 (BARD1) protein, a previously uncharacterized fibroblast growth factor (FGF) receptor, and a homolog of the p53 tumor suppressor (**Figure 4.3B**). A number of other genes were screened that gave no stem cell or *tsp-2* phenotype (**Figure 4.3C**). Given our focus on genes required for tegumental differentiation, these genes were not explored further.

In addition, we found that RNAi of genes encoding two related C2H2 zinc finger proteins, *zfp-1* and *zfp-1-1,* resulted in a reduction in the total number of *tsp-2*$^+$ cells yet spared the number of EdU-labeled neoblasts (**Figure 4.4A-B**). Indeed, RNAi-mediated transcript reduction of either *zfp-1* or *zfp-1-1* (**Figure 4.4G**) resulted in an approximately 50% reduction in the number of *tsp-2*$^+$ cells (**Figure 4.4A-B**) and led to no change in the total number of *nanos2*$^+$ neoblasts capable of incorporating EdU (**Figure 4.4C-D**). The effect of *zfp-1* and *zfp-1-1* RNAi treatment was not specific to the expression of *tsp-2*, as RNAi of either of these genes similarly led to a sizable decrease in the total number of cells expressing *sm13*, another marker of tsp-2+ cells (**Figure 4.4E-F**). These observations strongly suggest *zfp-1* and *zfp-1-1* are important for the differentiation and/or maintenance of *tsp-2*$^+$ cells.

Consistent with our RNAseq data, we found that *zfp-1* was expressed exclusively in *nanos*2$^+$ neoblasts and not in *tsp-2*$^+$ cells (**Figure 4.4H-I**). Conversely, *zfp-1-1* was not expressed in *nanos2*$^+$ neoblasts but was expressed at high levels in *tsp-2*$^+$ cells (**Figure 4.4J-K**). Similar to other transcripts enriched in *tsp-2*$^+$ cells, *zfp-1-1* appeared to be expressed in a subset of *tsp-2*$^+$

cells that were located more internally within the parasite (**Figure 4.4L**). Since neoblasts are typically located deeper inside the parasite, these more internal *tsp-2*$^{+}$*zfp-1-1*$^{+}$ cells could represent early neoblast progeny, whereas the *tsp-2* single-positive cells may represent more mature tegumental progenitors. We further determined that *zfp-1-1* was not expressed in definitive tegumental cells (**Figure 4.4K**) and that *zfp-1* and *zfp-1-1* were not co-expressed (**Figure 4.4I**). Thus, *zfp-1* expression appears to be neoblast-specific, whereas *zfp-1-1* expression is enriched in a subset of *tsp-2*$^{+}$ cells.

zfp-1 and *zfp-1-1* are members of a family of flatworm-specific DNA binding proteins whose homolog in planarians regulates epidermal lineage specification

We examined the amino acid sequences of the proteins encoded by *zfp-1* and *zfp-1-1*. Not only were the three C2H2 zinc finger domains of *ZFP-1* and *ZFP-1-1* highly similar to one another, but we also uncovered a number of related C2H2 zinc finger domain-containing proteins in the genomes of free-living (i.e., planarians and macrostomids) and parasitic flatworms (i.e., flukes, tapeworms, monogeneans) (**Figure 4.5A**). A thorough examination of proteins from taxa outside the Platyhelminthes failed to find any close relatives that shared both high sequence identity and a similar number of C2H2 domains, suggesting that these proteins are likely to be flatworm specific. Phylogenetic analysis of these proteins revealed two distinct groups of these *ZFP-1* family proteins: one group more similar to the schistosome *zfp-1* and another more closely related to *zfp-1-1* (**Figure 4.5B**). Among the homologs identified was a protein encoded from the *zfp-1* gene in the planarian *Schmidtea mediterranea*. In parallel to our model for tegument renewal by short-lived *tsp-2*$^{+}$ tegumental progenitors, the planarian epidermis perpetually rejuvenated from a population of short-lived epidermal progenitors derived from the neoblasts [108, 151]. The production of these epidermal progenitors relies on the planarian *zfp-1,* which is expressed in a subset of lineage-restricted neoblasts [108]. Thus, our results with *zfp-1* and *zfp-1-1* suggest the

potential for a conserved role for these proteins in coordinating epidermal biogenesis programs among flatworms.

Although *zfp-1* has been previously characterized in *S. mediterranea,* the molecular function of this group of novel proteins is not clear. Since we found proteins in this family shared little homology outside the three C2H2 zinc finger domains, we reasoned that these domains are likely key to the function of these proteins. C2H2 zinc finger domains are best known for their ability to function as transcriptional regulators by binding DNA, however, these domains can also participate in RNA-binding and protein-protein interactions [152-154]. Thus, we examined the sequences of these proteins in more detail. C2H2 zinc finger domains contain two conserved cysteines and two conserved histidines for zinc-binding (**highlighted in black background in Figure 4.5A**). For the *zfp-1* family proteins, we observed that the residues between the second zinc-coordinating cysteine and the first zinc-coordinating histidine of the second and third zinc fingers exhibited high sequence conservation, forming the motifs QRSNLQR and RKDHLxR, respectively (**Figure 4.5A**). Typically, each C2H2 zinc finger interacts with three consecutive DNA base pairs, and the first, fourth, and seventh positions in these motifs (**highlighted in cyan background in Figure 4.5A**) are key contributors to the binding specificity of the 3′base, the middle base, and 5’ base of the primary interaction DNA strand, respectively [155, 156]. Given this stereotypical binding, it is possible to predict target DNA binding sequences solely from amino acid sequences [135]. Using this model, we predict the that the common preferred DNA binding sequence for all *ZFP-1* homologs examined is 5'-GGGGAA-3' (**Figure 4.5C**), based on the sequence conservation of the last two zinc fingers. Given the highly conserved nature of the residues that contribute to sequence-specific binding, we believe that *ZFP-1* family proteins function by binding DNA and presumably act as transcription factors.

zfp-1-1 appears to be specifically required for the production of new tegumental cells

If *tsp-2*$^{+}$ cells are tegumental precursors, and *zfp-1* and *zfp-1-1* play a role in the specification of tegumental cells, we would anticipate that loss of *tsp-2*$^{+}$ cells following reduction in *zfp-1* and *zfp-1-1* levels would block the birth of new tegumental cells. Eventually the reduction in tegumental cell birth would result in the reduction in the total number of tegumental cells. To determine if this was the case, we knocked down *zfp-1* or *zfp-1-1* and performed an EdU pulse-chase experiment examining the ability to produce new tegumental cells (**Figure 4.6A**). Following *zfp-1* RNAi treatment, we noted a relatively small, but statistically significant, reduction in the percentage of tegumental cells that were EdU^{+} (**Figure 4.6B-C**). In contrast to *zfp-1* RNAi treatment, knockdown of *zfp-1-1* led to an almost complete block in the ability of new cells to be added to the tegument (**Figure 4.6B-C**). Consistent with these observed reductions in production of new mature tegumental cells, we also noted that RNAi of *zfp-1* or *zfp-1-1* led to 15 and 30 percent reductions in the total density of tegumental cell bodies, respectively (**Figure 4.6B-C**). Together these data indicate that both zinc finger proteins are important for tegument specification, but that *zfp-1-1* appears to play a more substantial role in the process.

We next sought to determine if loss of *zfp-1* or *zfp-1-1* led to general defects in the ability of parasites to generate non-tegumental lineages. We first monitored the production of new gut cells using the gut-specific marker *cathepsin B*. Like the tegument, the gut is a syncytium, and gut cells appear to be renewed at a relatively high rate [116, 121]. Following a 7-day EdU chase period, we noted that *zfp-1-1(RNAi)* parasites generated new gut cells at roughly the same rate as control-treated worms (**Figure 4.6D**). Conversely, the rate of new gut cell birth was severely reduced in *zfp-1(RNAi)* worms, suggesting a role for *zfp-1* not just in tegumental differentiation but also in the generation of new gut cells. Given the paucity of cell-type specific markers in schistosomes we next wanted to monitor the general differentiation potential of neoblasts in *zfp-1(RNAi) and zfp-1-1(RNAi)* parasites. After a 4-hour EdU pulse >95% of EdU^{+} cells are *nanos2*$^{+}$ (160/166 EdU^{+} nuclei, *n* = 9 male parasites) (**Figure 4.4C**), therefore, we reasoned that we could

monitor the general differentiation potential of neoblasts by examining the amount of EdU-labeled nuclei exiting the *nanos2*$^{+}$ neoblast compartment after a 7-day chase period (**Figure 4.6A**). However, since *tsp-2*$^{+}$ cells are the major output of neoblasts [121], and neither *zfp-1* nor *zfp-1-1* RNAi treatments completely depleted the *tsp-2*$^{+}$ cell pool, we specifically examined the appearance of EdU^{+}*nanos2*$^{-}$*tsp-2*$^{-}$ cells in the parenchyma after a 7 day chase in order to exclude cells related to the tegument lineage. While we noted large numbers of EdU^{+}*nanos2*$^{-}$*tsp-2*$^{-}$ cells in both *zfp-1* and *zfp-1-1* RNAi treated parasites, *zfp-1(RNAi)* worms displayed a slight reduction in the total number of EdU^{+}*nanos2*$^{-}$*tsp-2*$^{-}$ cells relative to controls (**Figure 4.6E**). These data suggest that *zfp-1* may play a more general role in neoblast differentiation, whereas *zfp-1-1* appears to play a more specific role in the production of new tegumental cells.

During *in vitro* culture, schistosomes use their ventral sucker to attach themselves to the bottom of their cell culture dish [120]. In parallel to our observations with *zfp-1-1* in tegumental differentiation, we noted that *zfp-1-1(RNAi)* parasites detached from their culture vessel during RNAi treatment (**Figure 4.6F**); a similar phenotype was not observed for either control(RNAi) or *zfp-1(RNAi)* animals (**Figure 4.6F**). These data suggest that loss of tegument cell body density following *zfp-1-1* RNAi may result in gross physical deficits during *in vitro* culture.

To explore the effects of *zfp-1-1* RNAi in more detail, we performed transcriptional profiling of *zfp-1-1(RNAi)* parasites using RNAseq (**Figure 4.7A**). As anticipated, RNAi of *zfp-1-1* resulted in reduced expression of transcripts expressed in *tsp-2*$^{+}$ cells including *tsp-2*, *meg-1*, and *sm13* (**Figure 4.7B, "Supplementary File 4" at PMID 29557781**). Consistent with the observed reduction in the total number of tegumental cells following *zfp-1-1(RNAi)* (**Figure 4.6B-C**), we also found that transcripts for the definitive tegumental markers *calpain*, *annexin,* and *npp-5* were significantly down-regulated in *zfp-1-1(RNAi)* parasites (**Figure 4.7B, "Supplementary File 4" at PMID 29557781**). Importantly, we did not observe significant changes in the expression of genes associated with the schistosome nervous system (e.g., *pc2* [157]) nor in genes associated with

the intestine (*cathepsin B*) in *zfp-1-1(RNAi)* parasites (**Figure 4.7B**). To further explore the specificity of *zfp-1-1* RNAi for cells within the tegument lineage, we examined if genes represented by each of our individual expression clusters (**Figure 4.1D**) were statistically enriched among genes down-regulated in *zfp-1-1(RNAi)* parasites. If the effects of *zfp-1-1* depletion are largely restricted to the tegumental lineage and not to other tissues, we would anticipate that the majority of genes down-regulated in *zfp-1-1(RNAi)* parasites would represent genes expressed in the tegumental lineage. Consistent with this model, we found that clusters of genes with high-levels of *TSP-2*-enrichment (i.e., 3, 14, 5, and 13) were statistically overrepresented among genes down-regulated (log_2 fold change < -0.5, p_{adj} < 0.05) following *zfp-1-1(RNAi).* Conversely, clusters with low-levels of *tsp-2* enrichment (i.e., 1, 11, 7, 12, and 15) were statistically underrepresented among genes down-regulated following *zfp-1-1(RNAi)* (**Figure 4.7C**). Given these data, and our pulse-chase experiments (**Figure 4.6B-E**), the effects of *zfp-1-1* RNAi appear to predominantly affect the maintenance of tegumental cells and their progenitors. Therefore, we suggest that *zfp-1-1* represents a critical and specific regulator of tegumental specification in schistosomes.

Discussion

We previously described a preliminary model (**Figure 3.5C**) where neoblasts produce *tsp-2*$^+$ cells that migrate through the mesenchyme and as these progenitors approach the tegument, they extend cellular projections that traverse the muscle layers and basement membranes, and ultimately fuse with the outer tegument. In order to test this model, we used FACS to acquire transcriptomes of neoblasts and *TSP-2*$^+$ cells. This led to the identification of *zfp-1* and *zfp-1-1*, two flatworm-specific transcription factors that appear to be required for tegument production and maintenance (**Figure 4.8**). Indeed, we found that tegumental cell bodies are subject to physiological cell turnover (**Figure 3.5A**), and that ablation of tegmental progenitors by *zfp-1* of *zfp-1-1* RNAi results in reduced tegumental cell density (**Figure 4.6B-C**). As such, it appears that

neoblast-driven tegument renewal is essential for the homoeostatic maintenance of tegumental cell number.

One outstanding question relates to the molecular composition of cells within the tegumental lineage. Our data suggest that *tsp-2*$^{+}$ cells contribute to the tegument, but it is not clear if this property extends to all *tsp-2*-expressing cells. Analysis of genes expressed in FACS-purified *TSP-2*$^{+}$ cells found that several genes were expressed in subsets of *tsp-2*$^{+}$ cells (**Figure 4.2B-C**). One possible interpretation of these observations is that these distinct *tsp-2*$^{+}$ populations represent cells at different stages of commitment to a tegumental fate. However, it is possible that certain subsets of *tsp-2*$^{+}$ are destined to generate other non-tegumental lineages. Interestingly, we also observed that a pair of Endophillin B1-encoding genes are expressed in a subset of mature tegumental cells (**Figure 4.2B**), opening up the possibility that the tegument is comprised of molecular and functionally distinct cell bodies, despite being a syncytium. Based on the relative distribution of tegument-specific cytoplasmic inclusions, early ultrastructural studies hinted at the possibility that multiple classes of tegumental cell types exist [141]. Given this possibility, different types of *tsp-2*$^{+}$ cells may give rise to different classes of tegumental cell bodies. Alternatively, a mechanism for tegument cell renewal independent of *tsp-2*$^{+}$ cells may also exist. Detailed studies of these various cell populations using emerging single cell RNA sequencing technology is expected to improve our understanding of this cellular heterogeneity and how it relates to tegument biogenesis.

Although both *zfp-1* and *zfp-1-1* are essential for the normal production of tegumental cells, depletion of *zfp-1-1* appears to have a more profound effect on this process (**Figure 4.6B-C**). This observation is curious since *tsp-2*$^{+}$ cells are depleted to a similar extent in either *zfp-1(RNAi)* or *zfp-1-1(RNAi)* parasites (**Figure 4.4A-B**). However, we did note that *zfp-1-1(RNAi)* resulted in a much greater depletion of cells expressing *sm13* compared to *zfp-1(RNAi)* (**Figure 4.4E-F**). One possible explanation of this observation is that *zfp-1* and *zfp-1-1* RNAi treatments

have differential effects on cells within the *tsp-2*$^{+}$ compartment. Perhaps *zfp-1* acts in the stem cells to specify early tegumental *tsp-2*$^{+}$ progenitors, whereas *zfp-1-1* acts in early progenitors to control the fate of cells later during the commitment process. Given the effects of *zfp-1-1* on *sm13*$^{+}$ cells, and the location of these cells towards the parasite's surface (**Figure 4.2C**), it is possible that *sm13*$^{+}$ cells may represent a population of late tegumental progenitors. A more detailed examination of the various cell types within the *tsp-2*$^{+}$ compartment is expected to bring clarity to this issue.

In addition to the differential effect on *sm13*$^{+}$ cells, we found that *zfp-1–1* RNAi treatment resulted in a gradual detachment of the parasite from their culture vessel (**Figure 4.6F**). Parasites rely upon their ventral sucker to attach to blood vessel walls in the host and to the bottom of culture vessels during in vitro culture. As the only part of the worm that physically attaches to solid substrate, one might expect the ventral sucker to experience more 'wear and tear' than the rest of the organism. Like the rest of the worm, the sucker is covered in tegument. While we cannot say that the detachment phenotype is a direct result of the disruption of tegument maintenance, an attractive hypothesis is that the gross effects of loss of tegument cell renewal are first experienced by the sucker in the form of the inability to attach to substrate. Indeed, this hypothesis is supported by the observation that the effects of *zfp-1-1(RNAi)* are largely limited to tegumental cell populations (**Figure 4.7A-C**). Future studies exploring the function of *zfp-1–1* in the context of host infection could provide important insights into the role for tegmental renewal in parasite survival *in vivo*.

Our data highlight fundamental similarities in the cellular organization of epidermal lineages between schistosomes and the free-living planarian flatworms. Unlike schistosomes, free-living flatworms (e.g., planarians) possess a simple epidermis comprised of a single layer of epithelial cells that rests upon a basement membrane and several layers of muscles [94, 95, 158]. Counter to the epidermal maintenance strategies of other long-lived metazoa (e.g., cnidarians

[159] and mammals [160]), where resident stem cells support the renewal of worn out or damaged epithelial cells, the planarian epidermis is unique as it is completely devoid of proliferative cells [161]. To fulfill a constant demand for new epidermal cells, neoblasts in planarians specify large numbers of post-mitotic epidermal progenitor cells [108, 151, 161]. In many ways, these epidermal progenitors are similar to *tsp-2*$^{+}$ tegumental progenitors: they appear to be the primary output of neoblasts, they are rapidly lost following neoblast ablation, and they express a variety of species-specific factors. Furthermore, like schistosomes, these progenitors migrate through the mesenchyme, traverse the muscles and basement membrane, and incorporate into the existing epithelium [161]. Thus, the cellular organization of epidermal maintenance lineages in planarians and schistosomes appears to be quite similar despite resulting in two very different tissues (epidermis vs. tegument).

In addition to the similarities in their cellular organization, our data, together with previous studies of planarians [108, 162], suggest that flatworm epidermal lineages also rely on members of the *zfp-1* family of flatworm-specific transcriptional regulators. Despite the apparent conserved function of these regulators, we do note some differences in the function of *zfp-1* family proteins in planarians and schistosomes. The planarian and schistosome *zfp-1* genes are both expressed in neoblasts and based on sequence similarity they appear to be orthologous (**Figure 4.5A-B**). However, the planarian protein is specifically required for the maintenance of the epidermal lineage, whereas the schistosome protein appears to be essential for both tegumental and non-tegumental lineages (**Figure 4.6D**). Thus, it would appear the schistosome *zfp-1* homolog plays a more general role in cellular differentiation. These observations, however, do not rule out possibility that the schistosome *zfp-1* protein is directly responsible for specifying tegument fates. Indeed, loss of the non-tegumental lineages following *zfp-1* RNAi could represent a compensatory mechanism by the neoblasts to fulfill a high demand for new tegumental cells. Although a specific role for *zfp-1* cannot be demonstrated at this time, the schistosome *zfp-1-1* appears to have a

specific role in tegmental fates. Like *zfp-1*, the schistosome *zfp-1-1* has a related homolog in planarians (**Figure 4.5B**). While this planarian homolog has not been characterized, recent single cell transcriptional analyses suggest that the expression of this gene is enriched in the epidermal lineage [163]. Clearly, more detailed studies of these zinc finger proteins, and their roles in epidermal development, in both free-living and parasitic flatworms are essential to determine the significance of these observations.

Given these apparent similarities between planarians and schistosomes, and a wealth of evidence indicating that the Neodermata are descendants of free-living flatworms [91, 92, 164], it is possible that the evolution of the tegument, and perhaps even the emergence of parasitism, has its roots in the epidermal biogenesis programs of the free-living ancestors to modern day Neodermata. By modulating the basic cellular behaviors of epidermal progenitor cells during the course of evolution, perhaps there was a shift from migratory epidermal progenitors that intercalate into the multi-cellular epithelium to fusogenic progenitor cells that give rise to the syncytial tegument. Given this model, we suspect that our observations of neoblast-driven tegument biogenesis in schistosomes are likely to extend to all members of the Neodermata. Therefore, further study of tegumental development is expected to provide clues relevant for understanding the evolutionary forces that gave rise to parasitism in flatworms and could also suggest novel therapeutic strategies against this important group of parasites.

CHAPTER 5

A SINGLE-CELL RNASEQ ATLAS OF SCHISTOSOMA MANSONI

Modified from Wendt et al. 2020

Introduction

Our previous studies have highlighted numerous similarities between schistosome and planarian neoblasts, including shared molecular markers [116], proliferative response to injury [120], and conserved machinery regulating “skin” production [126]. That being said, there are many differences. Notably, planarian neoblasts appear to be heterogenous, with different subsets of stem cells apparently responsible for the production of different types of tissues [108]. Schistosomes, however, seem to possess homogenous neoblasts that only give rise to the tegument lineage and to a lesser extent the gut [126].

It is possible that heterogeneity exists within schistosome neoblasts, but we simply have not found it yet because of our limited understanding of the complex composition of the animal. Single-cell RNAseq (scRNAseq) has been used to comprehensively describe tissue types and physiology of diverse metazoans [109] including larval schistosomes [165] but we lack a comprehensive description of the cell types present in egg-laying adults. We only have specific molecular markers cell types: neoblasts, tegument progenitors, tegument cells, gut cells, and some types of germ cells [43, 116, 121, 126, 166, 167]. As such, we decided to employ scRNAseq to better understand the complexity of the adult parasite.

The cellular view of the schistosome

To define the molecular signature of adult schistosome cell types, we dissociated adult *Schistosoma mansoni*, isolated cells by Fluorescence-Activated Cell Sorting (FACS), and generated scRNAseq libraries using a 10x genomics chromium controller (**Figure 5.1A**). Schistosomes are dioecious and sexual maturation of the female worm's reproductive organs, including the ovary and vitellaria, requires sustained physical contact with the male worm [35]. Accordingly, we generated scRNAseq libraries from adult male parasites, adult sexually mature female parasites, and age-matched virgin female parasites. We then performed clustering, identifying 68 molecularly distinct clusters composed of 43,642 cells (**Figures 5.1B, 5.2, "Table S1" at PMID 32973030**). These included: three clusters of cells expressing somatic stem cell (*i.e.,* neoblast) markers such as the RNA binding protein *nanos2,* the cell surface receptor *notch,* and the receptor tyrosine kinase *fgfra* [116] (**Figures 5.1C, 5.3A**); eight clusters expressing markers of tegument progenitors [121, 126] (**Figure 5.3B**); two clusters of parenchymal cells (**Figures 5.1D, 5.3C**); one cluster of ciliated flame cells that are part of the worm's protonephridial (excretory) system (**Figures 5.1E, 5.3D**); eight clusters of muscles (**Figure 5.1F**); and a cluster of esophageal gland cells (**Figures 5.1G, 5.3E**). Despite being composed of thousands of nuclei, our analysis also identified clusters corresponding to syncytial tissues: the tegument [126] (**Figures 5.1H, 5.3F**) and gut (**Figures 5.1I, 5.3G**). We failed to identify cells from the female ootype (an organ involved in eggshell formation) [35] and the protonephridial ducts [168], possibly because of their multinucleate nature. Gene ontology (GO) analyses of these clusters (**See "Table S2" at PMID 32973030**) confirmed expected findings (enrichment of "DNA replication" in "neoblast 1") and revealed novel biology such as the enrichment of "extracellular matrix structural components" in muscle clusters suggesting muscles are the source of extracellular matrix in schistosomes, similar to planarians [169].

Somatic tissues at the single-cell level

We uncovered unexpected molecular complexity within the schistosome nervous system, identifying 30 clusters expressing the neuroendocrine protein *7b2* (**Fig 5.1J**) and one apparent neuronal cluster that did not express high levels of *7b2* but expressed several of synaptic molecules (e.g. *synapsin*) (**Figure 5.4A, bottom left, "Table S1" at PMID 32973030**). Examination of genes from these neuronal cell clusters uncovered unique molecular fingerprints for several populations (**Figures 5.4A-E, 5.5, "Table S1" at PMID 32973030**) and highly-ordered structural and regional specialization in the central and peripheral nervous systems. This included left-right asymmetry (**Figure 5.4B**) despite the absence of a clear *nodal* homolog [170], which regulates left-right asymmetry in other lophotrochozoa [171]. Planaria also appear to lack a *nodal* homolog but it has been shown that they do possess some functional asymmetry [172] and that BMP homologs regulate left-right asymmetry during regeneration [173]. Our data suggest that schistosome neurons (and perhaps flatworm neurons generally) may be involved in *nodal*-independent left-right asymmetry. In addition to anatomical complexity, we also found distinct molecular complexity. Our atlas identified nine clusters of apparently ciliated neurons (neuron clusters 2, 4, 5, 6, 9, 10, 16, 26, and 30) based on their expression of *Smp_097490* (which colocalizes with the cilium-labeling acetylated tubulin [44]) and enrichment for GO terms such as "cilium organization" and "cilium assembly" (**Figure 5.4C-D, "Table S2" at PMID 32973030**). Together, this complexity is surprising given the relatively "sedentary" lifestyle of adult parasites in the portal vasculature [35] and suggests that schistosome neurons may have roles beyond environmental sensation and locomotion, an avenue ripe for further investigation.

Schistosome muscle is also very heterogeneous, with eight muscle clusters that possess unique expression patterns (**Figure 5.6A-C**). Some populations occur diffusely throughout the animal ("muscle 1" and "muscle 2"), whereas others are anatomically restricted such as "muscle 7" cells that reside next to the gut, suggesting that they are enteric muscles. Sex-specific differences in muscle populations will be discussed below.

Similar to planarians [174], many morphogens that regulate *wnt* (**Figure 5.7A-D**) and *tgfb* signaling (**Figure 5.7E-H**) are expressed in muscle and neuronal cells. Homologs of many of these genes are expressed specifically in planarian muscles [109] and have been implicated in regulating regeneration in planarians [174]. Though schistosomes survive amputation [175], there is no evidence of whole-body regeneration. This expression pattern in a non-regenerative animal suggests these genes may regulate schistosome neoblasts during homeostasis. Indeed, prior to the studies described here, almost nothing was known about the intrinsic molecular regulation of schistosome neoblasts [116, 120]. Today, nothing is known about the extrinsic molecular regulation of neoblasts. Given the role that these morphogens play in regulating planarian neoblast function, loss-of-function studies of morphogens expressed in non-proliferative tissues of the schistosome have the potential to unlock a whole new level of understanding of schistosome stem cell biology.

Sexual tissues at the single-cell level

The pathology of schistosome infection is driven by the host's inflammatory responses to parasite eggs[176]. Thus, we examined the differences between male, sexually mature female, and age-matched virgin females at the cellular level (**Figure 5.8A**). All adult parasites have germline stem cells (GSCs) marked by expression of *nanos1*[43]. Our scRNAseq data revealed that GSCs have very similar gene expression regardless of sex or maturity (**Figures 5.8B, 5.9A**). Like GSCs, GSC progeny fall into the same clusters in both male and female parasites, suggesting no major sex- or maturation-dependent differences in early gametogenesis (**Figures 5.8C, 5.9B**). However, later germ cells cluster according to sex, with expression of "late female germ cells" markers found predominantly in mature females (**Figures 5.8D, 5.9C**) and "late male germ cells" markers only in males (**Figure 5.9D**).

The sexually mature schistosome ovary is structured such that GSCs reside at the anterior and mature oocytes at the posterior end [43, 177]. The “GSCs” marker *nanos1* is expressed in the proliferative anterior compartment (**Figures 5.8B, 5.10A-D**) whereas the “late female germ cells” marker *bmpg* is expressed most highly in the non-proliferative posterior ovary (**Figures 5.8D, 5.10C**). Our single-cell RNAseq data shows that the “GSC progeny” cluster sits between “GSCs” and “late female germ cells” on the UMAP plot, (**Figure 5.8A**), with the “GSC progeny” marker *meiob* expressed most highly between the anterior and posterior ovary (**Figures 5.8C, 5.10B**). Concurrent visualization of these clusters reveals an organized linear architecture (**Figure 5.10E**). Interestingly, both mature and virgin females express the marker *meiob* (**Figure 5.8C**) suggesting that virgin female GSCs express differentiation markers without male stimulus. Thus, male parasites may regulate this developmental checkpoint by promoting survival of differentiating GSCs rather than inducing commitment, consistent with studies suggesting that male-female pairing can suppress apoptosis in the vitellaria of virgin female worms [178].

We also examined the vitellaria, another male-sensitive, stem-cell dependent tissue that produces the yolk cells of the parasite’s eggs. Despite a different function and organization, we observed parallels between ovary and vitellaria maturation, such as expression of *nanos1* in the putative stem cell and the presence of an apparent lineage from stem cell to mature tissue (**Figure 5.11A-D**). We also found a low frequency of vitellocyte-like cells in males [179] (**Figure 5.11A**). Finally, we identified pairing-independent sexual tissues such as the flatworm-specific Mehlis’ gland that plays an enigmatic role in egg production [35] (**Figure 5.11E**).

In addition to sexual tissues, we observed sexual dimorphism in non-reproductive tissues as well including 3 muscle clusters (muscle 5, 6, and 8) that appear to be largely restricted to female parasites (**See “Table S3” at PMID 32973030**), with “muscle 8” representing muscle cells that surround the ovary (**Figure 5.12A-C**). The “muscle 8” marker *Smp_200110* was expressed in *tpm2*$^{+}$ muscle cells around the ovaries in mature and virgin female parasites (**Figure 5.12B-C**)

but only in *7b2*$^{+}$ neuronal cells in male parasites (**Figure 5.12D**). While it is unclear what if any function this female-specific muscle cluster might play in schistosome reproductive biology, somatic regulation of reproductive tissues has been described in planaria [124]. Further investigation of these sex-dependent differences in somatic cells may yield valuable insight into how schistosome reproduction is regulated.

Though our scRNAseq atlas identified many of the anticipated biological differences between male and female parasites for many reproductive tissues (i.e. “late male germ cells” being present only in males), some cells that belong to clusters that should largely be restricted to female parasites appear with unexpectedly high frequency in male parasites, namely the “late female germ cells”, “mature vitellocytes”, and “Mehlis’ gland” (**Figure 5.13**). In order to understand this phenomenon, we examined the expression of cluster-specific markers for each cluster individually. This examination revealed that these clusters were not homogenous, but rather composed of essentially two populations: one that expressed high levels of the cluster-specific markers and a separate population that expressed lower levels. Given the observation that planarian neoblasts sometimes express markers of differentiated tissues at low levels [109], we hypothesized that the cells expressing low levels of cluster-specific markers might be neoblast-like cells. Upon examining the expression of the neoblast marker *nanos2*, we did indeed find this to be the case for all three clusters.

Examination of the “late female germ cells” cluster (**Figure 5.13A**) reveals that *bmpg*$^{+}$ late female germ cells make up almost the entire cluster in sexually mature females whereas the *nanos2*$^{+}$ neoblast-like cells make up the majority of the cells in both males and virgin females. This agrees with the known biology; sexually mature female parasites possess a functional ovary that robustly produces mature oocytes. In contrast, virgin female parasites produce minimal late germ cells (**Figure 5.8D, bottom**). The few “late female germ cell”-like cells in males likely come from rare hermaphroditic ovary-bearing males [180].

Examination of the “mature vitellocyte” cluster (**Figure 5.13B**) reveals a similar phenomenon. *ataxin2*$^{+}$ mature vitellocytes are highly abundant in sexually mature females but rare in virgin females and males. *nanos2*$^{+}$ neoblast-like cells showed the opposite pattern: sparse in sexually mature females and relatively abundant in virgin females and males. Once again, this agrees with the biology: sexually mature female parasites should robustly produce mature vitellocytes but these cells should be rare within virgin females and males (**Figure 5.11A**).

Finally, examining the “Mehlis’ gland” cluster (**Figure 5.13C**) revealed similar findings. *Smp_343210*$^{+}$ Mehlis’ gland cells dominate the cluster in sexually mature and virgin female parasites but are sparse in male parasites. In contrast, *nanos2*$^{+}$ neoblast-like cells were abundant in male parasites (and to a lesser extent virgin female parasites). This, once again, agrees with the biology: the Mehlis’ gland is a pairing-independent tissue found in sexually mature and virgin females but not appreciably in males (**Figure 5.11E**). The *Smp_343210*$^{+}$ cells we observed in male parasites could represent a primordial Mehlis’ gland that expresses tissue markers below the limit of detection by WISH.

Discussion

Using scRNAseq, we were able to generate a cellular atlas of the adult schistosome. Our atlas is the most comprehensive atlas to date of any metazoan parasite to date. In this chapter, we illustrate the utility of using scRNAseq to understand non-traditional model organisms at the molecular level. Indeed, this chapter describes a monumental leap forward in our understanding of the cell biology of the schistosome. In addition to describing molecular markers of virtually all known tissues in the adult parasite, we also made numerous fascinating discoveries worthy of further investigation.

We found 8 different clusters of cells that we posit to be tegument progenitors and they exist along two linear pathways leading from neoblasts toward the definitive tegument (**Figure 5.2**). Based on expression of *tsp-2* in both lineages (see www.collinslab.org/schistocyte for gene expression plots not contained within this work), we know that at least one of these pathways contains tegument progenitors. Do both ultimately produce the tegument? If so, why are there two different lineages? Is only one responsible for tegument production? Then what do the *tsp-2*$^{+}$ non-progenitor cells do? Given our atlas of tegument progenitor markers and our knowledge of specific tegument regulators (**Figures 4.6 and 4.7**), we are now armed with the tools that we need to begin to unravel the finer points of tegument development.

We also identified previously unappreciated commonalities between schistosomes and planaria that have important implications for schistosome neoblast biology. Much like in planarians, schistosome muscle and neurons appear to be the primary source of many different morphogens (**Figure 5.7**). These morphogens are well characterized in planarians as regulators of regeneration [173, 181]. As schistosomes do not appear to have regenerative capabilities, what could these morphogens be doing in schistosomes? Once again, our atlas provides us with the knowledge of which morphogens are expressed specifically in muscles and neurons, allowing us to identify candidates for functional RNAi screens to better understand the non-regenerative function of these genes.

As a final example, our atlas will help us to understand how exactly schistosome reproduction, the cause of disease pathology, is controlled. We identified markers for reproductive tissues in male, sexually mature female, and virgin parasites (**Figure 5.8**). By examining these markers, we were able to confirm studies regarding GSC differentiation [178] (**Figure 5.8B-D**), provide a molecular description of the organization of reproductive organs (**Figure 5.10E**), and confirm the ectopic presence of female tissues in male parasites [179]. In sum, our scRNAseq

atlas represents an incredible resource for any researchers interested in studying schistosome biology.

CHAPTER 6

A NOVEL GUT LINEAGE IS REGULATED BY THE SCHISTSOME HOMOLOG OF HNF4

Modified from Wendt et al. 2020

Introduction

In chapters 3 and 4, we explored the biology of tegument production. We identified two regulators of tegument production, *zfp-1* and *zfp-1-1*, whose homologs regulate epidermal production in free-living flatworms [108]. This implies that “skin” production specifically (and perhaps stem cell differentiation generally) is an evolutionarily conserved feature of flatworm biology. This begs the question, what other aspects of flatworm biology are evolutionarily conserved?

As mentioned in chapter 1, one interesting feature of planarian neoblast biology is the specialization of neoblasts [108]. Different neoblasts appear committed to different fates, with the planarian homolog of *zfp-1* not only acting as a marker of the epidermal-biased neoblasts, but also functioning as a key regulator of epidermal neoblast function. In schistosomes, we have yet to see any evidence of neoblast specialization; indeed, all neoblasts essentially look the same with our current markers. That does not preclude the possibility of neoblast specialization, but our current lack of knowledge of cell types within the animal makes the search for and the study of neoblast heterogeneity in schistosomes very difficult

In the previous chapter, we demonstrated the utility of the scRNAseq atlas for enabling the most detailed descriptive study to date of adult schistosome somatic and reproductive tissues. Examining this atlas revealed the presence of three distinct neoblast clusters, which we dubbed “neoblast 1”, “neoblast 2”, and “*eled*$^{+}$ neoblasts” (**Figure 5.2**). Thus, heterogeneity does appear

to exist within schistosome neoblasts, but is it functional? Do these neoblast sub-populations play specialized roles in schistosome neoblast biology?

A subset of neoblasts give rise to the gut

Egg production is the primary driver of pathology, but this pathology is exacerbated by the parasite's stem cell-mediated longevity [116]. Previous work suggests adult neoblasts are molecularly homogeneous and predominantly give rise to cells involved in tegument production [121, 126] but free-living flatworms are known to possess functionally distinct neoblasts that produce specific tissues [108]. We identified a subpopulation of neoblasts ("*eled*$^+$ neoblasts") that formed a putative non-tegument lineage as suggested by a linear "path" of cells from *eled*$^+$ neoblasts to the gut (**Figure 6.1A-G**). Notably, these *eled*$^+$ neoblasts expressed *hnf4* (**Figure 6.1B-D**), a marker of gut neoblasts in planarians [108]. Thus, we hypothesized that these *eled*$^+$ neoblasts were gut neoblasts which give rise to a *prom2*$^+$ transition population and ultimately produce the gut.

hnf4* is required for gut neoblast function and gut maintenance *in vitro* and pathogenesis *in vivo

Given the importance of gut-mediated blood digestion for egg production [47], we sought to perturb this lineage by RNAi of genes expressed in this lineage (**Figure 6.2A-B**). We found that knocking down *hnf4* resulted in a ~3.8-fold increase in *eled*$^+$ neoblasts (**Figure 6.2B-E**). *eled* is expressed in germ tissues such as the testes, so we examined the expression of the germ marker *nanos1* along the gut, and found no increase in *nanos1* expression (**Figure 6.2F**), indicating the increase in *eled*$^+$ cells is likely not expansion of germ tissue but are instead somatic neoblasts. Further examination of the *hnf4(RNAi)* animals revealed a concomitant decrease in the

expression of several gut markers (**Figure 6.3A-B**). Indeed, RNAseq on *hnf4(RNAi)* animals demonstrated that over 70% of transcripts expressed in the "gut" cluster were downregulated (**Figure 6.3C-D, "Table S4" at PMID 32973030**).

The extensive transcriptional changes to gut-associated genes suggested there may be some structural or functional defects in the gut. To assess gut structure, we next supplemented the culture media of *hnf4(RNAi)* parasites with fluorescently-labeled dextran (which labels the gut lumen [49]). After 12 hours of culture, all control(RNAi) parasites but only 1 out of 15 *hnf4(RNAi)* parasites had dextran in the lumen (**Figure 6.4A, left**). Examination of the parasite's head showed that the dextran failed to enter the digestive tract of the *hnf4(RNAi)* parasites (**Figure 6.4A, right**), suggesting either a complete loss of patency or a defect in the parasite's ability to coordinate dextran ingestion. We then examined *hnf4(RNAi)* animals by transmission electron microscopy (TEM). The schistosome gut is a syncytial blind tube-like structure with a microvilli-filled lumen [182]. Though gut tissue was still present, we found a significant decrease in luminal microvilli (**Figure 6.4B-C**) and 2 out of 4 of *hnf4(RNAi)* animals had dilated lumens compared to controls (**Figure 6.4D-E**).

One possible explanation for the disruption of gut structure was a complete disruption of stem cell mediated tissue maintenance. To understand whether stem cells functioned normally in *hnf4(RNAi)* animals, we first looked at apoptosis using TUNEL and found no difference in *hnf4(RNAi)* animals, ruling out increased cell death (**Figure 6.5A**). Next, we looked at tegument production using EdU pulse-chase approaches. We found a significant increase in tegument production compared to controls (**Figure 6.5B-C**) ruling out a broad stem cell differentiation defect. Our ability to monitor new gut production by EdU pulse-chase approaches was complicated by the fact that gut marker expression was largely absent in most *hnf4(RNAi)* parasites (**Figure 6.3A-D**). In cases where we could detect gut marker expression in EdU pulse-chase experiments, we found gut-like tissue was being produced in *hnf4(RNAi)* parasites but was

morphologically abnormal (**Figure 6.5D**). Examination of the expression of *eled* and the gut marker *ctsb* revealed that locations where *eled*$^{+}$ neoblasts were abundant lacked *ctsb* expression (**Figure 6.5E**). This suggests that *hnf4* is required for *eled*$^{+}$ neoblasts to successfully differentiate into *ctsb*$^{+}$ gut cells and that this impairment of gut differentiation is at least partially responsible for the gut defects following *hnf4* RNAi.

Having observed extensive structural deficits in the gut following *hnf4* RNAi, we next wondered if gut function (i.e. blood digestion) was disrupted. To assess the digestive capability of *hnf4(RNAi)* parasites, we added red blood cells (RBCs) to the media and observed the parasites' ability to uptake and digest the cells. *hnf4(RNAi)* parasites either failed to ingest (15/69) or digest RBCs (54/69) (**Figure 6.6A-B**). Because we observed a decrease in the expression of proteolytic enzymes by RNAseq (**See "Table S4" at PMID 32973030**), we studied whether *hnf4* RNAi resulted in loss of cysteine (cathepsin) protease activity (which contributes to hemoglobin digestion [183]). Measuring cathepsin activity of lysates in *hnf4(RNAi)* parasites using a fluorogenic peptidyl substrate, we found cathepsin B activity was decreased 8.2-fold relative to control parasites (**Figure 6.6C**) consistent with gene expression analyses (**See "Table S4" at PMID 32973030**). In contrast, aspartyl protease activity was similar in control and *hnf4(RNAi)* parasites (**Figure 6.6D**), which could reflect expression of aspartic proteases in non-gut tissues that were unaffected following *hnf4* RNAi (**See "Table S1" and "Table S4" at PMID 32973030**). Together, these data suggest *hnf4* is at least indirectly required for the digestion of hemoglobin, in part by regulating the expression of cathepsin B, a key contributor to the digestion of blood proteins including hemoglobin [184], in *S. mansoni*.

We examined whether *hnf4* was required to cause disease in the host by transplanting control and *hnf4(RNAi)* parasites into uninfected mice and then perfusing the mice 22-30 days post-transplant. Worm recovery was statistically indistinguishable (control(RNAi) = 72% vs. *hnf4(RNAi)* = 49%, p = 0.136, Welch's t-test) (**Figure 6.7A**). This observation is not entirely

unexpected as schistosomes can acquire nutrients though their tegument [47]. Nonetheless, mice receiving *hnf4(RNAi)* parasites had morphologically normal livers in contrast to abundant egg-induced granulomata in control parasite recipients (**Figure 6.7B-C**). Additionally, recovered male *hnf4(RNAi)* parasites were significantly shorter than controls (2.87mm vs. 5.21mm, respectively, $p < 0.0001$, Welch's t-test) (**Figure 6.7D-E**). These results show *hnf4* is at least indirectly required for parasite growth and egg-induced pathology *in vivo*. Together, these data suggest *hnf4* specifically and gut homeostasis generally are potential therapeutic targets to blunt the pathology caused by adult parasites.

Discussion

In the previous chapter, we created a scRNAseq atlas of the adult schistosome. Here, we leveraged that atlas to advance our understanding of stem cell biology in schistosomes. Specifically, we identified an apparent gut lineage that begins with a specialized neoblast (the *eled*$^+$ neoblast). We further studied these *eled*$^+$ neoblasts and identified a regulator of these cells in the schistosome homolog of the nuclear receptor *hnf4*. Finally, we demonstrated that *hnf4* is required for disease pathology.

Taken together, this chapter highlights the utility of scRNAseq for the study of stem cell biology, especially in non-traditional model organisms where very little is known about the biology of interest. Indeed, without our atlas, we may never have been able to identify the relatively rare *eled*$^+$ neoblast population (**Figure 6.1B**). We also would not have had the ability to identify candidate regulators of these *eled*$^+$ neoblasts without our scRNAseq atlas providing us with the information of genes enriched in the *eled*$^+$ neoblast cluster (**Figure 6.2A-B**).

One exciting implication of the schistosome homolog of *hnf4* being required for disease pathology is that, as a ligand-influenced nuclear receptor [185, 186], *hnf4* homologs have the

potential to function as a drug targets. Even should schistosome *hnf4* not be a viable drug target, our data suggest that targeting schistosome gut homeostasis could be a viable therapeutic strategy. Our scRNAseq atlas provides us with a list of genes expressed in gut lineage, which we could serve as candidate therapeutic targets in this endeavor.

The impact of this work extends beyond the study of schistosomes. The study of virtually all parasitic metazoans is hampered by the dearth of molecular tools (most notably, genome editing). This generation of our schistosome atlas required only a FACS sorting protocol and a quality genome sequence. Even our functional studies were relatively simple to carry out relying mostly upon *ex vivo* culture, RNAi, and WISH, techniques already developed in many important parasitic metazoans [118, 119, 187-190]. Indeed, our approach serves as a template for the investigation of other understudied and experimentally challenging parasitic metazoans, improving our understanding of their biology and enabling the discovery of novel therapies for these pathogens.

REFERENCES

1. Colley, D.G., et al., *Human schistosomiasis.* Lancet, 2014. **383**(9936): p. 2253-64.
2. Organization, W.H., *Schistosomiasis, fact sheet no 115.* Geneva: World Health Organization, 2014.
3. King, C.H., *Health metrics for helminth infections.* Acta Trop, 2015. **141**(Pt B): p. 150-60.
4. Secor, W.E. and D.G. Colley, *When Should the Emphasis on Schistosomiasis Control Move to Elimination?* Trop Med Infect Dis, 2018. **3**(3).
5. Cioli, D., et al., *Schistosomiasis control: praziquantel forever?* Mol Biochem Parasitol, 2014. **195**(1): p. 23-9.
6. Friedman, J.F., et al., *Praziquantel for the treatment of schistosomiasis during human pregnancy.* Bull World Health Organ, 2018. **96**(1): p. 59-65.
7. World Health, O., *Schistosomiasis: progress report 2001 - 2011, strategic plan 2012 - 2020*. 2013, Geneva: World Health Organization.
8. Wang, W., L. Wang, and Y.S. Liang, *Susceptibility or resistance of praziquantel in human schistosomiasis: a review.* Parasitol Res, 2012. **111**(5): p. 1871-7.
9. Thomas, C.M. and D.J. Timson, *The Mechanism of Action of Praziquantel: Six Hypotheses.* Curr Top Med Chem, 2018. **18**(18): p. 1575-1584.
10. Bais, S. and R.M. Greenberg, *TRP channels as potential targets for antischistosomals.* Int J Parasitol Drugs Drug Resist, 2018. **8**(3): p. 511-517.
11. Greenberg, R.M., *New approaches for understanding mechanisms of drug resistance in schistosomes.* Parasitology, 2013. **140**(12): p. 1534-46.
12. Aragon, A.D., et al., *Towards an understanding of the mechanism of action of praziquantel.* Mol Biochem Parasitol, 2009. **164**(1): p. 57-65.

13. Stelma, F.F., et al., *Efficacy and side effects of praziquantel in an epidemic focus of Schistosoma mansoni.* Am J Trop Med Hyg, 1995. **53**(2): p. 167-70.

14. Tebeje, B.M., et al., *Schistosomiasis vaccines: where do we stand?* Parasit Vectors, 2016. **9**(1): p. 528.

15. Hsü, S.Y., H.F. Hsü, and J.W. Osborn, *Immunization of rhesus monkeys against schistosome infection by cercariae exposed to high doses of x-radiation.* Proc Soc Exp Biol Med, 1969. **131**(4): p. 1146-9.

16. Taylor, M.G., et al., *Immunisation of sheep against Schistosoma mattheei using either irradiated cercariae or irradiated schistosomula.* J Helminthol, 1976. **50**(1): p. 1-9.

17. Hsü, S.Y., et al., *Vaccination of bovines against schistosomiasis japonica with highly irradiated schistosomula in China.* Am J Trop Med Hyg, 1984. **33**(5): p. 891-8.

18. You, H., et al., *Schistosome Vaccines for Domestic Animals.* Trop Med Infect Dis, 2018. **3**(2).

19. Wilson, R.A., X.H. Li, and W. Castro-Borges, *Do schistosome vaccine trials in mice have an intrinsic flaw that generates spurious protection data?* Parasit Vectors, 2016. **9**: p. 89.

20. Langenberg, M.C.C., et al., *A controlled human Schistosoma mansoni infection model to advance novel drugs, vaccines and diagnostics.* Nat Med, 2020. **26**(3): p. 326-332.

21. Tanaka, H. and M. Tsuji, *From discovery to eradication of schistosomiasis in Japan: 1847-1996.* Int J Parasitol, 1997. **27**(12): p. 1465-80.

22. Kajihara, N. and K. Hirayama, *The War against a Regional Disease in Japan A History of the Eradication of Schistosomiasis japonica.* Trop Med Health, 2011. **39**(1 Suppl 1): p. 3-44.

23. Coelho, P. and R.L. Caldeira, *Critical analysis of molluscicide application in schistosomiasis control programs in Brazil.* Infect Dis Poverty, 2016. **5**(1): p. 57.

24. Ivy, J.A., et al., *Historical perspective: Revisiting the St. Lucia Project, a multi-year comparison trial of schistosomiasis control strategies.* PLoS Negl Trop Dis, 2018. **12**(1): p. e0006223.

25. Negrón-Aponte, H. and W.R. Jobin, *Schistosomiasis control in Puerto Rico: twenty-five years of operational experience.* Am J Trop Med Hyg, 1979. **28**(3): p. 515-25.

26. Jobin, W.R., et al., *Biological control of Biomphalaria glabrata in major reservoirs of Puerto Rico.* Am J Trop Med Hyg, 1977. **26**(5 Pt 1): p. 1018-24.

27. Pointier, J.P. and J. Jourdane, *Biological control of the snail hosts of schistosomiasis in areas of low transmission: the example of the Caribbean area.* Acta Trop, 2000. **77**(1): p. 53-60.

28. Pointier, J.P., *Invading freshwater snails and biological control in Martinique Island, French West Indies.* Mem Inst Oswaldo Cruz, 2001. **96 Suppl**: p. 67-74.

29. Howarth, F.G., *Environmental Impacts of Classical Biological Control.* Annual Review of Entomology, 1991. **36**(1): p. 485-509.

30. Sokolow, S.H., et al., *To Reduce the Global Burden of Human Schistosomiasis, Use 'Old Fashioned' Snail Control.* Trends Parasitol, 2018. **34**(1): p. 23-40.

31. Sokolow, S.H., et al., *Reduced transmission of human schistosomiasis after restoration of a native river prawn that preys on the snail intermediate host.* Proc Natl Acad Sci U S A, 2015. **112**(31): p. 9650-5.

32. Laamrani, H., et al., *Evaluation of environmental methods to control snails in an irrigation system in Central Morocco.* Trop Med Int Health, 2000. **5**(8): p. 545-52.

33. Incani, R.N., *The Venezuelan experience in the control of schistosomiasis mansoni.* Mem Inst Oswaldo Cruz, 1987. **82 Suppl 4**: p. 89-93.

34. al-Madani, A.A., *Schistosomiasis control in Saudi Arabia with special reference to the period 1983-1988.* Public Health, 1990. **104**(4): p. 261-6.

35. Basch, P.F., *Schistosomes: Development, Reproduction, and Host Relations*. 1991, New York: Oxford University Press. 248.

36. McLaren, D.J., *Schistosoma mansoni: The parasite surface in Relation to Host Immunity*. Tropical Medicine Research Studies Series, ed. K.N. Brown. Vol. 1. 1980, Letchworth, England: John Wiley & Sons, Ltd. 229.

37. McLaren, D.J. and D.J. Hockley, *Blood flukes have a double outer membrane.* Nature, 1977. **269**(5624): p. 147-9.

38. Dorsey, C.H., *Schistosoma mansoni: description of the head gland of cercariae and schistosomules at the ultrastructural level.* Exp Parasitol, 1976. **39**(3): p. 444-59.

39. Dorsey, C.H. and M.A. Stirewalt, *Schistosoma mansoni: fine structure of cercarial acetabular glands.* Exp Parasitol, 1971. **30**(2): p. 199-214.

40. Neill, P.J., et al., *The ultrastructure of the Schistosoma mansoni egg.* Am J Trop Med Hyg, 1988. **39**(1): p. 52-65.

41. Göbel, E. and J.P. Pan, *Ultrastructure of the daughter sporocyst and developing cercaria of Schistosoma japonicum in experimentally infected snails, Oncomelania hupensis hupensis.* Z Parasitenkd, 1985. **71**(2): p. 227-40.

42. Cogswell, A.A., et al., *Whole mount in situ hybridization methodology for Schistosoma mansoni.* Mol Biochem Parasitol, 2011. **178**(1-2): p. 46-50.

43. Wang, J. and J.J. Collins, III, *Identification of new markers for the Schistosoma mansoni vitelline lineage.* Int J Parasitol, 2016. **46**(7): p. 405-10.

44. Collins, J.J., III, et al., *An atlas for Schistosoma mansoni organs and life-cycle stages using cell type-specific markers and confocal microscopy.* PLoS Negl Trop Dis, 2011. **5**(3): p. e1009.

45. Lawrence, J.D., *The ingestion of red blood cells by Schistosoma mansoni.* J Parasitol, 1973. **59**(1): p. 60-3.

46. Zussman, R.A., P.M. Bauman, and J.C. Petruska, *The role of ingested hemoglobin in the nutrition of Schistosoma mansoni.* J Parasitol, 1970. **56**(1): p. 75-9.

47. Skelly, P.J., et al., *Schistosome feeding and regurgitation.* PLoS Pathog, 2014. **10**(8): p. e1004246.

48. Caffrey, C.R., et al., *Schistosoma japonicum, S. mansoni, S. haematobium, S. intercalatum, and S. rodhaini: cysteine-class cathepsin activities in the vomitus of adult worms.* Parasitology Research, 1996. **83**(1): p. 37-41.

49. Hall, S.L., et al., *Insights into blood feeding by schistosomes from a proteomic analysis of worm vomitus.* Mol Biochem Parasitol, 2011. **179**(1): p. 18-29.

50. Stefanic, S., et al., *RNA Interference in Schistosoma mansoni Schistosomula: Selectivity, Sensitivity and Operation for Larger-Scale Screening.* PLoS Negl Trop Dis, 2010. **4**(10): p. e850.

51. Morales, M.E., et al., *RNA interference of Schistosoma mansoni cathepsin D, the apical enzyme of the hemoglobin proteolysis cascade.* Mol Biochem Parasitol, 2008. **157**(2): p. 160-8.

52. Correnti, J.M., P.J. Brindley, and E.J. Pearce, *Long-term suppression of cathepsin B levels by RNA interference retards schistosome growth.* Mol Biochem Parasitol, 2005. **143**(2): p. 209-15.

53. Berriman, M., et al., *The genome of the blood fluke Schistosoma mansoni.* Nature, 2009. **460**(7253): p. 352-8.

54. Protasio, A.V., et al., *A systematically improved high quality genome and transcriptome of the human blood fluke Schistosoma mansoni.* PLoS Negl Trop Dis, 2012. **6**(1): p. e1455.

55. Luo, F., et al., *An improved genome assembly of the fluke Schistosoma japonicum.* PLoS Negl Trop Dis, 2019. **13**(8): p. e0007612.

56. Young, N.D., et al., *Whole-genome sequence of Schistosoma haematobium.* Nat Genet, 2012. **44**(2): p. 221-5.

57. Liu, F., et al., *The Schistosoma japonicum genome reveals features of host-parasite interplay.* Nature, 2009. **460**(7253): p. 345-51.

58. Huang, S.C., et al., *Fatty acid oxidation is essential for egg production by the parasitic flatworm Schistosoma mansoni.* PLoS Pathog, 2012. **8**(10): p. e1002996.

59. Bexkens, M.L., et al., *Schistosoma mansoni does not and cannot oxidise fatty acids, but these are used for biosynthetic purposes instead.* Int J Parasitol, 2019. **49**(8): p. 647-656.

60. Thompson, D.P., et al., *Changes in glucose metabolism and cyanide sensitivity in Schistosoma mansoni during development.* Mol Biochem Parasitol, 1984. **13**(1): p. 39-51.

61. Bueding, E., *Carbohydrate metabolism of schistosoma mansoni.* J Gen Physiol, 1950. **33**(5): p. 475-95.

62. Harris, A.R., R.J. Russell, and A.D. Charters, *A review of schistosomiasis in immigrants in Western Australia, demonstrating the unusual longevity of Schistosoma mansoni.* Trans R Soc Trop Med Hyg, 1984. **78**(3): p. 385-8.

63. Hornstein, L., et al., *Persistent Schistosoma mansoni infection in Yemeni immigrants to Israel.* Isr J Med Sci, 1990. **26**(7): p. 386-9.

64. Payet, B., et al., *Prolonged latent schistosomiasis diagnosed 38 years after infestation in a HIV patient.* Scand J Infect Dis, 2006. **38**(6-7): p. 572-5.

65. Wilson, R.A. and P.E. Barnes, *The tegument of Schistosoma mansoni: observations on the formation, structure and composition of cytoplasmic inclusions in relation to tegument function.* Parasitology, 1974. **68**(2): p. 239-58.

66. Hockley, D.J. and D.J. McLaren, *Schistosoma mansoni: changes in the outer membrane of the tegument during development from cercaria to adult worm.* Int J Parasitol, 1973. **3**(1): p. 13-25.

67. Skelly, P.J. and R.A. Wilson, *Making sense of the schistosome surface.* Adv Parasitol, 2006. **63**: p. 185-284.

68. Keating, J.H., R.A. Wilson, and P.J. Skelly, *No overt cellular inflammation around intravascular schistosomes in vivo.* J Parasitol, 2006. **92**(6): p. 1365-9.

69. Smithers, S.R., R.J. Terry, and D.J. Hockley, *Host antigens in schistosomiasis.* Proc R Soc Lond B Biol Sci, 1969. **171**(1025): p. 483-94.

70. Clegg, J.A., S.R. Smithers, and R.J. Terry, *"Host" antigens associated with schistosomes: observations on their attachment and their nature.* Parasitology, 1970. **61**(1): p. 87-94.

71. Goldring, O.L., et al., *Acquisition of human blood group antigens by Schistosoma mansoni.* Clin Exp Immunol, 1976. **26**(1): p. 181-7.

72. Damian, R.T., *Common antigens between adult Schistosoma mansoni and the laboratory mouse.* J Parasitol, 1967. **53**(1): p. 60-4.

73. Wu, C., et al., *Non-immune immunoglobulins shield Schistosoma japonicum from host immunorecognition.* Sci Rep, 2015. **5**: p. 13434.

74. Loukas, A., et al., *Receptor for Fc on the surfaces of schistosomes.* Infect Immun, 2001. **69**(6): p. 3646-51.

75. Deng, J., et al., *Inhibition of the complement membrane attack complex by Schistosoma mansoni paramyosin.* Infect Immun, 2003. **71**(11): p. 6402-10.

76. Elzoheiry, M., et al., *Intravascular Schistosoma mansoni Cleave the Host Immune and Hemostatic Signaling Molecule Sphingosine-1-Phosphate via Tegumental Alkaline Phosphatase.* Front Immunol, 2018. **9**: p. 1746.

77. Bryan, A.M. and M. Del Poeta, *Sphingosine-1-phosphate receptors and innate immunity.* Cell Microbiol, 2018. **20**(5): p. e12836.

78. Pirovich, D.B., A.A. Da'dara, and P.J. Skelly, *Schistosoma mansoni glyceraldehyde-3-phosphate dehydrogenase enhances formation of the blood-clot lysis protein plasmin.* Biol Open, 2020. **9**(3).

79. Figueiredo, B.C., et al., *Schistosomes Enhance Plasminogen Activation: The Role of Tegumental Enolase.* PLoS Pathog, 2015. **11**(12): p. e1005335.

80. Wang, Q., A.A. Da'dara, and P.J. Skelly, *The human blood parasite Schistosoma mansoni expresses extracellular tegumental calpains that cleave the blood clotting protein fibronectin.* Sci Rep, 2017. **7**(1): p. 12912.

81. Wang, Q., A.A. Da'dara, and P.J. Skelly, *The blood fluke Schistosoma mansoni cleaves the coagulation protein high molecular weight kininogen (HK) but does not generate the vasodilator bradykinin.* Parasit Vectors, 2018. **11**(1): p. 182.

82. Elzoheiry, M., et al., *The Essential Ectoenzyme SmNPP5 from the Human Intravascular Parasite Schistosoma mansoni is an ADPase and a Potent Inhibitor of Platelet Aggregation.* Thromb Haemost, 2018. **118**(6): p. 979-989.

83. Elzoheiry, M., et al., *Schistosomes can hydrolyze proinflammatory and prothrombotic polyphosphate (polyP) via tegumental alkaline phosphatase, SmAP.* Mol Biochem Parasitol, 2019. **232**: p. 111190.

84. Da'dara, A.A., et al., *Schistosome tegumental ecto-apyrase (SmATPDase1) degrades exogenous pro-inflammatory and pro-thrombotic nucleotides.* PeerJ, 2014. **2**: p. e316.

85. Da'dara, A., et al., *Metabolite movement across the schistosome surface.* J Helminthol, 2012. **86**(2): p. 141-7.

86. Krautz-Peterson, G., et al., *Suppressing glucose transporter gene expression in schistosomes impairs parasite feeding and decreases survival in the mammalian host.* PLoS Pathog, 2010. **6**(6): p. e1000932.

87. Krautz-Peterson, G., et al., *Amino acid transport in schistosomes: Characterization of the permeaseheavy chain SPRM1hc.* J Biol Chem, 2007. **282**(30): p. 21767-75.

88. Faghiri, Z. and P.J. Skelly, *The role of tegumental aquaporin from the human parasitic worm, Schistosoma mansoni, in osmoregulation and drug uptake.* FASEB J, 2009. **23**(8): p. 2780-9.

89. Faghiri, Z., et al., *The tegument of the human parasitic worm Schistosoma mansoni as an excretory organ: the surface aquaporin SmAQP is a lactate transporter.* PLoS One, 2010. **5**(5): p. e10451.

90. Littlewood, D.T.J. and R.A. Bray, *Interrelationships of the Platyhelminthes*. The Systematics Association Special Volume Series, ed. A. Warren. 2001, London: Taylor & Francis. 356.

91. Laumer, C.E., A. Hejnol, and G. Giribet, *Nuclear genomic signals of the 'microturbellarian' roots of platyhelminth evolutionary innovation.* Elife, 2015. **4**.

92. Ehlers, U., *Das Phylogenetische System der Plathelminthes*, ed. G. Fischer. 1985, Stuttgart.

93. Halton, D.W., *Nutritional adaptations to parasitism within the platyhelminthes.* Int J Parasitol, 1997. **27**(6): p. 693-704.

94. Tyler, S. and M. Hooge, *Comparative morphology of the body wall in flatworms (Platyhelminthes).* Can. J. Zool., 2004. **82**: p. 194-210.

95. Tyler, S. and M.S. Tyler, *Origin of the epidermis in parasitic platyhelminths.* Int J Parasitol, 1997. **27**(6): p. 715-38.

96. Littlewood, D.T.J., *The Evolution of Parasitism in Flatworms*, in *Parasitic Flatworms: Molecular Biology, Biochemistry, Immunology, and Physiology*, A.G. Maule and N.J. Marks, Editors. 2006, CAB International Oxfordshire, UK. p. 1-36.

97. Skelly, P.J. and C.B. Shoemaker, *The Schistosoma mansoni host-interactive tegument forms from vesicle eruptions of a cyton network.* Parasitology, 2001. **122 Pt 1**: p. 67-73.

98. Baguñà, J., *The planarian neoblast: the rambling history of its origin and some current black boxes.* Int J Dev Biol, 2012. **56**(1-3): p. 19-37.

99. Bardeen, C.R. and F.H. Baetjer, *The inhibitive action of the Roentgen rays on regeneration in planarians.* Journal of Experimental Zoology, 1904. **1**(1): p. 191-195.

100. Baguna, J., E. Saló, and C. Auladell, *Regeneration and pattern formation in planarians. III. Evidence that neoblasts are totipotent stem cells and the source of blastema cells.* Development, 1989. **107**: p. 77-86.

101. Reddien, P.W., et al., *SMEDWI-2 is a PIWI-like protein that regulates planarian stem cells.* Science, 2005. **310**(5752): p. 1327-30.

102. Wagner, D.E., I.E. Wang, and P.W. Reddien, *Clonogenic neoblasts are pluripotent adult stem cells that underlie planarian regeneration.* Science, 2011. **332**(6031): p. 811-6.

103. Reddien, P.W., *The Cellular and Molecular Basis for Planarian Regeneration.* Cell, 2018. **175**(2): p. 327-345.

104. Sánchez Alvarado, A. and P.A. Newmark, *Double-stranded RNA specifically disrupts gene expression during planarian regeneration.* Proc Natl Acad Sci U S A, 1999. **96**(9): p. 5049-54.

105. Reddien, P.W., et al., *Identification of genes needed for regeneration, stem cell function, and tissue homeostasis by systematic gene perturbation in planaria.* Dev Cell, 2005. **8**(5): p. 635-49.

106. Lapan, S.W. and P.W. Reddien, *dlx and sp6-9 Control optic cup regeneration in a prototypic eye.* PLoS Genet, 2011. **7**(8): p. e1002226.

107. Scimone, M.L., et al., *A regulatory program for excretory system regeneration in planarians.* Development, 2011. **138**(20): p. 4387-98.

108. van Wolfswinkel, J.C., D.E. Wagner, and P.W. Reddien, *Single-Cell Analysis Reveals Functionally Distinct Classes within the Planarian Stem Cell Compartment.* Cell Stem Cell, 2014. **15**(3): p. 326-39.

109. Fincher, C.T., et al., *Cell type transcriptome atlas for the planarian Schmidtea mediterranea.* Science, 2018. **360**(6391).

110. Plass, M., et al., *Cell type atlas and lineage tree of a whole complex animal by single-cell transcriptomics.* Science, 2018. **360**(6391).

111. Gehrke, A.R. and M. Srivastava, *Neoblasts and the evolution of whole-body regeneration.* Curr Opin Genet Dev, 2016. **40**: p. 131-137.

112. Ladurner, P., R. Rieger, and J. Baguñà, *Spatial distribution and differentiation potential of stem cells in hatchlings and adults in the marine platyhelminth macrostomum sp.: a bromodeoxyuridine analysis.* Dev Biol, 2000. **226**(2): p. 231-41.

113. Pfister, D., et al., *Flatworm stem cells and the germ line: Developmental and evolutionary implications of macvasa expression in Macrostomum lignano.* Developmental Biology, 2008. **319**(1): p. 146-159.

114. Koziol, U. and K. Brehm, *Recent advances in Echinococcus genomics and stem cell research.* Vet Parasitol, 2015. **213**(3-4): p. 92-102.

115. Koziol, U., et al., *The unique stem cell system of the immortal larva of the human parasite Echinococcus multilocularis.* Evodevo, 2014. **5**(1): p. 10.

116. Collins, J.J., III, et al., *Adult somatic stem cells in the human parasite Schistosoma mansoni.* Nature, 2013. **494**(7438): p. 476-9.

117. Wang, B., J.J. Collins, 3rd, and P.A. Newmark, *Functional genomic characterization of neoblast-like stem cells in larval Schistosoma mansoni.* Elife, 2013. **2**: p. e00768.

118. McCusker, P., et al., *Stimulating Neoblast-Like Cell Proliferation in Juvenile Fasciola hepatica Supports Growth and Progression towards the Adult Phenotype In Vitro.* PLoS Negl Trop Dis, 2016. **10**(9): p. e0004994.

119. Rozario, T., et al., *Region-specific regulation of stem cell-driven regeneration in tapeworms.* Elife, 2019. **8**.

120. Collins, J.N. and J.J. Collins, III, *Tissue Degeneration following Loss of Schistosoma mansoni cbp1 Is Associated with Increased Stem Cell Proliferation and Parasite Death In Vivo.* PLoS Pathog, 2016. **12**(11): p. e1005963.

121. Collins, J.J., III, et al., *Stem cell progeny contribute to the schistosome host-parasite interface.* Elife, 2016. **5**.

122. Tran, M.H., et al., *Tetraspanins on the surface of Schistosoma mansoni are protective antigens against schistosomiasis.* Nat Med, 2006. **12**(7): p. 835-40.

123. Pearson, M.S., et al., *Enhanced protective efficacy of a chimeric form of the schistosomiasis vaccine antigen Sm-TSP-2.* PLoS Negl Trop Dis, 2012. **6**(3): p. e1564.

124. Collins, J.J., III, et al., *Genome-Wide Analyses Reveal a Role for Peptide Hormones in Planarian Germline Development.* PLoS Biol, 2010. **8**(10): p. e1000509.

125. King, R.S. and P.A. Newmark, *In situ hybridization protocol for enhanced detection of gene expression in the planarian Schmidtea mediterranea.* BMC Dev Biol, 2013. **13**: p. 8.

126. Wendt, G.R., et al., *Flatworm-specific transcriptional regulators promote the specification of tegumental progenitors in Schistosoma mansoni.* Elife, 2018. **7**.

127. Dobin, A., et al., *STAR: ultrafast universal RNA-seq aligner.* Bioinformatics, 2013. **29**(1): p. 15-21.

128. Howe, K.L., et al., *WormBase ParaSite - a comprehensive resource for helminth genomics.* Mol Biochem Parasitol, 2016.

129. Love, M.I., W. Huber, and S. Anders, *Moderated estimation of fold change and dispersion for RNA-seq data with DESeq2.* Genome Biol, 2014. **15**(12): p. 550.

130. Si, Y., et al., *Model-based clustering for RNA-seq data.* Bioinformatics, 2014. **30**(2): p. 197-205.

131. Howe, K.L., et al., *WormBase 2016: expanding to enable helminth genomic research.* Nucleic Acids Res, 2016. **44**(D1): p. D774-80.

132. Brandl, H., et al., *PlanMine--a mineable resource of planarian biology and biodiversity.* Nucleic Acids Res, 2016. **44**(D1): p. D764-73.

133. Hahn, C., B. Fromm, and L. Bachmann, *Comparative genomics of flatworms (platyhelminthes) reveals shared genomic features of ecto- and endoparastic neodermata.* Genome Biol Evol, 2014. **6**(5): p. 1105-17.

134. Simanov, D., et al., *The Flatworm Macrostomum lignano Is a Powerful Model Organism for Ion Channel and Stem Cell Research.* Stem Cells Int, 2012. **2012**: p. 167265.

135. Gupta, A., et al., *An improved predictive recognition model for Cys(2)-His(2) zinc finger proteins.* Nucleic Acids Res, 2014. **42**(8): p. 4800-12.

136. Butler, A., et al., *Integrating single-cell transcriptomic data across different conditions, technologies, and species.* Nat Biotechnol, 2018. **36**(5): p. 411-420.

137. Stuart, T., et al., *Comprehensive Integration of Single-Cell Data.* Cell, 2019. **177**(7): p. 1888-1902.e21.

138. Hafemeister, C. and R. Satija, *Normalization and variance stabilization of single-cell RNA-seq data using regularized negative binomial regression.* Genome Biol, 2019. **20**(1): p. 296.

139. Caffrey, C.R. and A. Ruppel, *Cathepsin B-like activity predominates over cathepsin L-like activity in adult Schistosoma mansoni and S. japonicum.* Parasitol Res, 1997. **83**(6): p. 632-5.

140. Zeng, A., et al., *Prospectively Isolated Tetraspanin(+) Neoblasts Are Adult Pluripotent Stem Cells Underlying Planaria Regeneration.* Cell, 2018. **173**(7): p. 1593-1608.e20.

141. Morris, G.P. and L.T. Threadgold, *Ultrastructure of the tegument of adult Schistosoma mansoni.* J Parasitol, 1968. **54**(1): p. 15-27.

142. Hockley, D.J., *Ultrastructure of the tegument of Schistosoma.* Adv Parasitol, 1973. **11**(0): p. 233-305.

143. Braschi, S. and R.A. Wilson, *Proteins exposed at the adult schistosome surface revealed by biotinylation.* Mol Cell Proteomics, 2006. **5**(2): p. 347-56.

144. Rofatto, H.K., et al., *Characterization of phosphodiesterase-5 as a surface protein in the tegument of Schistosoma mansoni.* Mol Biochem Parasitol, 2009. **166**(1): p. 32-41.

145. Skelly, P.J. and C.B. Shoemaker, *Rapid appearance and asymmetric distribution of glucose transporter SGTP4 at the apical surface of intramammalian-stage Schistosoma mansoni.* Proc Natl Acad Sci U S A, 1996. **93**(8): p. 3642-6.

146. Wilson, R.A., *Proteomics at the schistosome-mammalian host interface: any prospects for diagnostics or vaccines?* Parasitology, 2012. **139**(9): p. 1178-94.

147. van Balkom, B.W., et al., *Mass spectrometric analysis of the Schistosoma mansoni tegumental sub-proteome.* J Proteome Res, 2005. **4**(3): p. 958-66.

148. Tu, K.C., et al., *Egr-5 is a post-mitotic regulator of planarian epidermal differentiation.* Elife, 2015. **4**.

149. Hayashi, T., et al., *Isolation of planarian X-ray-sensitive stem cells by fluorescence-activated cell sorting.* Dev Growth Differ, 2006. **48**(6): p. 371-80.

150. Charrin, S., et al., *Tetraspanins at a glance.* J Cell Sci, 2014. **127**(Pt 17): p. 3641-8.

151. Eisenhoffer, G.T., H. Kang, and A. Sánchez Alvarado, *Molecular analysis of stem cells and their descendants during cell turnover and regeneration in the planarian Schmidtea mediterranea.* Cell Stem Cell, 2008. **3**(3): p. 327-39.

152. Krishna, S.S., I. Majumdar, and N.V. Grishin, *Structural classification of zinc fingers: survey and summary.* Nucleic Acids Res, 2003. **31**(2): p. 532-50.

153. Brayer, K.J. and D.J. Segal, *Keep your fingers off my DNA: protein-protein interactions mediated by C2H2 zinc finger domains.* Cell Biochem Biophys, 2008. **50**(3): p. 111-31.

154. Hall, T.M., *Multiple modes of RNA recognition by zinc finger proteins.* Curr Opin Struct Biol, 2005. **15**(3): p. 367-73.

155. Wolfe, S.A., L. Nekludova, and C.O. Pabo, *DNA recognition by Cys2His2 zinc finger proteins.* Annu Rev Biophys Biomol Struct, 2000. **29**: p. 183-212.

156. Klug, A., *The discovery of zinc fingers and their applications in gene regulation and genome manipulation.* Annu Rev Biochem, 2010. **79**: p. 213-31.

157. Protasio, A.V., et al., *MiR-277/4989 regulate transcriptional landscape during juvenile to adult transition in the parasitic helminth Schistosoma mansoni.* PLoS Negl Trop Dis, 2017. **11**(5): p. e0005559.

158. Hyman, L., *The Invertebrates: Platyhelminthes and Rhynchocoela The Acoelomate Bilateria*. Vol. II. 1951, New York: McGraw-Hill Book Company, Inc. 550.

159. Buzgariu, W., et al., *Multi-functionality and plasticity characterize epithelial cells in Hydra.* Tissue Barriers, 2015. **3**(4): p. e1068908.

160. Watt, F.M., *Stem cell fate and patterning in mammalian epidermis.* Curr Opin Genet Dev, 2001. **11**(4): p. 410-7.

161. Newmark, P.A. and A. Sanchez Alvarado, *Bromodeoxyuridine specifically labels the regenerative stem cells of planarians.* Dev Biol, 2000. **220**(2): p. 142-53.

162. Wagner, D.E., J.J. Ho, and P.W. Reddien, *Genetic regulators of a pluripotent adult stem cell system in planarians identified by RNAi and clonal analysis.* Cell Stem Cell, 2012. **10**(3): p. 299-311.

163. Wurtzel, O., et al., *A Generic and Cell-Type-Specific Wound Response Precedes Regeneration in Planarians.* Dev Cell, 2015. **35**(5): p. 632-45.

164. Egger, B., et al., *A transcriptomic-phylogenomic analysis of the evolutionary relationships of flatworms.* Curr Biol, 2015. **25**(10): p. 1347-53.

165. Wang, B., et al., *Stem cell heterogeneity drives the parasitic life cycle of Schistosoma mansoni.* Elife, 2018. **7**.

166. Dillon, G.P., et al., *Patterns of gene expression in schistosomes: localization by whole mount in situ hybridization.* Parasitology, 2007. **134**(Pt 11): p. 1589-97.

167. Lu, Z., et al., *Schistosome sex matters: a deep view into gonad-specific and pairing-dependent transcriptomes reveals a complex gender interplay.* Sci Rep, 2016. **6**: p. 31150.

168. Wilson, R.A. and L.A. Webster, *Protonephridia.* Biol Rev Camb Philos Soc, 1974. **49**(2): p. 127-60.

169. Cote, L.E., E. Simental, and P.W. Reddien, *Muscle functions as a connective tissue and source of extracellular matrix in planarians.* Nat Commun, 2019. **10**(1): p. 1592.

170. Grimes, D.T., *Making and breaking symmetry in development, growth and disease.* Development, 2019. **146**(16).

171. Grande, C. and N.H. Patel, *Nodal signalling is involved in left-right asymmetry in snails.* Nature, 2009. **457**(7232): p. 1007-11.

172. Nogi, T., et al., *Eye regeneration assay reveals an invariant functional left-right asymmetry in the early bilaterian, Dugesia japonica.* Laterality, 2005. **10**(3): p. 193-205.

173. Reddien, P.W., et al., *BMP signaling regulates the dorsal planarian midline and is needed for asymmetric regeneration.* Development, 2007.

174. Witchley, J.N., et al., *Muscle cells provide instructions for planarian regeneration.* Cell Rep, 2013. **4**(4): p. 633-41.

175. Popiel, I., D.L. Irving, and P.F. Basch, *Wound healing in the trematode Schistosoma.* Tissue Cell, 1985. **17**(1): p. 69-77.

176. Pearce, E.J. and A.S. MacDonald, *The immunobiology of schistosomiasis.* Nat Rev Immunol, 2002. **2**(7): p. 499-511.

177. Nollen, P.M., et al., *The timing of reproductive cell development and movement in Schistosoma mansoni, S. japonicum, and S. haematobium, using techniques of autoradiography and transplantation.* J Parasitol, 1976. **62**(2): p. 227-31.

178. Galanti, S.E., S.C. Huang, and E.J. Pearce, *Cell death and reproductive regression in female Schistosoma mansoni.* PLoS Negl Trop Dis, 2012. **6**(2): p. e1509.

179. Shaw, M.K. and D.A. Erasmus, *Schistosoma mansoni: the presence and ultrastructure of vitelline cells in adult males.* J Helminthol, 1982. **56**(1): p. 51-3.

180. Vogel, H., *Hermaphrodites of Schistosoma mansoni.* Ann Trop Med Parasitol, 1947. **41**(2): p. 266-77.

181. Petersen, C.P. and P.W. Reddien, *Wnt signaling and the polarity of the primary body axis.* Cell, 2009. **139**(6): p. 1056-68.

182. Morris, G.P., *Fine structure of the gut epithelium of Schistosoma mansoni.* Experientia, 1968. **24**(5): p. 480-2.

183. Caffrey, C.R., et al., *Cysteine proteases as digestive enzymes in parasitic helminths.* PLoS Negl Trop Dis, 2018. **12**(8): p. e0005840.

184. Jílková, A., et al., *Structural basis for inhibition of cathepsin B drug target from the human blood fluke, Schistosoma mansoni.* J Biol Chem, 2011. **286**(41): p. 35770-81.

185. Palanker, L., et al., *Drosophila HNF4 regulates lipid mobilization and beta-oxidation.* Cell Metab, 2009. **9**(3): p. 228-39.

186. Yuan, X., et al., *Identification of an endogenous ligand bound to a native orphan nuclear receptor.* PLoS One, 2009. **4**(5): p. e5609.

187. McVeigh, P., et al., *RNAi dynamics in Juvenile Fasciola spp. Liver flukes reveals the persistence of gene silencing in vitro.* PLoS Negl Trop Dis, 2014. **8**(9): p. e3185.

188. Anandanarayanan, A., et al., *RNA interference in Fasciola gigantica: Establishing and optimization of experimental RNAi in the newly excysted juveniles of the fluke.* PLoS Negl Trop Dis, 2017. **11**(12): p. e0006109.

189. Sripa, J., et al., *RNA interference targeting cathepsin B of the carcinogenic liver fluke, Opisthorchis viverrini.* Parasitol Int, 2011. **60**(3): p. 283-8.

190. Wang, X., et al., *RNAi-mediated silencing of enolase confirms its biological importance in Clonorchis sinensis.* Parasitol Res, 2014. **113**(4): p. 1451-8.

Figure 1.1

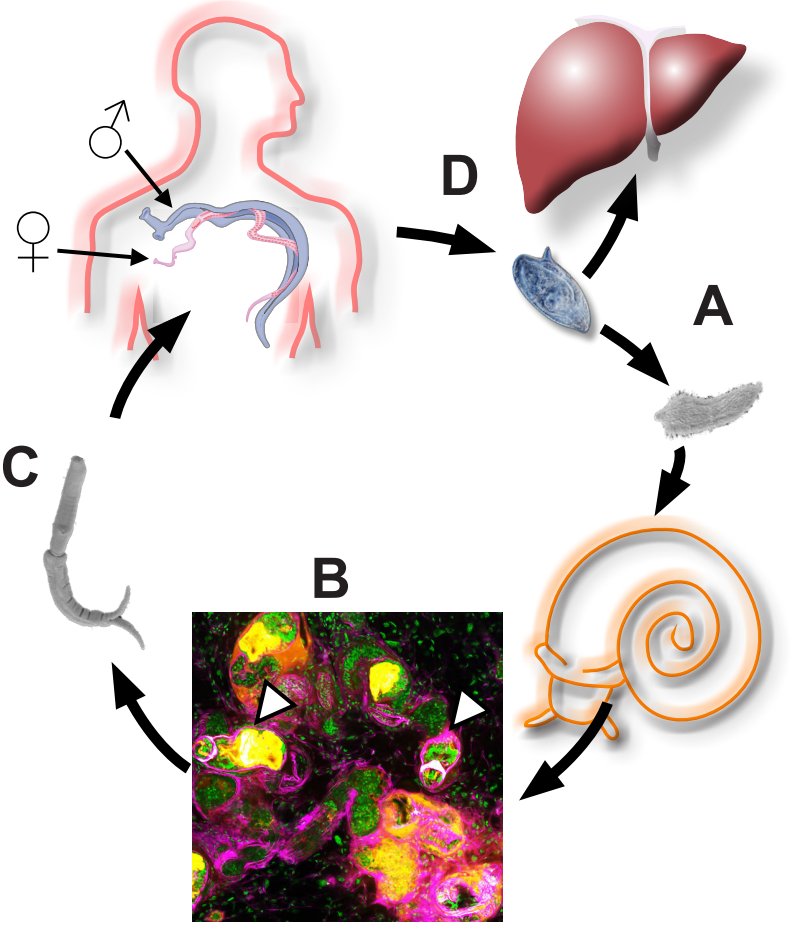

FIGURE 1.1: Schistosome life cycle

(A) *Schistosoma mansoni* eggs hatch in freshwater to give rise to the first larval stage, the free swimming ciliated miracidia. (B) Upon finding a susceptible snail, the miracidia will penetrate through the snail's tissues and transform into the next larval stage referred to as the sporocyst. (C) Sporocysts undergo asexual embryogenesis to eventually produce the next larval stage, the infectious cercaria. Cercaria use their flagella-like tail to traverse through water until finding a suitable definitive host, i.e., a human. The cercaria then penetrates through the host's skin and enters the bloodstream where they transform over the course of several weeks into adult parasites. Male and female parasites physically pair together and the females begin producing eggs. (D) To complete the lifecycle, these eggs must leave the blood and enter the intestinal lumen in order to escape into the environment, but the process of leaving the vasculature is inefficient. Large quantities of eggs become trapped in host tissues such as the liver where they induce a massive inflammatory response, which ultimately leads to the pathology of schistosomiasis.

Figure 1.2

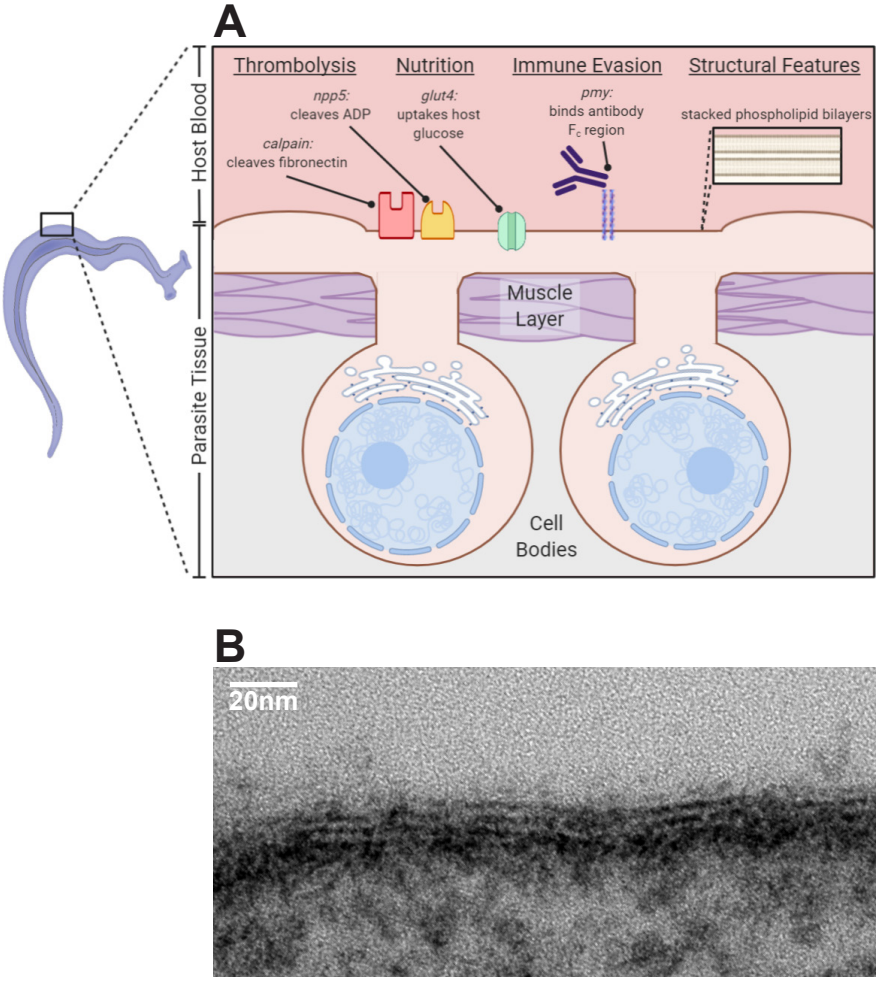
A
Thrombolysis
Nutrition
Immune Evasion
Structural Features
npp5:
cleaves ADP
calpain:
cleaves fibronectin
glut4:
uptakes host
glucose
pmy:
binds antibody
Fc region
stacked phospholipid bilayers
Host Blood
Parasite Tissue
Muscle
Layer
Cell
Bodies
B
20nm

FIGURE 1.2: The schistosome tegument

(A) Cartoon depicting some of the molecular features of the schistosome tegument. The tegument is believed to play roles in thrombolysis, nutrient acquisition, and immune evasion. It also possesses unique multi-laminate surface membranes. (B) A TEM depicting the multi-laminate structure of the plasma membrane at the surface of the tegument. Scale bar: 20nm.

Figure 2.1

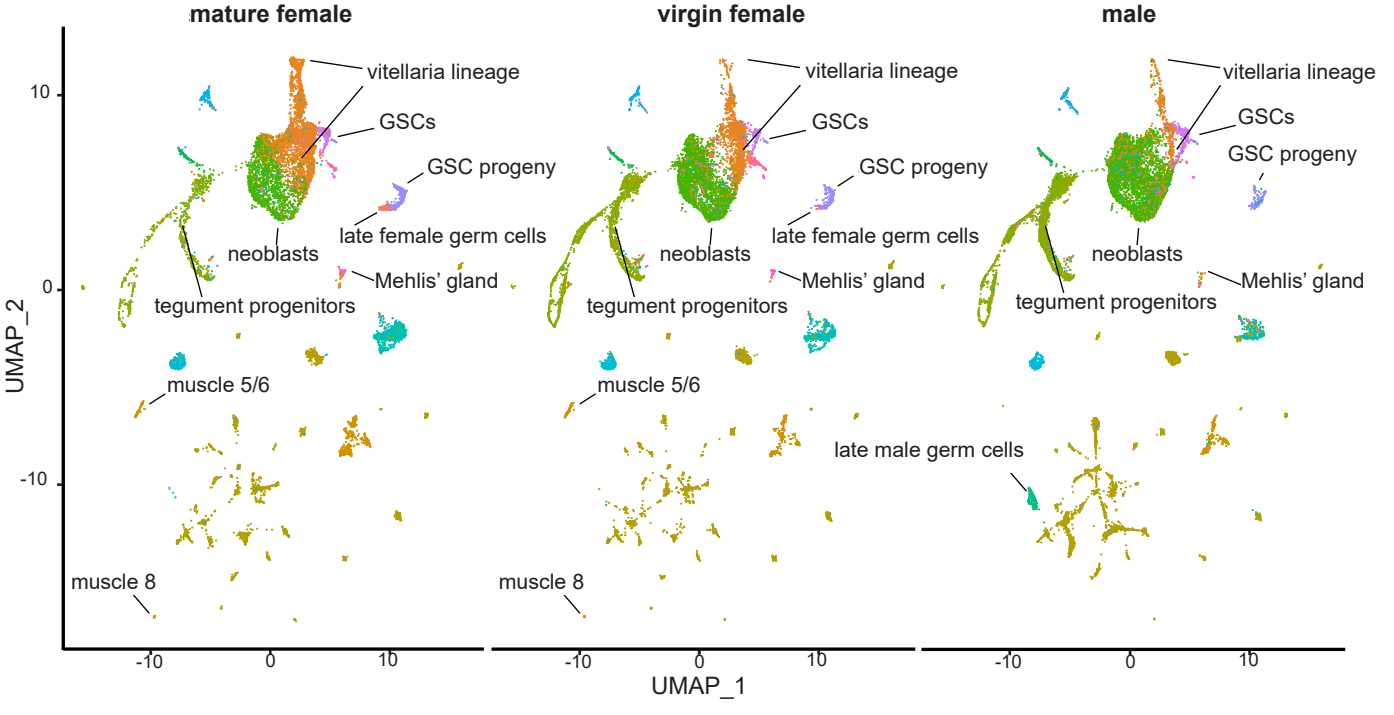
mature female
virgin female
male
vitellaria lineage
GSCs
GSC progeny
late female germ cells
neoblasts
Mehlis' gland
tegument progenitors
muscle 5/6
muscle 8
late male germ cells
UMAP_2
UMAP_1
10
0
-10

FIGURE 2.1: Different scRNAseq normalization methods produce the same results

UMAP plot showing the scRNAseq data reclustered using sctransform instead of the standard Seurat workflow. Relevant clusters are labeled.

Figure 3.1

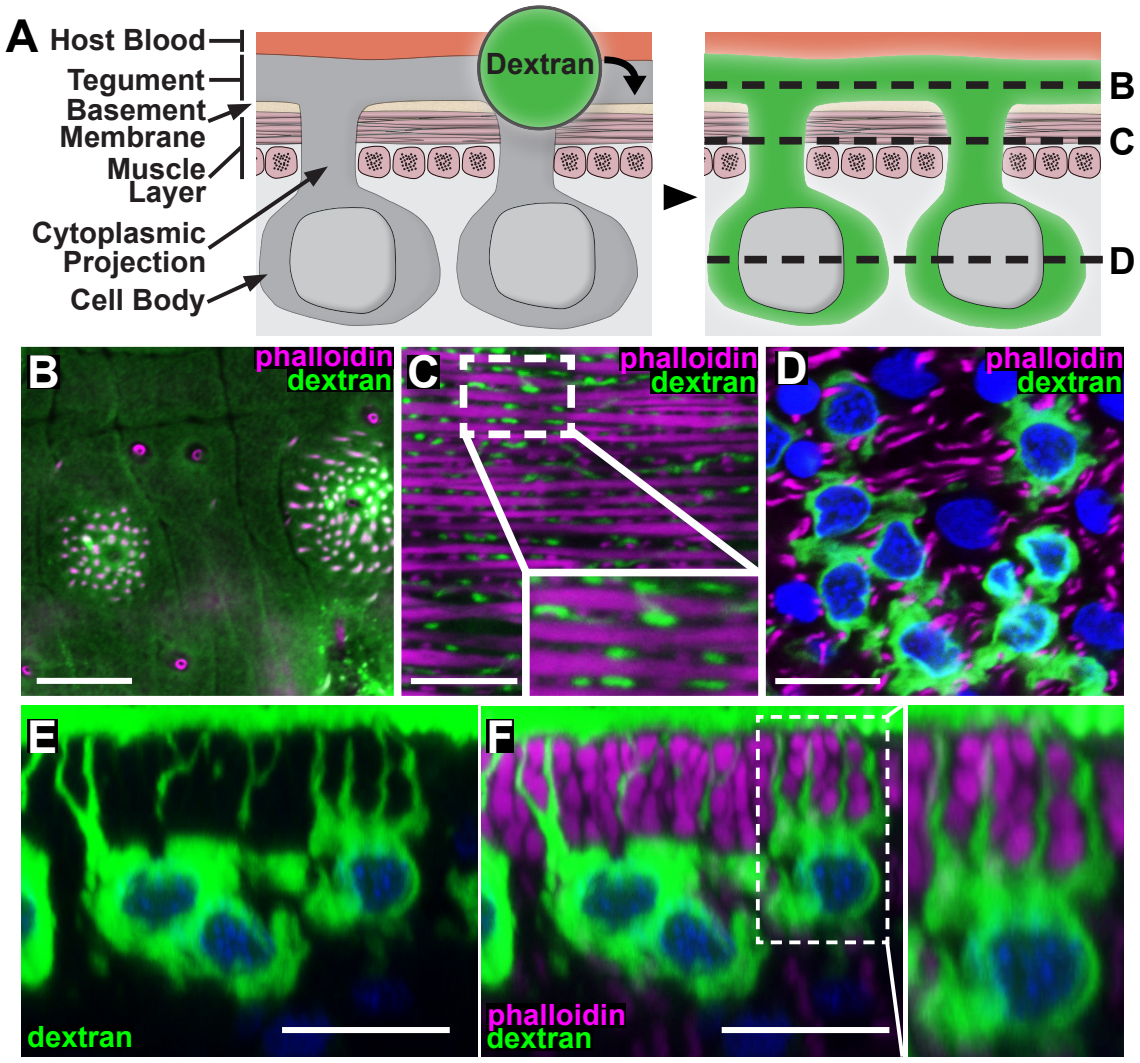
A
Host Blood
Tegument
Basement Membrane
Muscle Layer
Cytoplasmic Projection
Cell Body
Dextran
B
C
D
B
phalloidin
dextran
C
phalloidin
dextran
D
phalloidin
dextran
E
dextran
F
phalloidin
dextran

FIGURE 3.1: Fluorescent dextran labels the schistosome tegument

(A) Cartoon depicting anatomy of the tegument and fluorescent dextran labeling. (B-D) Transverse planes through various levels of the tegument as indicated in (A). Muscle cells are labelled with phalloidin and tegumental cells are labeled with fluorescent dextran. (E-F) Side view of the dextran-labeled tegument depicting cytoplasmic projections extending from the cell bodies to the surface of the tegument, (F) intercalating between phalloidin-labeled muscle fibers. Scale bars: 10μm.

Figure 3.2

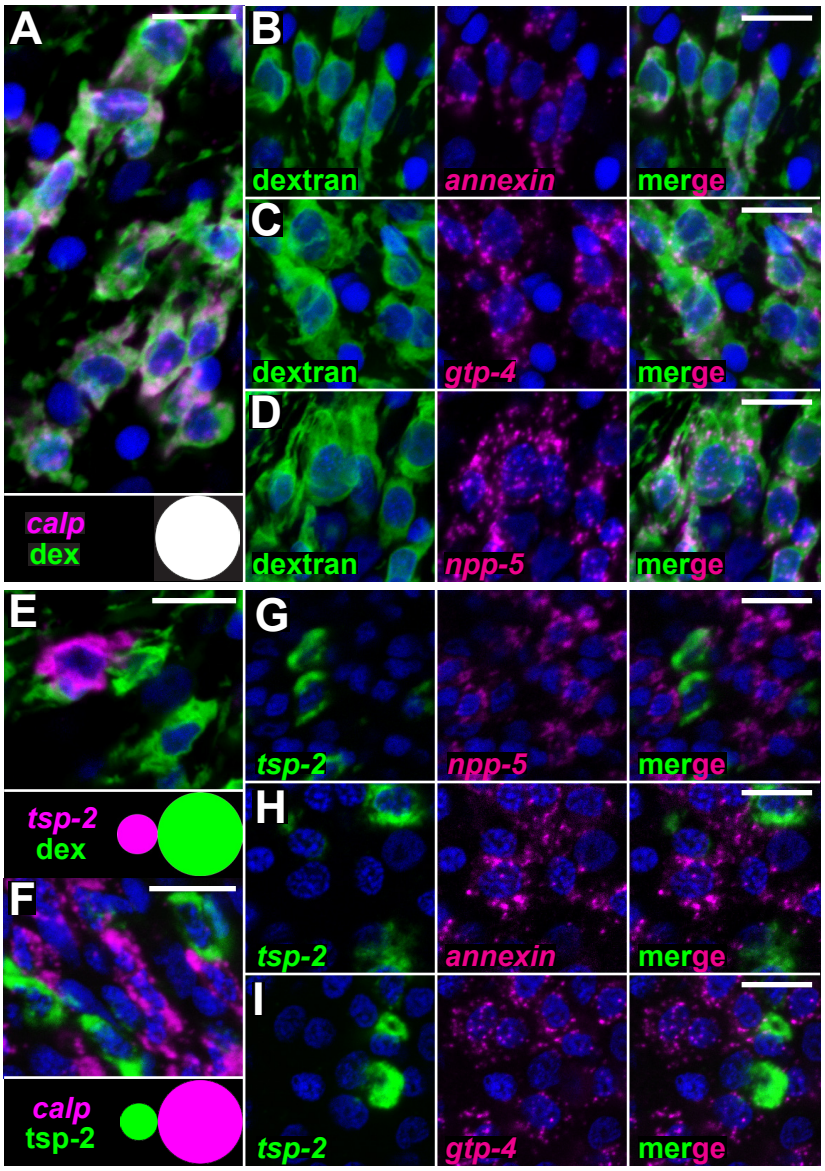
A
calp
dex
B
dextran
annexin
merge
C
dextran
gtp-4
merge
D
dextran
npp-5
merge
E
tsp-2
dex
F
calp
tsp-2
G
tsp-2
npp-5
merge
H
tsp-2
annexin
merge
I
tsp-2
gtp-4
merge

FIGURE 3.2: tsp-2+ neoblast progeny cells are not tegumental cells

(A-E) FISH experiments demonstrating the localization of (A) *calp* expression (*n* = 222 cells from 3 adult male parasites), (B) *annexin* expression (*n* = 216 cells from 3 adult male parasites), (C) *gtp-4* expression (*n* = 172 cells from 3 adult male parasites), (D) *npp-5* expression (*n* = 199 cells from 3 adult male parasites), and (E) *tsp-2* expression relative to the dextran-labeled tegumental cells (*n* = 233 cells from 3 adult male parasites). Insets show a Venn diagram illustrating the relative overlap of cell populations. (G-I) double FISH experiment demonstrating the localization of *tsp-2* expression relative to (F) *calp* expression (*n* = 275 cells from 3 adult male parasites), (G) *npp-5* expression (*n* = 492 cells from 3 adult male parasites), (H) *annexin* expression (*n* = 237 cells from 3 adult male parasites), and (I) *gtp-4* expression (*n* = 255 cells from 3 adult male parasites). Scale bars: 10μm.

Figure 3.3

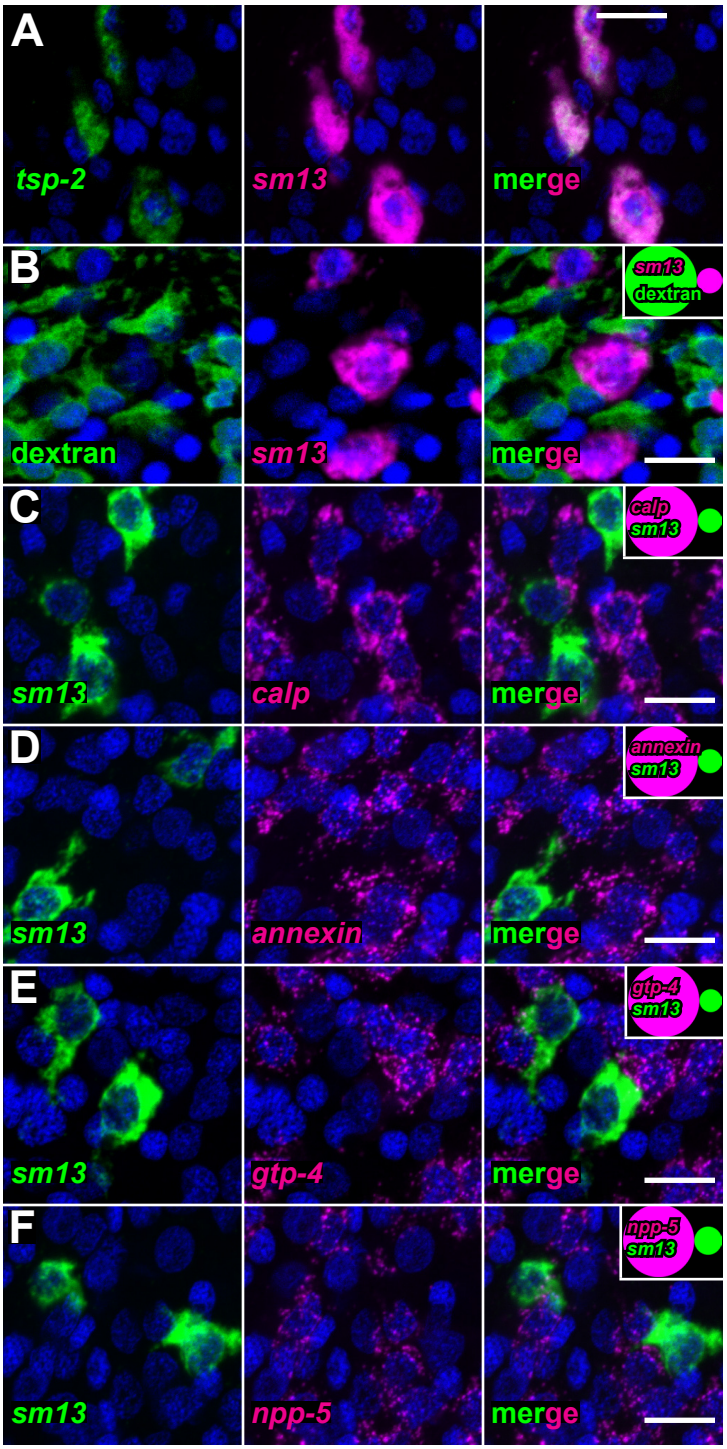
A
tsp-2
sm13
merge
B
dextran
sm13
merge
sm13
dextran
C
sm13
calp
merge
calp
sm13
D
sm13
annexin
merge
annexin
sm13
E
sm13
gtp-4
merge
gtp-4
sm13
F
sm13
npp-5
merge
npp-5
sm13

FIGURE 3.3: The neoblast progeny marker sm13 colocalizes with tsp-2 but not with definitive tegument markers

(A) Double FISH experiment demonstrating the localization of *tsp-2* expression relative to *sm13* expression (*n* = 240 cells from 3 adult male parasites). (B) FISH experiment on dextran-labeled worms demonstrating the localization of *sm13* expression relative to dextran-labeled tegumental cells (*n* = 372 cells from 2 adult male parasites). (C-F) Double FISH experiments demonstrating the localization of (C) *calp* expression (*n* = 291 cells from 3 adult male parasites), (D) *annexin* expression (*n* = 287 cells from 3 adult male parasites), (E) *gtp-4* expression (*n* = 328 cells from 3 adult male parasites), and (F) *npp-5* expression (*n* = 269 cells from 3 adult male parasites) relative to *sm13* expression. Insets show a Venn diagram illustrating the relative overlap of cell populations with white representing co-expression. Scale bars: 10μm.

Figure 3.4

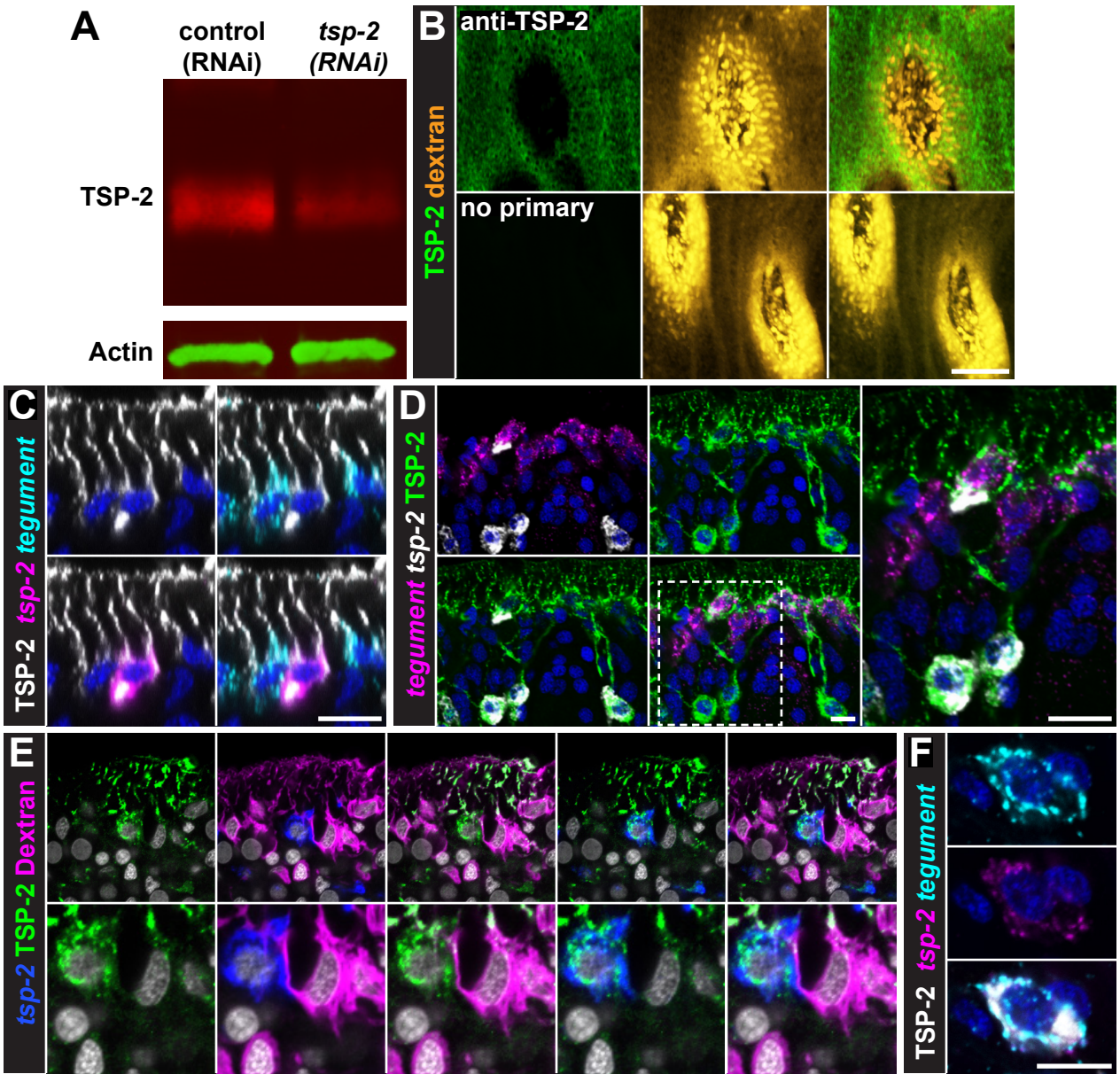
A
control (RNAi)
tsp-2 (RNAi)
TSP-2
Actin
B
anti-TSP-2
no primary
TSP-2 dextran
C
TSP-2 tsp-2 tegument
D
tegument tsp-2 TSP-2
E
tsp-2 TSP-2 Dextran
F
TSP-2 tsp-2 tegument

FIGURE 3.4: TSP-2 protein is present in tsp-2+ neoblast progeny and in the mature tegument

(A) Western blot showing depletion of *TSP-2* protein levels following *tsp-2* RNAi. (B) Transverse image at tegument surface demonstrating the specificity of surface labeling of the parasite using anti-*TSP-2* antibody. (C) Immunofluorescence in conjunction with FISH demonstrating that *TSP-2* protein is found in both *tsp-2*-expressing cells and in the cells expressing a mixture of tegument markers ("tegument"). (D) Double FISH experiment with immunofluorescence demonstrating that *TSP-2* protein is found in both *tsp-2* mRNA^{+} cells as well as in mature tegumental cells. (E) FISH experiment in conjunction with dextran-labeling and immunofluorescence demonstrating that *TSP-2* protein is found in both *tsp-2* mRNA^{+} cells as well as in mature tegumental cells. (F) Image of a rare *tsp-2* mRNA expressing tegumental cell that is also *TSP-2* protein positive. Scale bars: 10μm.

Figure 3.5

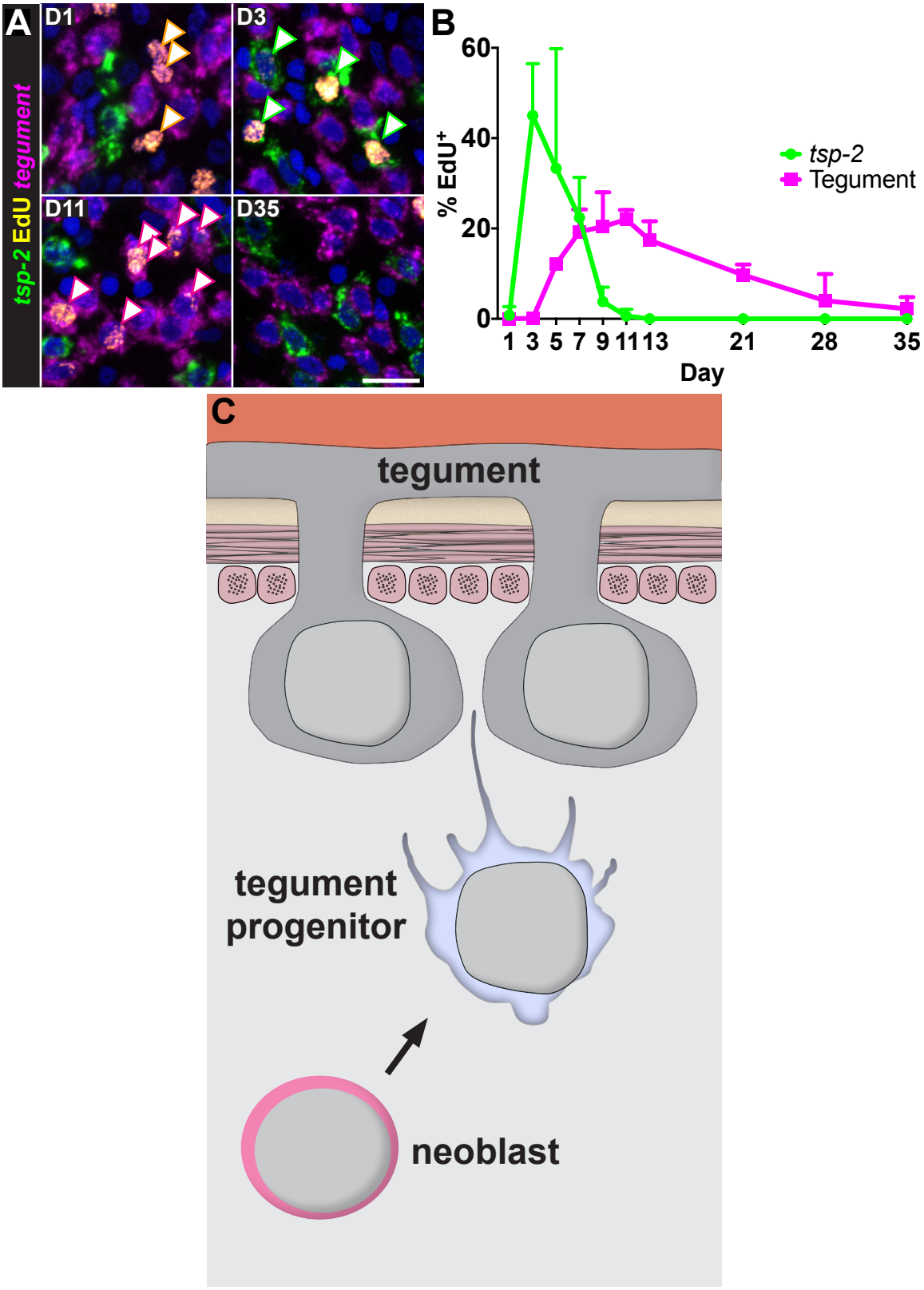
A
D1
D3
D11
D35
tsp-2 EdU tegument
B
% EdU+
60
40
20
0
1 3 5 7 9 11 13 21 28 35
Day
tsp-2
Tegument
C
tegument
tegument progenitor
neoblast

FIGURE 3.5: tsp-2+ neoblast progeny behave like tegument progenitors

(A) EdU pulse-chase experiment examining the kinetics of EdU incorporation into *tsp-2*$^{+}$ cells and definitive tegumental cells. We find that EdU is incorporated into *tsp-2*$^{+}$ cells prior to incorporation into cells expressing tegumental markers, consistent with short lived *tsp-2*-expressing progenitors going on to become mature tegumental cells (*n* = ~130 cells per animal from 6 adult male parasites per time point). (B) Quantification of EdU incorporation in *tsp-2*$^{+}$ and tegumental cells. (C) Model of tegument production: neoblasts make a transient progenitor that eventually becomes a tegumental cell. Error bars represent 95% confidence intervals. Scale bars: 10μm.

Figure 4.1

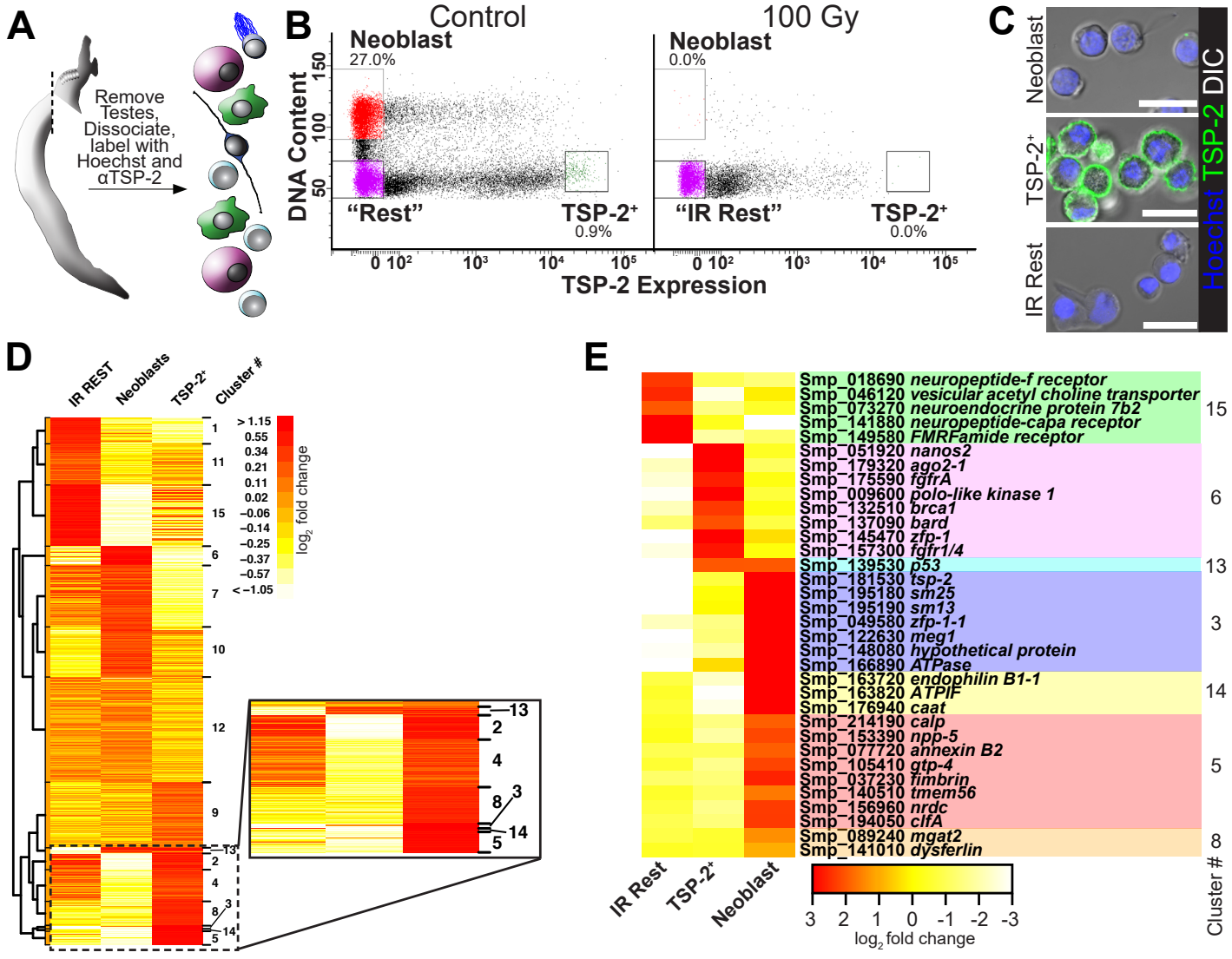
A
Remove Testes, Dissociate, label with Hoechst and αTSP-2
B
Control
100 Gy
Neoblast
27.0%
0.0%
DNA Content
"Rest"
"IR Rest"
TSP-2⁺
0.9%
0.0%
TSP-2 Expression
C
Neoblast
TSP-2⁺
IR Rest
Hoechst TSP-2 DIC
D
IR REST
Neoblasts
TSP-2⁺
Cluster #
log2 fold change
E
Smp_018690 neuropeptide-f receptor
Smp_046120 vesicular acetyl choline transporter
Smp_073270 neuroendocrine protein 7b2
Smp_141880 neuropeptide-capa receptor
Smp_149580 FMRFamide receptor
Smp_051920 nanos2
Smp_179320 ago2-1
Smp_175590 fgfrA
Smp_009600 polo-like kinase 1
Smp_132510 brca1
Smp_137090 bard
Smp_145470 zfp-1
Smp_157300 fgfr1/4
Smp_139530 p53
Smp_181530 tsp-2
Smp_195180 sm25
Smp_195190 sm13
Smp_049580 zfp-1-1
Smp_122630 meg1
Smp_148080 hypothetical protein
Smp_166890 ATPase
Smp_163720 endophilin B1-1
Smp_163820 ATPIF
Smp_176940 caat
Smp_214190 calp
Smp_153390 npp-5
Smp_077720 annexin B2
Smp_105410 gtp-4
Smp_037230 fimbrin
Smp_140510 tmem56
Smp_156960 nrdc
Smp_194050 clfA
Smp_089240 mgat2
Smp_141010 dysferlin
IR Rest
TSP-2⁺
Neoblast
log2 fold change
Cluster #

FIGURE 4.1: FACS purification and transcriptional profiling identifies molecules expressed in neoblasts and cells associated with the tegumental lineage

(A) Cartoon depicting FACS purification strategy. (B) FACS plots showing various cell populations in control and following gamma-irradiation. Percentages represent fraction of the number of cells in the box region over the total number of live cells. (C) Confocal micrographs of the sorted cell populations labeled with Hoechst and an anti-*TSP-2* antibody. (D) Heatmap showing clustering analysis of genes expressed in the indicated cell populations. Inset shows *TSP-2* enriched clusters. (E) Heatmap showing the relative expression of individual genes in each cell population. These genes are organized by cluster. Scale bars: 10μm.

Figure 4.2

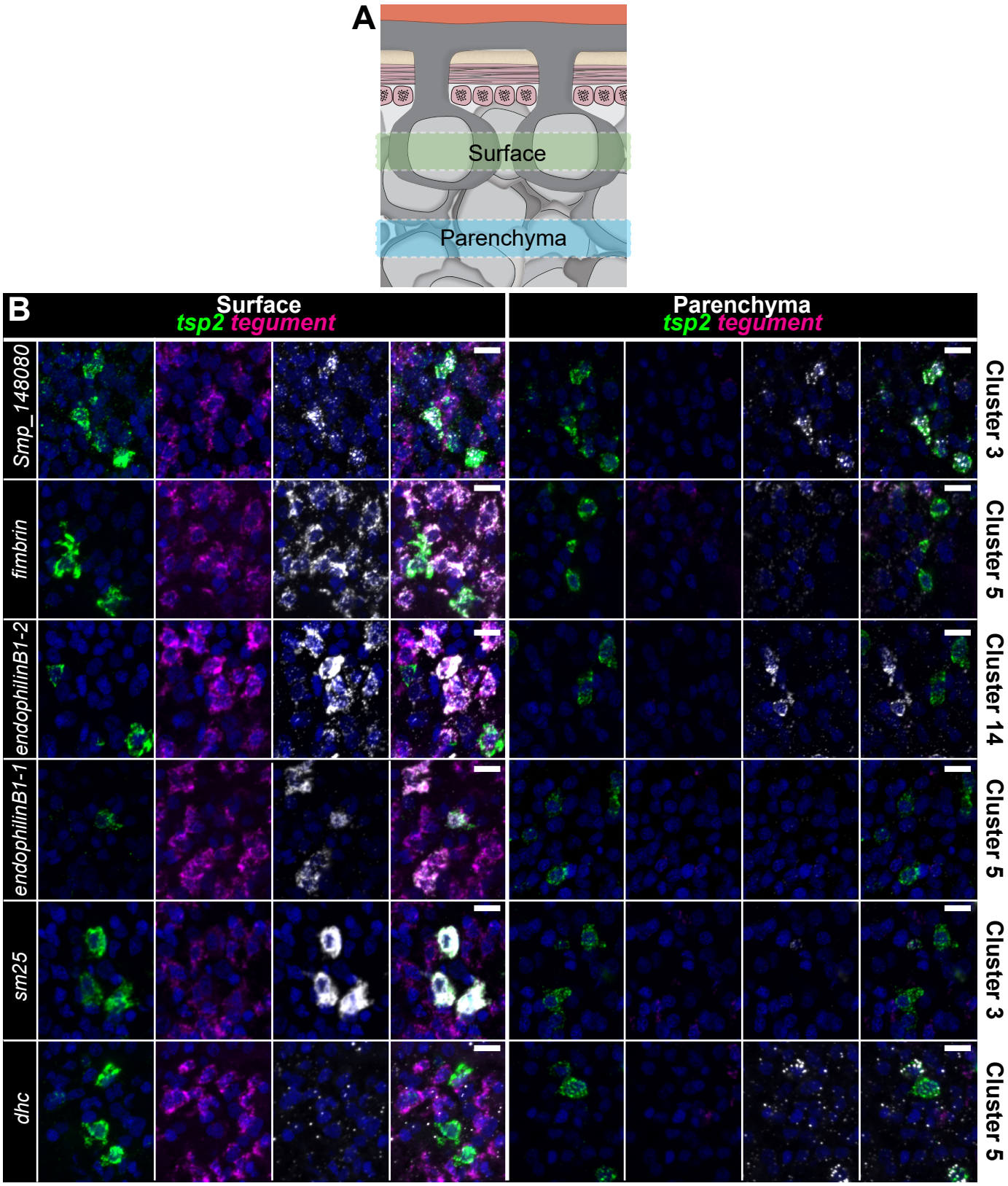
A
Surface
Parenchyma
B
Surface
tsp2 tegument
Parenchyma
tsp2 tegument
Smp_148080
fimbrin
endophilinB1-2
endophilinB1-1
sm25
dhc
Cluster 3
Cluster 5
Cluster 14
Cluster 5
Cluster 3
Cluster 5

Figure 4.2

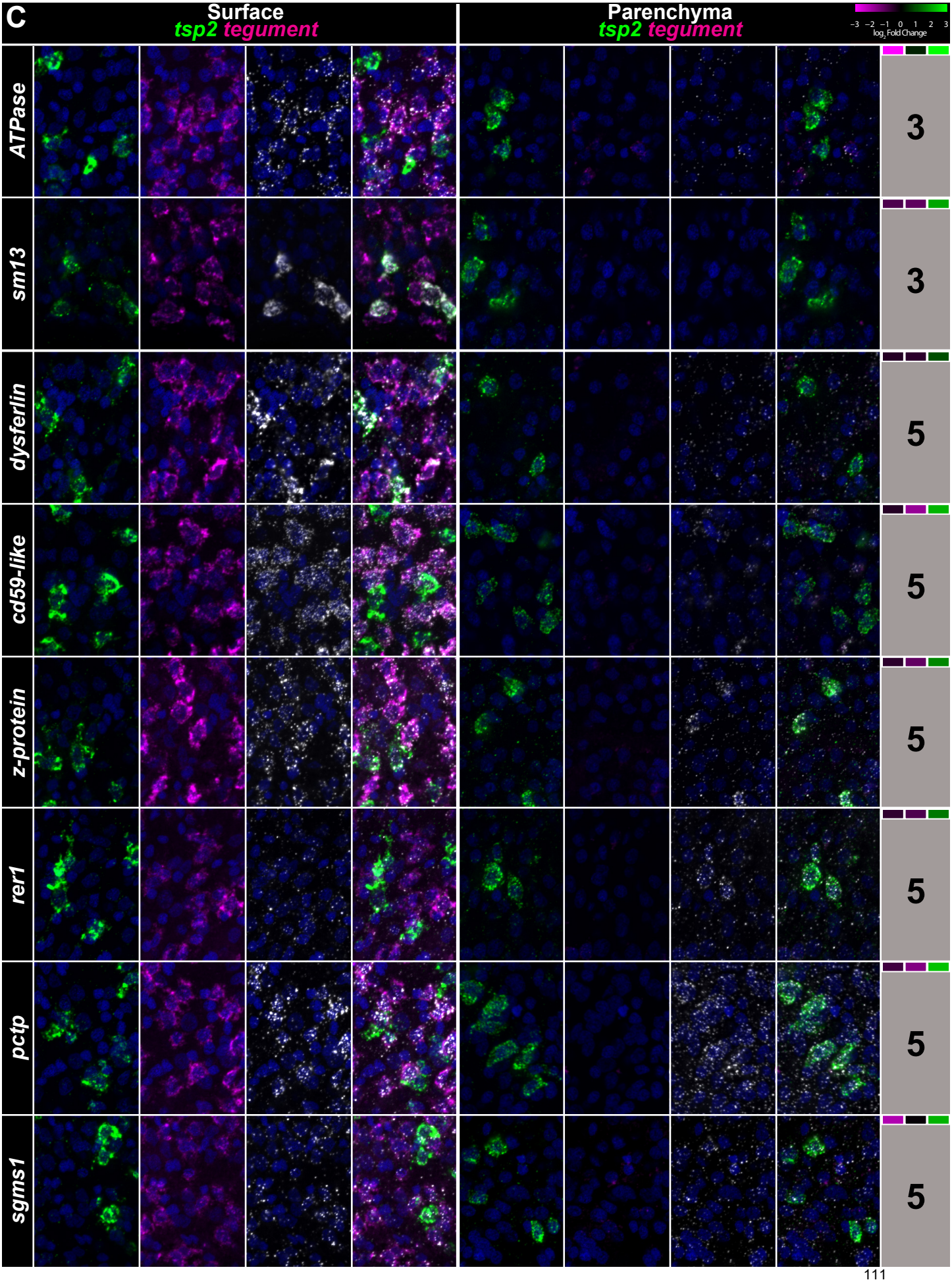
C
Surface
tsp2 tegument
Parenchyma
tsp2 tegument
−3 −2 −1 0 1 2 3
log2 Fold Change
ATPase
3
sm13
3
dysferlin
5
cd59-like
5
z-protein
5
rer1
5
pctp
5
sgms1
5

Figure 4.2

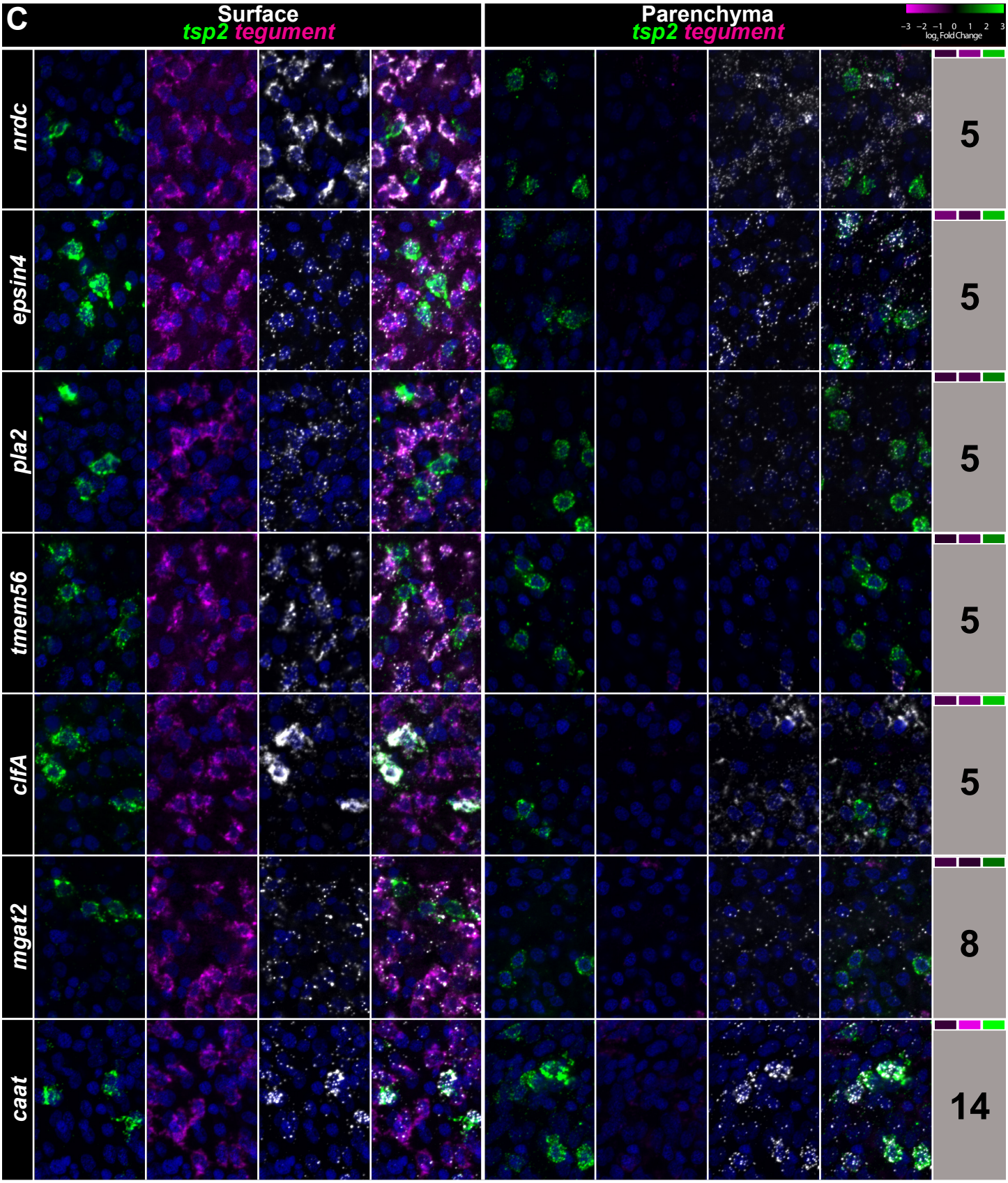
C
Surface
tsp2 tegument
Parenchyma
tsp2 tegument
−3 −2 −1 0 1 2 3
log2 Fold Change
nrdc
epsin4
pla2
tmem56
clfA
mgat2
caat
5
5
5
5
5
8
14

FIGURE 4.2: Examination of the expression of genes expressed in TSP-2-enriched clusters

(A) Cartoon depicting the approximate regions imaged in panel B. (B) FISH for *tsp-2*, a mixture of tegumental makers (“tegument”), and panel of 6 genes from different clusters of gene expression (indicated at right of the image). Images are maximum intensity projections at either the level of the surface (left) or in the parenchyma (right). FISH for *tsp-2*, a mixture of tegumental makers (“tegument”), and panel of 15 additional genes from various clusters of gene expression (indicated at right of the image). Relative expression levels of each gene in IR Rest, Neoblasts, and *TSP-2*$^{+}$ cells are indicated in the heatmap to the right. Images are maximum intensity projections at either the level of the surface (left) or in the parenchyma (right). Scale bars: 10μm.

Figure 4.3

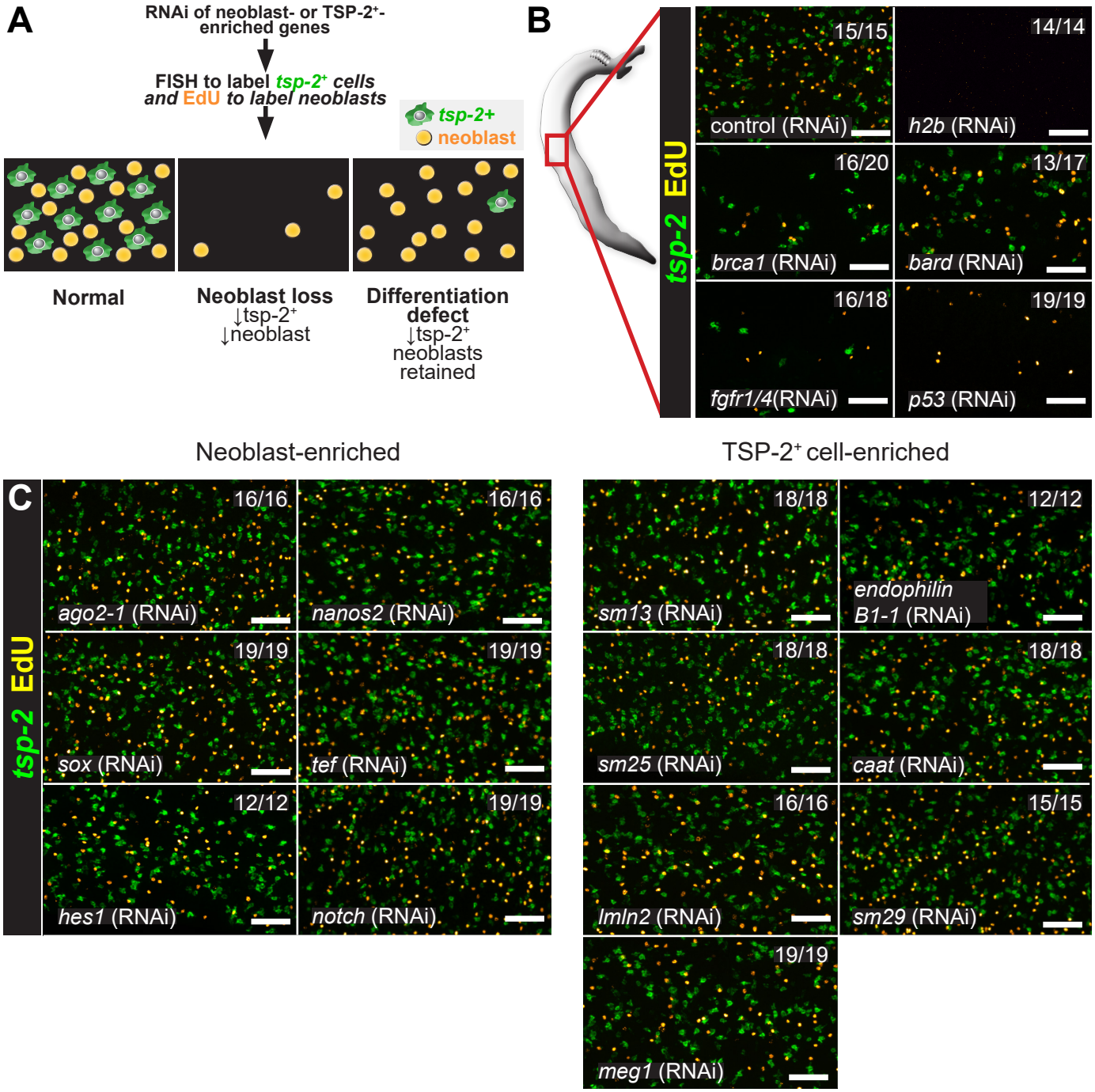
A
RNAi of neoblast- or TSP-2+-enriched genes
FISH to label tsp-2+ cells and EdU to label neoblasts
tsp-2+
neoblast
Normal
Neoblast loss
↓tsp-2+
↓neoblast
Differentiation defect
↓tsp-2+
neoblasts retained
B
tsp-2 EdU
15/15
control (RNAi)
14/14
h2b (RNAi)
16/20
brca1 (RNAi)
13/17
bard (RNAi)
16/18
fgfr1/4(RNAi)
19/19
p53 (RNAi)
Neoblast-enriched
TSP-2+ cell-enriched
C
tsp-2 EdU
16/16
ago2-1 (RNAi)
16/16
nanos2 (RNAi)
19/19
sox (RNAi)
19/19
tef (RNAi)
12/12
hes1 (RNAi)
19/19
notch (RNAi)
18/18
sm13 (RNAi)
12/12
endophilin B1-1 (RNAi)
18/18
sm25 (RNAi)
18/18
caat (RNAi)
16/16
lmln2 (RNAi)
15/15
sm29 (RNAi)
19/19
meg1 (RNAi)

FIGURE 4.3: An RNAi screen to identify regulators of tsp-2+ cell production

(A) Cartoon depicting the RNAi screening strategy used to identify regulators of tegument progenitor specification. Candidate genes were knocked-down using RNAi, worms were pulsed with EdU for 4 hours, then neoblasts and tegument progenitor cells were observed using EdU detection and *tsp-2* RNA FISH, respectively. (B) Negative control RNAi preserves *tsp-2* cells and neoblasts whereas *h2b* RNAi results in a loss of neoblasts and *tsp-2* cells. *brca1*, *bard*, *fgfr1/4*, and *p53* RNAi results in a partial depletion of neoblasts and a proportional decrease in *tsp-2*$^{+}$ cells. (C) Results of knocking down candidate transcripts that are dispensable for normal neoblast function and *tsp-2*$^{+}$ cell production. Representative maximum intensity confocal projections are shown. Numbers represent the fraction of parasites displaying the observed phenotype. Representative maximum intensity confocal projections are shown. Numbers represent the fraction of parasites displaying the observed phenotype. Scale bars: 50μm.

Figure 4.4

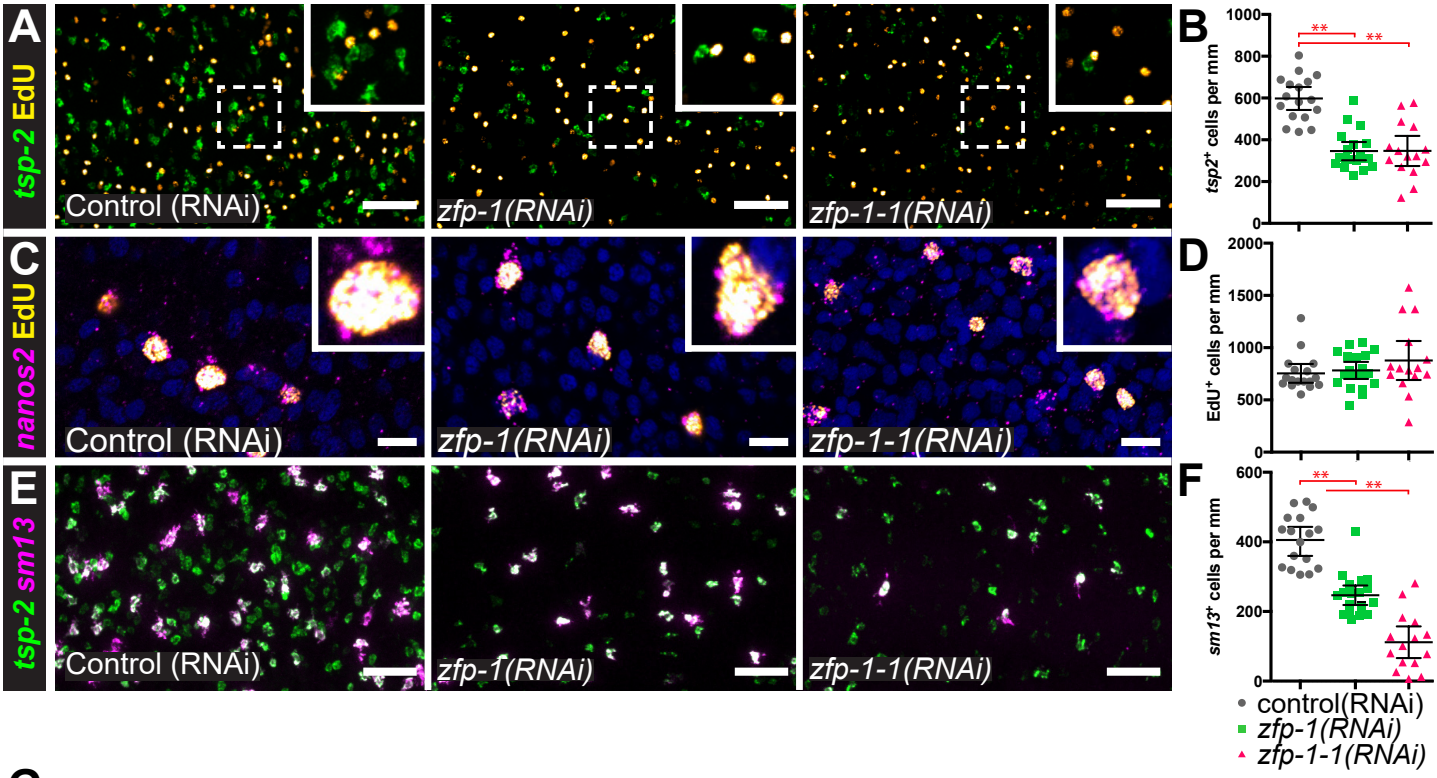
A
tsp-2 EdU
Control (RNAi)
zfp-1(RNAi)
zfp-1-1(RNAi)
B
tsp2+ cells per mm
C
nanos2 EdU
D
EdU+ cells per mm
E
tsp-2 sm13
F
sm13+ cells per mm
control(RNAi)
zfp-1(RNAi)
zfp-1-1(RNAi)

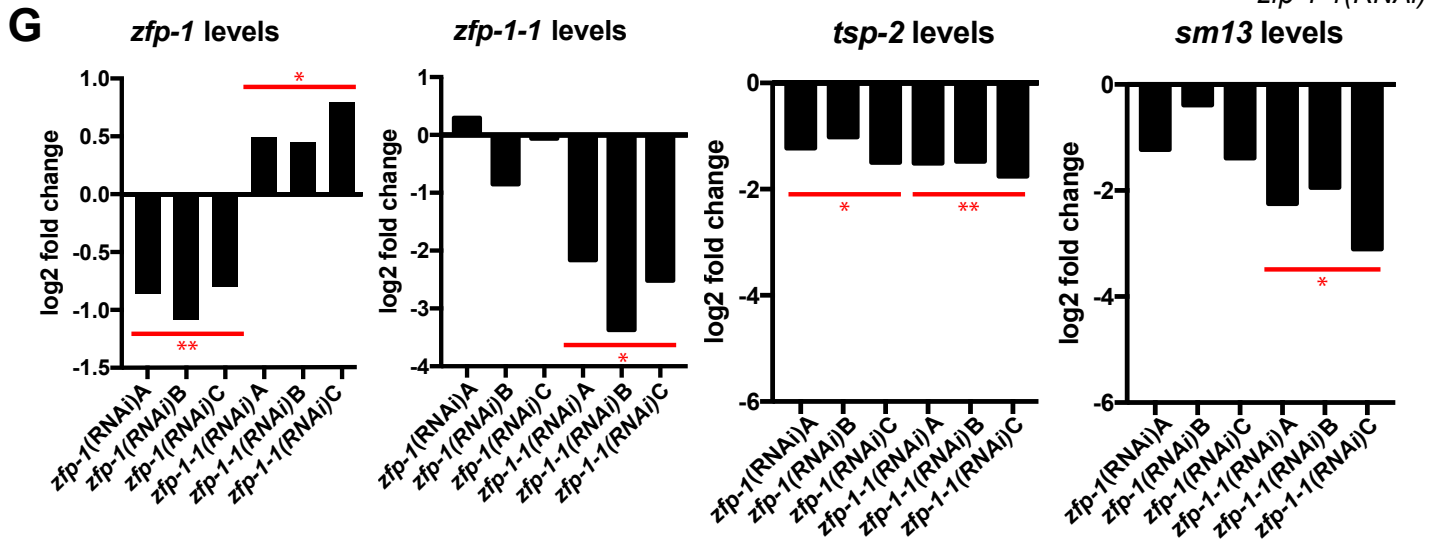
G
zfp-1 levels
zfp-1-1 levels
tsp-2 levels
sm13 levels
log2 fold change
zfp-1(RNAi)A
zfp-1(RNAi)B
zfp-1(RNAi)C
zfp-1-1(RNAi)A
zfp-1-1(RNAi)B
zfp-1-1(RNAi)C

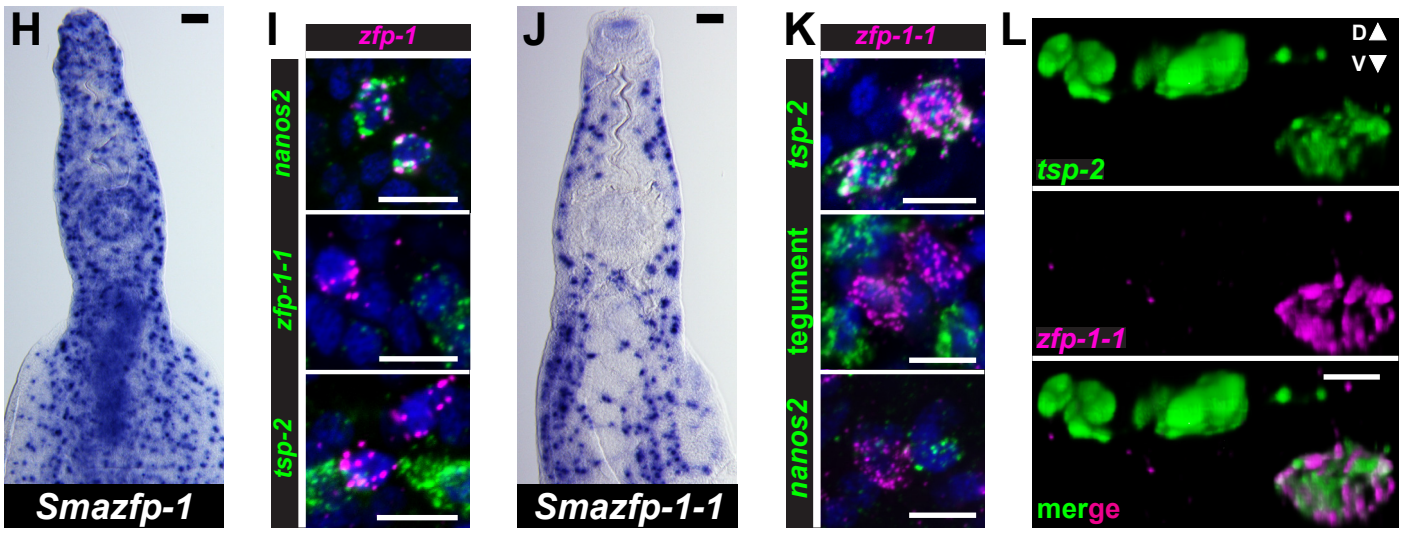
H
Smazfp-1
I
zfp-1
nanos2
zfp-1-1
tsp-2
J
Smazfp-1-1
K
zfp-1-1
tsp-2
tegument
nanos2
L
D▲
V▼
tsp-2
zfp-1-1
merge

FIGURE 4.4: zfp-1 and zfp-1-1 are required for the production of tsp-2+ cells

(A) Maximum intensity projection showing *tsp-2* expression and EdU incorporation in *zfp-1(RNAi)* or *zfp-1-1(RNAi)* parasites. (B) Quantification of the number of *tsp-2*$^{+}$ cells per mm of worm. Control(RNAi) *n* = 17, *zfp-1(RNAi) n* = 19, *zfp-1-1(RNAi) n* = 15. (C) Maximum intensity projection showing *nanos2* expression and EdU incorporation in *zfp-1(RNAi)* or *zfp-1-1(RNAi)* parasites. (D) Quantification of the number of EdU^{+} cells per mm worm. Control(RNAi) *n* = 17, *zfp-1(RNAi) n* = 19, *zfp-1-1(RNAi) n* = 15. (E) Maximum intensity projection showing *tsp-2* and *sm13* expression in *zfp-1(RNAi)* or *zfp-1-1(RNAi)* parasites. (F) Quantification of the number of *sm13*$^{+}$ cells per mm worm. Control(RNAi) *n* = 17, *zfp-1(RNAi) n* = 19, *zfp-1-1(RNAi) n* = 15. (G) Quantitative real time PCR analysis of the effects of *zfp-1* and *zfp-1-1* RNAi on the expression of *zfp-1*, *zfp-1-1*, *sm13*, and *tsp-2*. Each bar represents the expression of the indicated gene from an individual biological replicate relative to the expression from a control RNAi treatment group. Expression levels of indicated genes were normalized to both Cytochrome C Oxidase (Smp_900000) and Proteasome Subunit Beta Type-4 (Smp_056500). (H) WISH showing *zfp-1* expression in adult male worm. (I) Double FISH showing expression of *zfp-1* relative to *nanos2* (a neoblast marker), *zfp-1-1*, and *tsp-2*. (J) WISH showing *zfp-1-1* expression in adult male worm. (K) Double FISH showing expression of *zfp-1-1* relative to *tsp-2*, a mixture tegument-specific markers (tegument), and *nanos2* (a neoblast marker). (L) 3D rendering showing expression of *zfp-1-1* in a subset of *tsp-2*$^{+}$ cells. The dorsal surface of the parasite is oriented toward the top. Scale bars: A, C, E, H, J 50μm; I, K, L 10μm. Error bars represent 95% confidence intervals, * $p < 0.05$, ** $p < 0.01$ (Student's t-test).

Figure 4.5

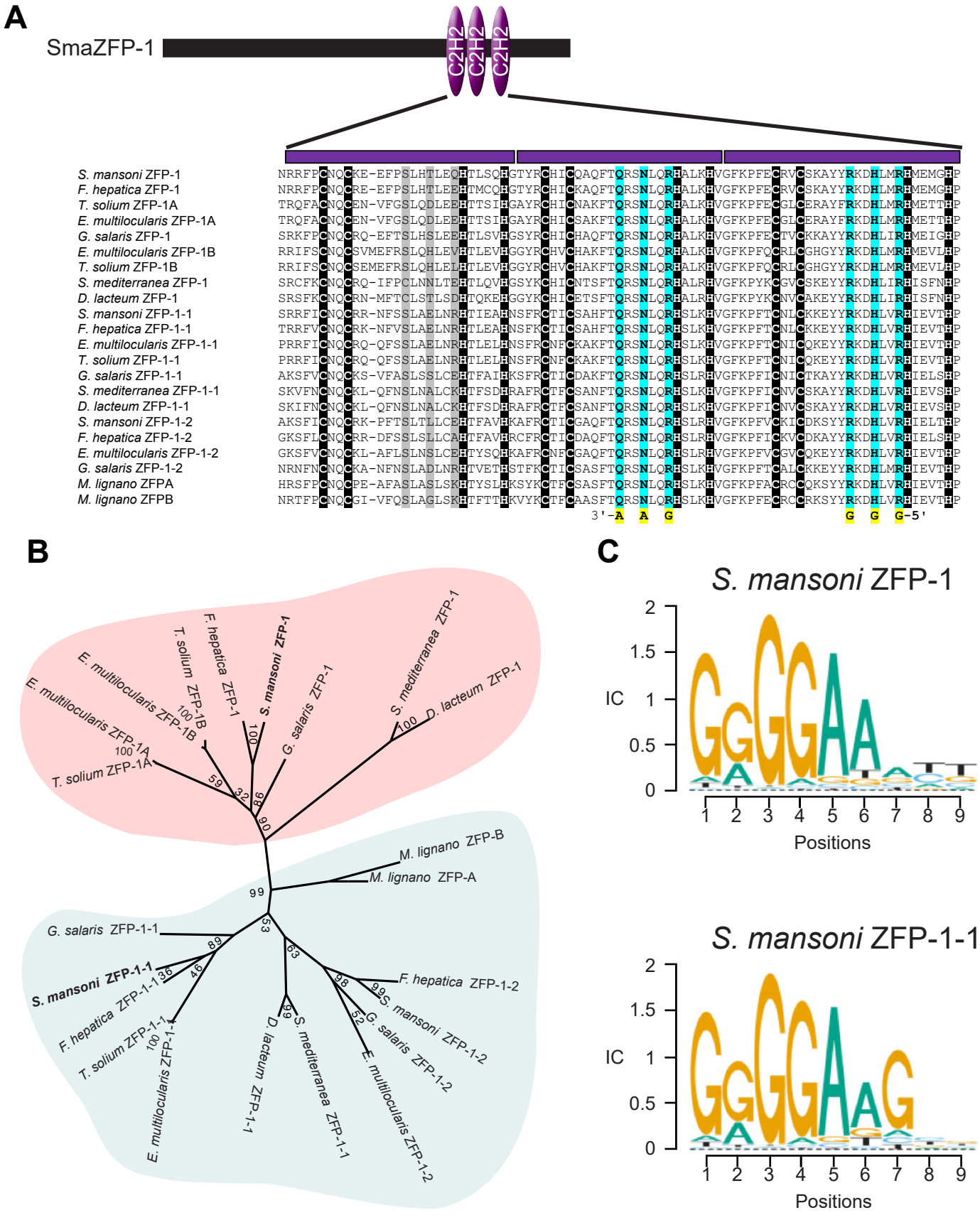
A
SmaZFP-1
C2H2
C2H2
C2H2
S. mansoni ZFP-1
F. hepatica ZFP-1
T. solium ZFP-1A
E. multilocularis ZFP-1A
G. salaris ZFP-1
E. multilocularis ZFP-1B
T. solium ZFP-1B
S. mediterranea ZFP-1
D. lacteum ZFP-1
S. mansoni ZFP-1-1
F. hepatica ZFP-1-1
E. multilocularis ZFP-1-1
T. solium ZFP-1-1
G. salaris ZFP-1-1
S. mediterranea ZFP-1-1
D. lacteum ZFP-1-1
S. mansoni ZFP-1-2
F. hepatica ZFP-1-2
E. multilocularis ZFP-1-2
G. salaris ZFP-1-2
M. lignano ZFPA
M. lignano ZFPB
3'-A A G G G G-5'
B
S. mansoni ZFP-1
F. hepatica ZFP-1
T. solium ZFP-1B
E. multilocularis ZFP-1B
E. multilocularis ZFP-1A
T. solium ZFP-1A
G. salaris ZFP-1
S. mediterranea ZFP-1
D. lacteum ZFP-1
M. lignano ZFP-B
M. lignano ZFP-A
G. salaris ZFP-1-1
S. mansoni ZFP-1-1
F. hepatica ZFP-1-1
T. solium ZFP-1-1
E. multilocularis ZFP-1-1
D. lacteum ZFP-1-1
S. mediterranea ZFP-1-1
E. multilocularis ZFP-1-2
G. salaris ZFP-1-2
S. mansoni ZFP-1-2
F. hepatica ZFP-1-2
C
S. mansoni ZFP-1
IC
Positions
S. mansoni ZFP-1-1
IC
Positions

FIGURE 4.5: ZFP-1 and ZFP-1-1 are flatworm specific zinc finger proteins and are putative transcriptional regulators

(A) Multiple protein sequence alignment of the C2H2 domain of several *zfp-1* and *zfp-1-1* homologs. Zinc coordinating residues are shown in black background. Conserved residues contributing to high specificity DNA-binding are highlighted in cyan for the second and third zinc fingers, with the specific DNA base shown below the residue highlighted in yellow. The corresponding positions in the first zinc finger are shown in grey background. The positions determining DNA binding specificity in the first zinc finger (highlighted in grey background) either are not well conserved among these proteins or do not contribute to high specificity of DNA binding. (B) Un-rooted phylogenic tree of *ZFP-1* and *ZFP-1-1* homologs from multiple species of flatworms. Numbers at the nodes represent bootstrap values. (C) Predicted DNA binding motif of *ZFP-1* and *ZFP-1-1* of *S. mansoni* by the ZFModels server.

Figure 4.6

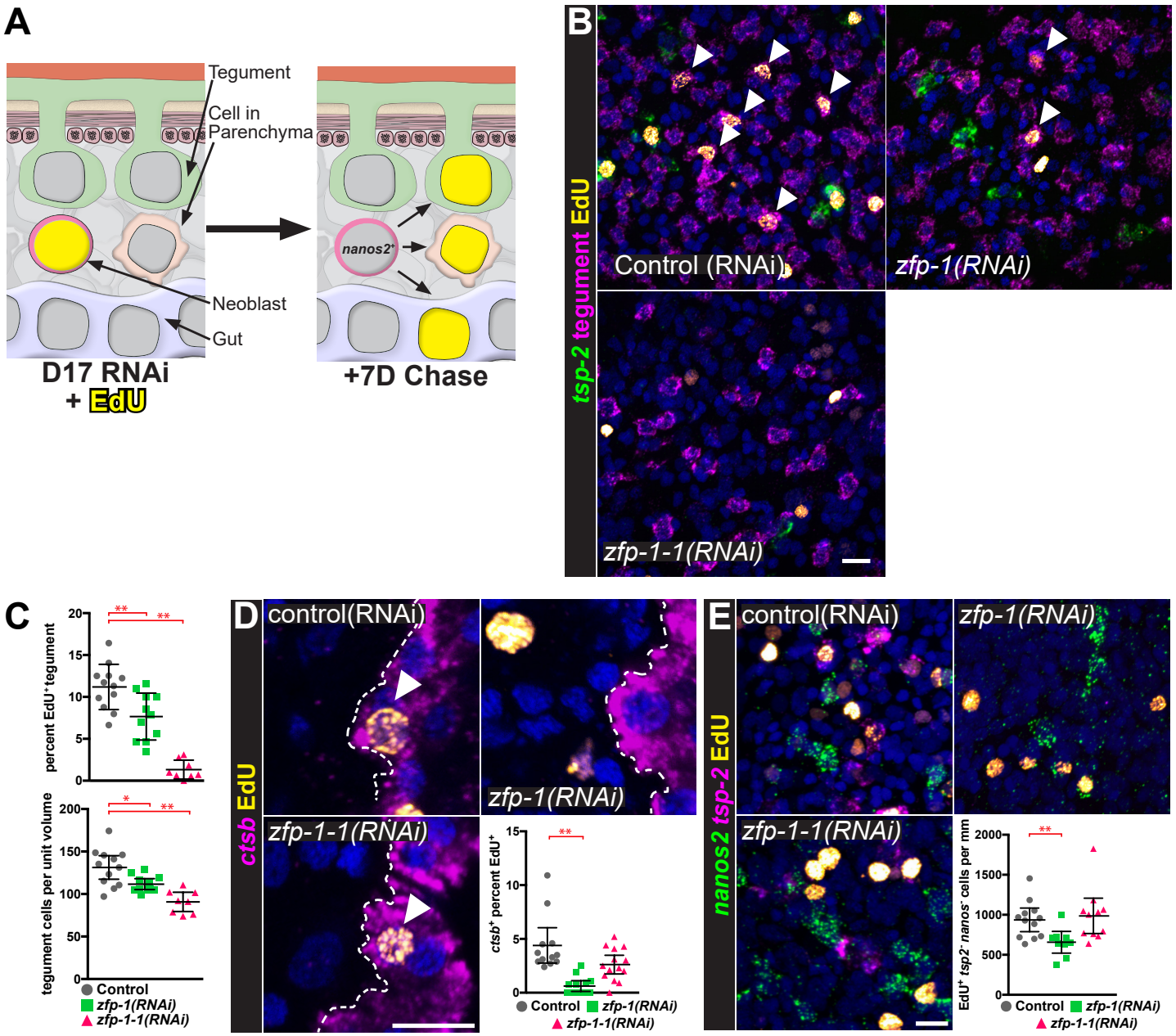
A
Tegument
Cell in Parenchyma
nanos2+
Neoblast
Gut
D17 RNAi
+ EdU
+7D Chase
B
tsp-2 tegument EdU
Control (RNAi)
zfp-1(RNAi)
zfp-1-1(RNAi)
C
percent EdU+ tegument
tegument cells per unit volume
Control
zfp-1(RNAi)
zfp-1-1(RNAi)
D
ctsb EdU
control(RNAi)
zfp-1(RNAi)
zfp-1-1(RNAi)
ctsb+ percent EdU+
E
nanos2 tsp-2 EdU
control(RNAi)
zfp-1(RNAi)
zfp-1-1(RNAi)
EdU+ tsp2- nanos- cells per mm
F
Percent attached
D1
D3
D5
D7
D9
D11
D13
D15
D17
D19
D21
Control(RNAi)
zfp-1(RNAi)
zfp-1-1(RNAi)

FIGURE 4.6: ZFP-1 family proteins are required for the production of new tegumental cells

(A) Cartoon depicting the strategy for fate-mapping by EdU pulse-chase experiments. (B) FISH for *tsp-2* and tegumental markers with EdU detection in *zfp-1(RNAi)* or *zfp-1-1(RNAi)* parasites at day 7 following an EdU pulse. Arrows represent EdU^+ tegumental cells. (C) (Top) Quantification of the percentage of tegumental cells that are EdU^+ following a 7-day chase period and (Bottom) tegumental cell density in *zfp-1(RNAi)* or *zfp-1-1(RNAi)* parasites. Control(RNAi) n = 12, *zfp-1(RNAi)* n = 11, *zfp-1-1(RNAi)* n = 8. (D) FISH for *ctsb* and EdU detection in *zfp-1(RNAi)* or *zfp-1-1(RNAi)* parasites at day 7 following an EdU pulse. Plot represents the percentage of $ctsb^+$ cells that are EdU^+. Control(RNAi) n = 12, *zfp-1(RNAi)* n = 13, *zfp-1-1(RNAi)* n = 14. (E) FISH for *nanos2* and *tsp-2* with EdU detection in *zfp-1(RNAi)* or *zfp-1-1(RNAi)* parasites at day 7 following an EdU pulse. Plot represents the number of $tsp\text{-}2^-$ EdU^+ differentiated cells (i.e., $nanos2^-$ cells) per mm of parasite length. Control(RNAi) n = 12, *zfp-1(RNAi)* n = 10, *zfp-1-1(RNAi)* n = 11. (F) Percentage of the parasites that remain attached to the culture dish at the indicated time point following the first RNAi treatment. n = 5 experiments with approximately 10 worms per RNAi treatment in each experiment. Scale bars: 10μm. Error bars in C-F represent 95% confidence intervals, * $p < 0.05$, ** $p < 0.01$ (Student's t-test).

Figure 4.7

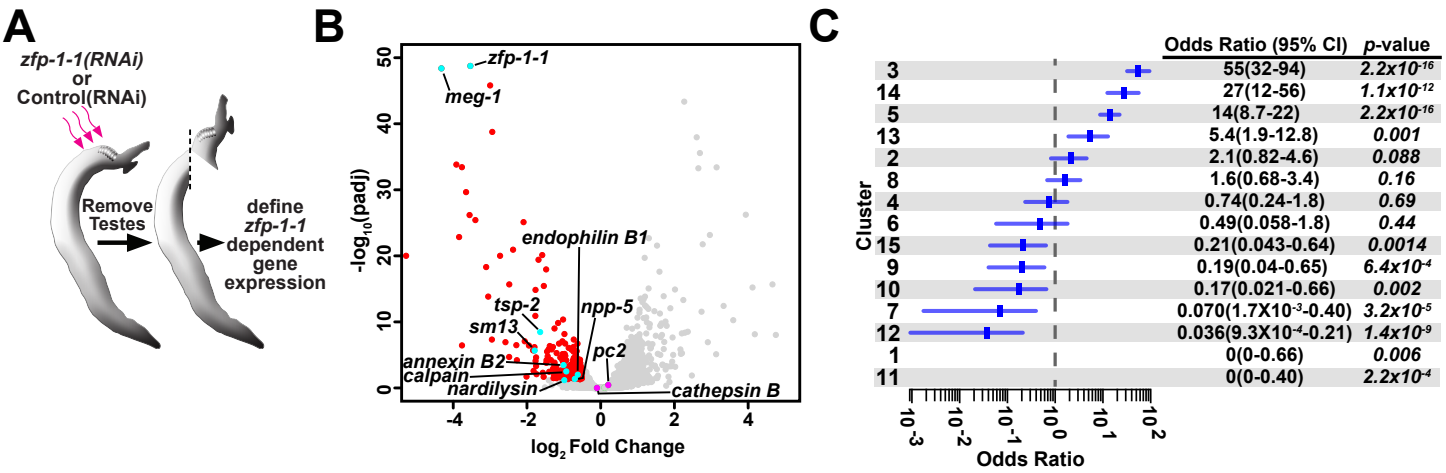
A
zfp-1-1(RNAi)
or
Control(RNAi)
Remove
Testes
define
zfp-1-1
dependent
gene
expression
B
zfp-1-1
meg-1
endophilin B1
tsp-2
npp-5
sm13
pc2
annexin B2
calpain
nardilysin
cathepsin B
-log10(padj)
log2 Fold Change
C
Odds Ratio (95% CI)
p-value
Cluster
3 55(32-94) 2.2x10-16
14 27(12-56) 1.1x10-12
5 14(8.7-22) 2.2x10-16
13 5.4(1.9-12.8) 0.001
2 2.1(0.82-4.6) 0.088
8 1.6(0.68-3.4) 0.16
4 0.74(0.24-1.8) 0.69
6 0.49(0.058-1.8) 0.44
15 0.21(0.043-0.64) 0.0014
9 0.19(0.04-0.65) 6.4x10-4
10 0.17(0.021-0.66) 0.002
7 0.070(1.7X10-3-0.40) 3.2x10-5
12 0.036(9.3X10-4-0.21) 1.4x10-9
1 0(0-0.66) 0.006
11 0(0-0.40) 2.2x10-4
Odds Ratio

FIGURE 4.7: zfp-1-1 RNAi specifically disrupts tegument production

(A) Cartoon depicting strategy for examining transcriptional changes following *zfp-1-1* RNAi. (B) Volcano plot showing differentially expressed genes in *zfp-1-1(RNAi)* worms. Red dots represent genes that are down regulated (-0.5 $\log_2$ fold change, $p_{adj} < 0.05$) in *zfp-1-1(RNAi)* worms. Cyan dots indicate genes known to be expressed in the tegument lineage. Magenta dots indicate genes validated to be expressed in differentiated cells. (C) Plot showing odds-ratio (i.e., the relative over- or under-representation) of genes from gene expression clusters among genes down regulated following *zfp-1-1* RNAi. Blue rectangles depict the odds-ratio from a Fisher's Exact Test, whereas blue lines indicate the 95% confidence intervals. Values of odds-ratio and *p*-values for Fisher's Exact Test shown to right. No genes from expression clusters 1 or 11 were down-regulated following *zfp-1-1* RNAi, so no odds ratio was calculated. From these data, genes from expression clusters 3, 5, 13 and 14 are over-represented ($p < 0.05$), whereas genes from clusters 1, 7, 9, 11, 12, and 15 appear under-represented.

Figure 4.8

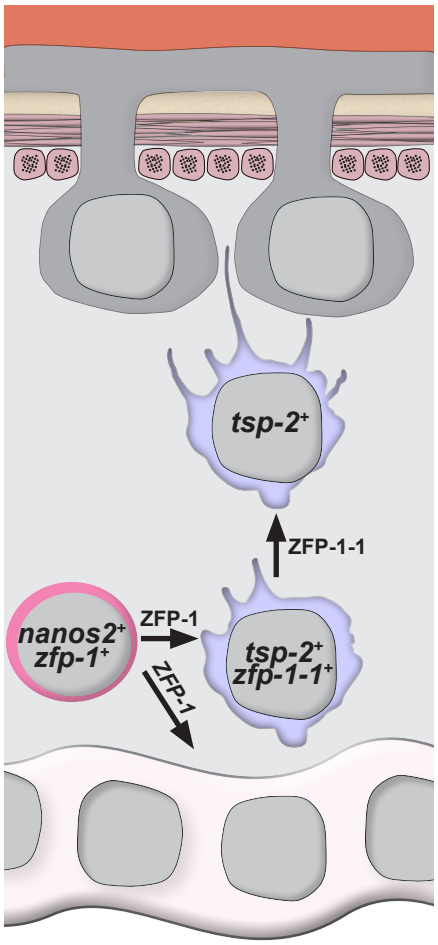

FIGURE 4.8: Model for the specification of new tegumental cells from neoblasts

Neoblasts (magenta cells) expressing *nanos2* and *zfp-1* specify large numbers of *tsp-2*$^{+}$ cells. Some fraction of *tsp-2*$^{+}$ cells express *zfp-1-1*. Within this *tsp-2*$^{+}$ compartment are cells that extend cytoplasmic projections that ultimately fuse with the tegumental syncytium. Loss of *zfp-1* function results in a general differentiation defect (i.e. loss of both tegument progenitors and gut cells) whereas loss of *zfp-1-1* function results in a specific loss of *tsp-2*$^{+}$ cells responsible for replenishing the tegument. In both cases, depletion of *tsp-2*$^{+}$ cells causes a reduction in the total number of tegumental cell bodies.

Figure 5.1

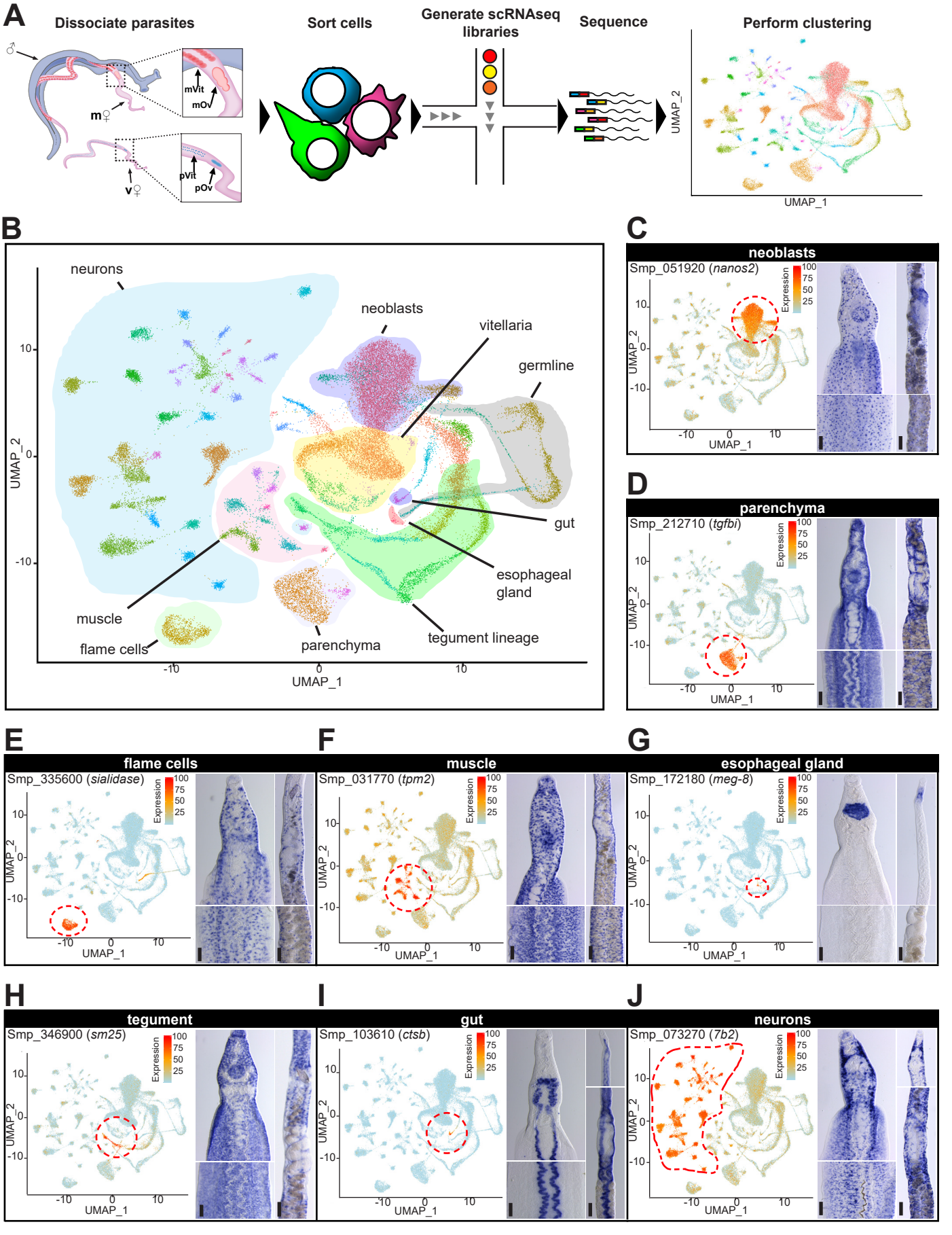
A
Dissociate parasites
Sort cells
Generate scRNAseq libraries
Sequence
Perform clustering
mVit
mOv
pVit
pOv
UMAP_1
UMAP_2
B
neurons
neoblasts
vitellaria
germline
gut
esophageal gland
muscle
flame cells
parenchyma
tegument lineage
C
neoblasts
Smp_051920 (nanos2)
D
parenchyma
Smp_212710 (tgfbi)
E
flame cells
Smp_335600 (sialidase)
F
muscle
Smp_031770 (tpm2)
G
esophageal gland
Smp_172180 (meg-8)
H
tegument
Smp_346900 (sm25)
I
gut
Smp_103610 (ctsb)
J
neurons
Smp_073270 (7b2)
Expression

FIGURE 5.1: Overview of the single-cell RNAseq atlas of adult *Schistosoma mansoni*

(A) Schematic diagram of single-cell RNA sequencing workflow. Cartoon to left depicts male paired with a mature female worm (m♀) that possess a mature ovary (mOv) and vitellaria (mVit); unpaired virgin female worms (v♀) possess a primordial ovary (pOv) and vitellaria (pVit). (B) Uniform Manifold Approximation and Projection (UMAP) plot of the 68 scRNAseq clusters. (C-J), (left) UMAP plot and whole-mount *in situ* hybridization (WISH) of the indicated gene and its expression in the noted tissue in the head (middle, top) and body (middle, bottom) of a male and the ovary (right, top) and vitellaria (right, bottom) of a mature female parasite. Scale bars, 100μm. UMAP plots colored by gene expression (blue = low, red = high).

Figure 5.2

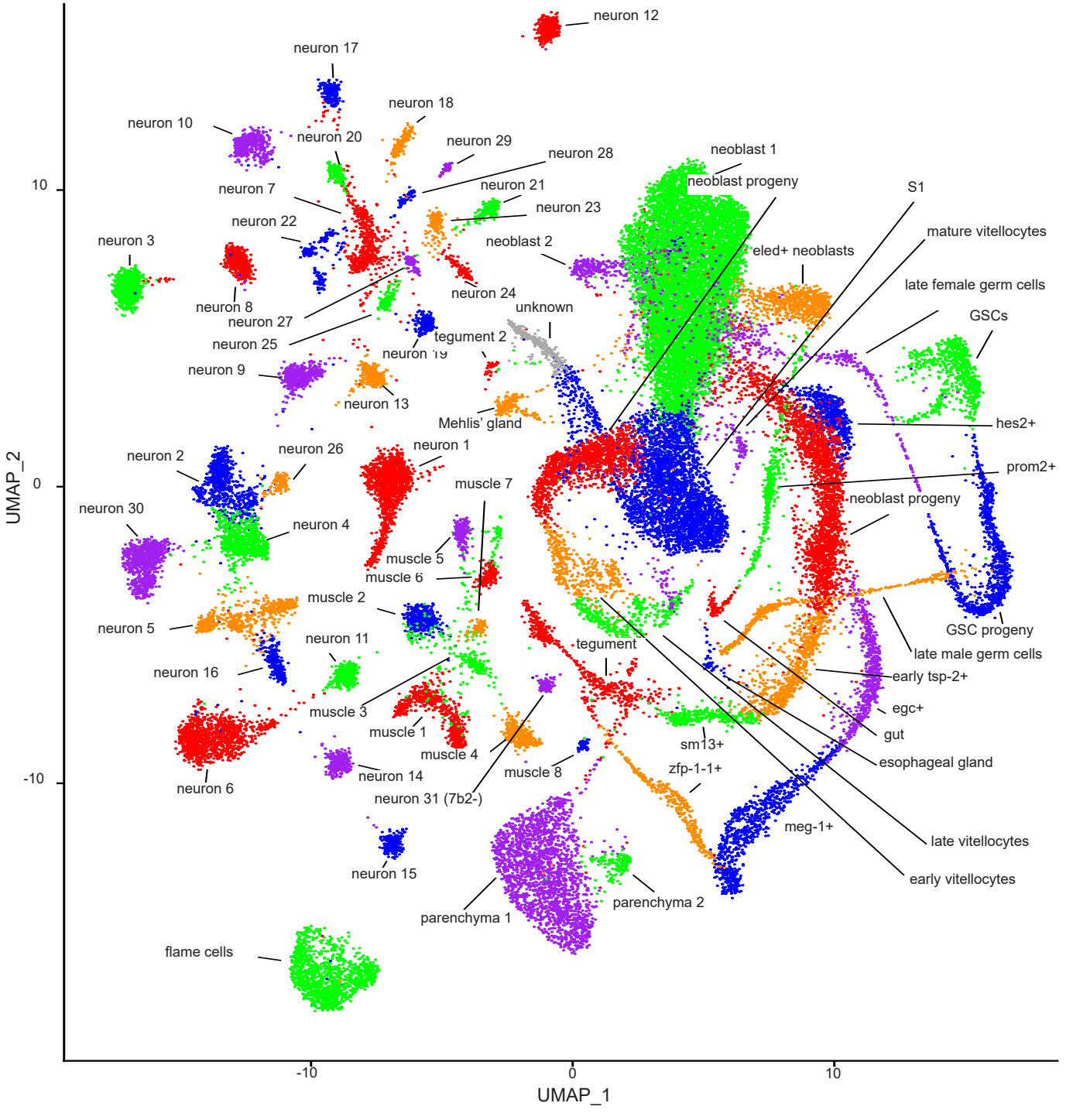
neuron 12
neuron 17
neuron 18
neuron 10
neuron 20
neuron 29
neuron 28
neuron 7
neuron 21
neuron 23
neuron 22
neuron 3
neuron 8
neuron 24
neuron 27
neuron 25
neuron 19
tegument 2
unknown
neuron 9
neuron 13
Mehlis' gland
neuron 2
neuron 26
neuron 1
muscle 7
neuron 30
neuron 4
muscle 5
muscle 6
muscle 2
neuron 5
neuron 11
neuron 16
muscle 3
muscle 1
muscle 4
muscle 8
neuron 14
neuron 6
neuron 31 (7b2-)
neuron 15
parenchyma 1
flame cells
neoblast 1
neoblast progeny
neoblast 2
eled+ neoblasts
S1
mature vitellocytes
late female germ cells
GSCs
hes2+
prom2+
neoblast progeny
GSC progeny
late male germ cells
early tsp-2+
egc+
gut
esophageal gland
tegument
sm13+
zfp-1-1+
meg-1+
late vitellocytes
early vitellocytes
parenchyma 2
10
0
-10
UMAP_2
-10
0
10
UMAP_1

FIGURE 5.2: Full view of the single-cell RNAseq atlas of adult *Schistosoma mansoni*.

Uniform Manifold Approximation and Projection (UMAP) plot of all clusters with labels.

Figure 5.3

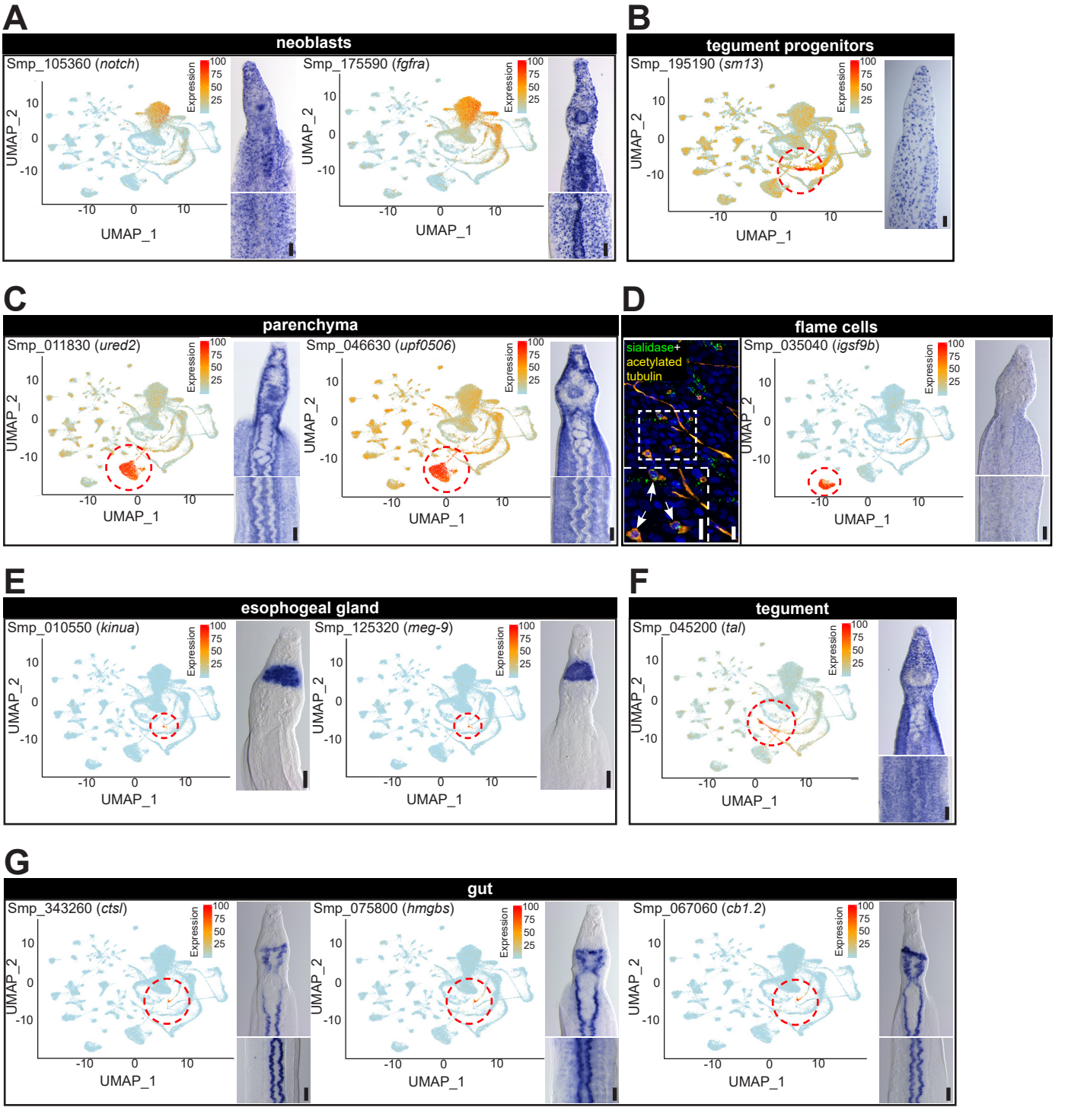
A
neoblasts
Smp_105360 (notch)
Smp_175590 (fgfra)
B
tegument progenitors
Smp_195190 (sm13)
C
parenchyma
Smp_011830 (ured2)
Smp_046630 (upf0506)
D
flame cells
sialidase+
acetylated
tubulin
Smp_035040 (igsf9b)
E
esophogeal gland
Smp_010550 (kinua)
Smp_125320 (meg-9)
F
tegument
Smp_045200 (tal)
G
gut
Smp_343260 (ctsl)
Smp_075800 (hmgbs)
Smp_067060 (cb1.2)
UMAP_1
UMAP_2
Expression

FIGURE 5.3: Additional somatic tissue-specific genes.

(A) (left) UMAP plot and (right) whole-mount *in situ* hybridization (WISH) of neoblast-specific genes *notch* and *fgfra*. (B) (left) UMAP plot and (right) WISH of tegument progenitor-specific gene *sm13*. (C) (left) UMAP plot and (right) WISH of parenchyma-specific genes *ured2* and *upf0506*. (D) (left) fluorescence *in situ* hybridization (FISH) with acetylated tubulin immunofluorescence to label cilia, (middle) UMAP plot, and (right) WISH of flame cell-specific gene *igsf9b*. (E) (left) UMAP plot and (right) WISH of esophageal gland-specific genes *kinua* and *meg-9*. (F) (left) UMAP plot and (right) WISH of tegument-specific gene *tal*. (G) (left) UMAP plot and (right) WISH of gut-specific genes *ctsl*, *hmgbs*, and *cb1.2*. Scale bars, D, left panel: 10 μm; all others: 100 μm. UMAP plots are colored by gene expression (blue = low, red = high).

Figure 5.4

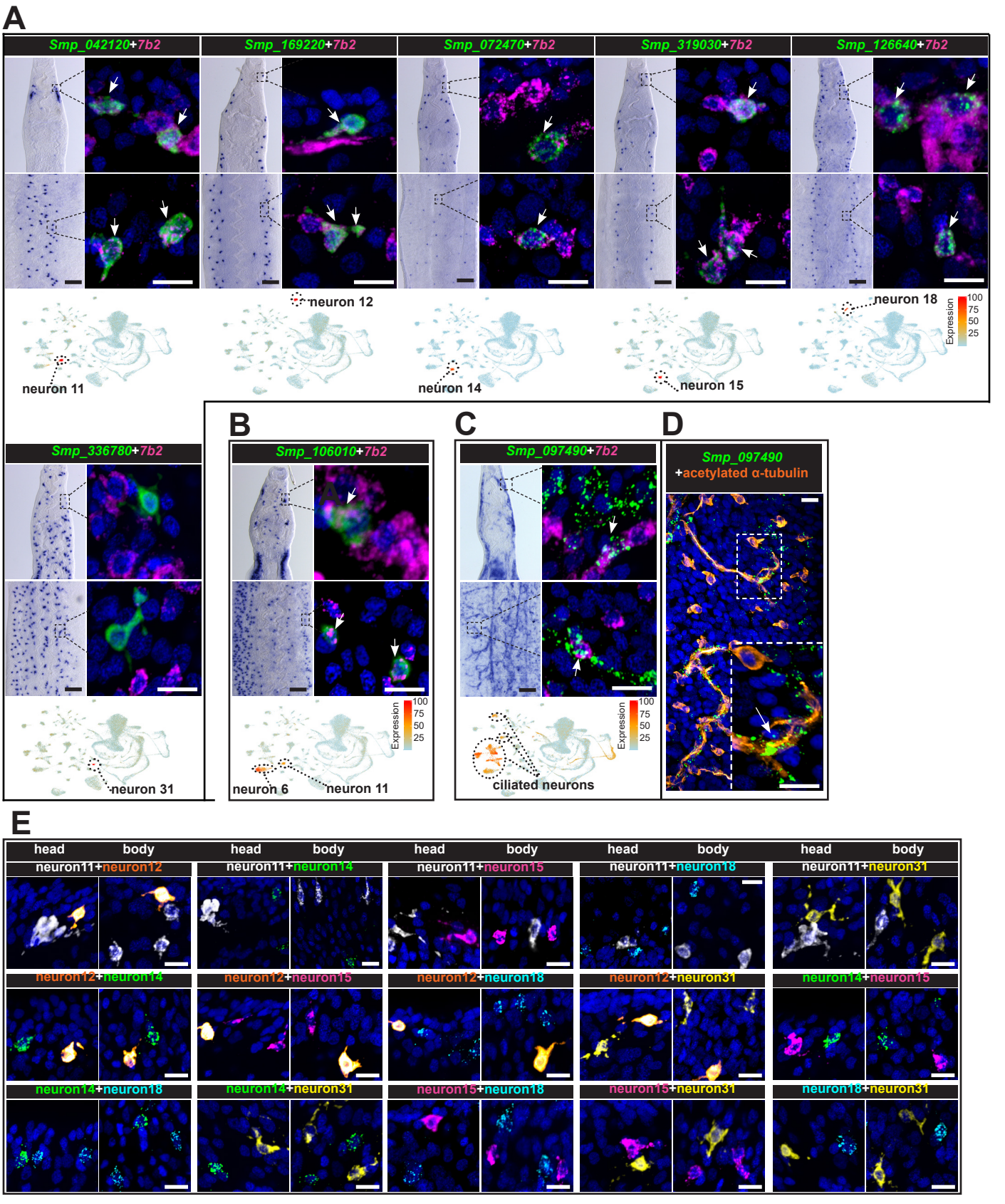
A
Smp_042120+7b2
Smp_169220+7b2
Smp_072470+7b2
Smp_319030+7b2
Smp_126640+7b2
neuron 11
neuron 12
neuron 14
neuron 15
neuron 18
Expression
100
75
50
25
Smp_336780+7b2
neuron 31
B
Smp_106010+7b2
neuron 6
neuron 11
C
Smp_097490+7b2
ciliated neurons
D
Smp_097490
+acetylated α-tubulin
E
head
body
neuron11+neuron12
neuron11+neuron14
neuron11+neuron15
neuron11+neuron18
neuron11+neuron31
neuron12+neuron14
neuron12+neuron15
neuron12+neuron18
neuron12+neuron31
neuron14+neuron15
neuron14+neuron18
neuron14+neuron31
neuron15+neuron18
neuron15+neuron31
neuron18+neuron31

FIGURE 5.4: Schistosome neurons display complex heterogeneity.

(A) For each of 6 different neuron cluster-specific genes (top left) WISH of head, (top right) double FISH of region of head indicated to the left with cluster specific gene (green) and *7b2* (magenta), (middle left) WISH of body, (middle right) double FISH of region of body indicated to the left with cluster specific gene (green) and *7b2* (magenta), and (bottom) UMAP plot. (B and C) (top left) WISH of head, (top right) double FISH of region of head indicated to the left with (B) “neuron 6”- and “neuron 11”- enriched gene *Smp_106010* (green) or (C) the ciliated neuron-enriched gene *Smp_097490* (green) and *7b2* (magenta), (middle left) WISH of body, (middle right) double FISH of region of body indicated to the left with *Smp_106010* (green) and *7b2* (magenta), and (bottom) UMAP plot. (D) FISH of *Smp_097490* (green) with immunofluorescent labeling of acetylated tubulin (orange) and (bottom) UMAP plot. (E) Double FISH with the indicated combination of neuron cluster-specific markers. Nuclei: blue. Scale bars, all FISH: 10 μm; all colorimetric WISH: 100 μm. UMAP plots are colored by gene expression (blue = low, red = high).

Figure 5.5

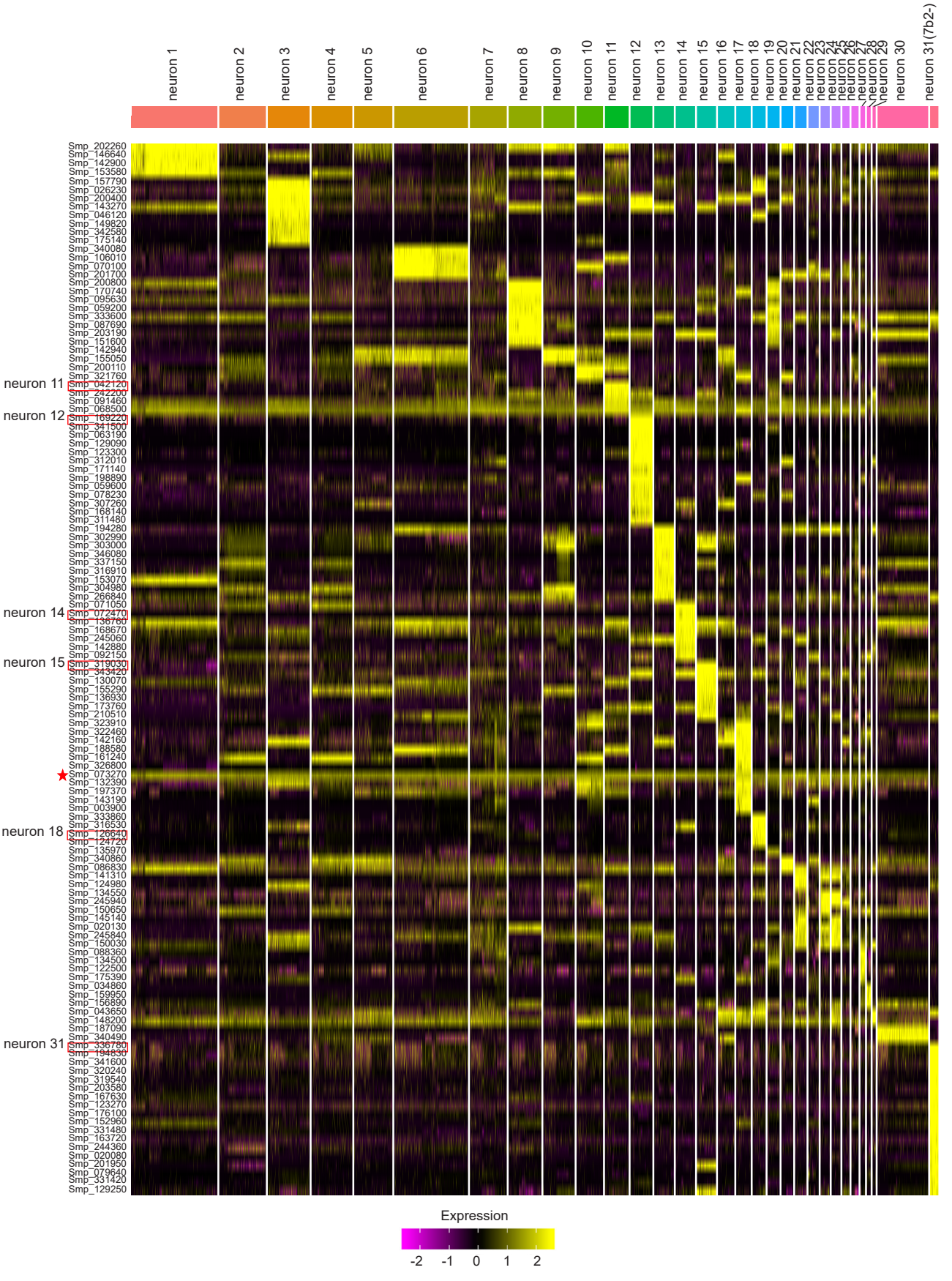
neuron 1
neuron 2
neuron 3
neuron 4
neuron 5
neuron 6
neuron 7
neuron 8
neuron 9
neuron 10
neuron 11
neuron 12
neuron 13
neuron 14
neuron 15
neuron 16
neuron 17
neuron 18
neuron 19
neuron 20
neuron 21
neuron 22
neuron 23
neuron 24
neuron 25
neuron 26
neuron 27
neuron 28
neuron 29
neuron 30
neuron 31(7b2-)
neuron 11
neuron 12
neuron 14
neuron 15
neuron 18
neuron 31
Expression
-2
-1
0
1
2

FIGURE 5.5: Heatmap of neuronal marker genes.

The six different neuron cluster-specific genes shown in Fig. S3A are labeled and indicated by a red rectangle. The general neuronal marker (for 30/31 clusters) *7b2* (Smp_073270) is indicated with red asterisk. Each row represents a gene and each column represents a cell. Clusters are indicated on the top of the panel. Heatmaps are colored by gene expression (purple = low, yellow = high).

Figure 5.6

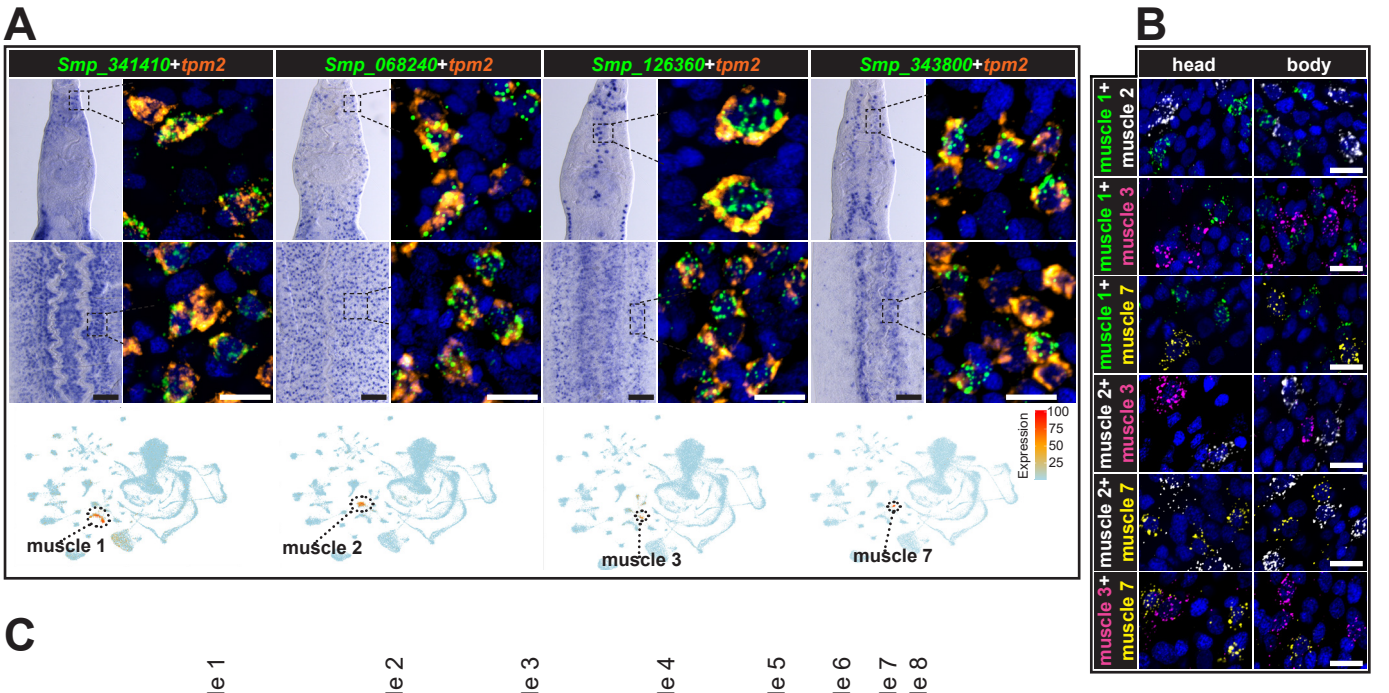
A
Smp_341410+tpm2
Smp_068240+tpm2
Smp_126360+tpm2
Smp_343800+tpm2
Expression
100
75
50
25
muscle 1
muscle 2
muscle 3
muscle 7
B
head
body
muscle 1+ muscle 2
muscle 1+ muscle 3
muscle 1+ muscle 7
muscle 2+ muscle 3
muscle 2+ muscle 7
muscle 3+ muscle 7

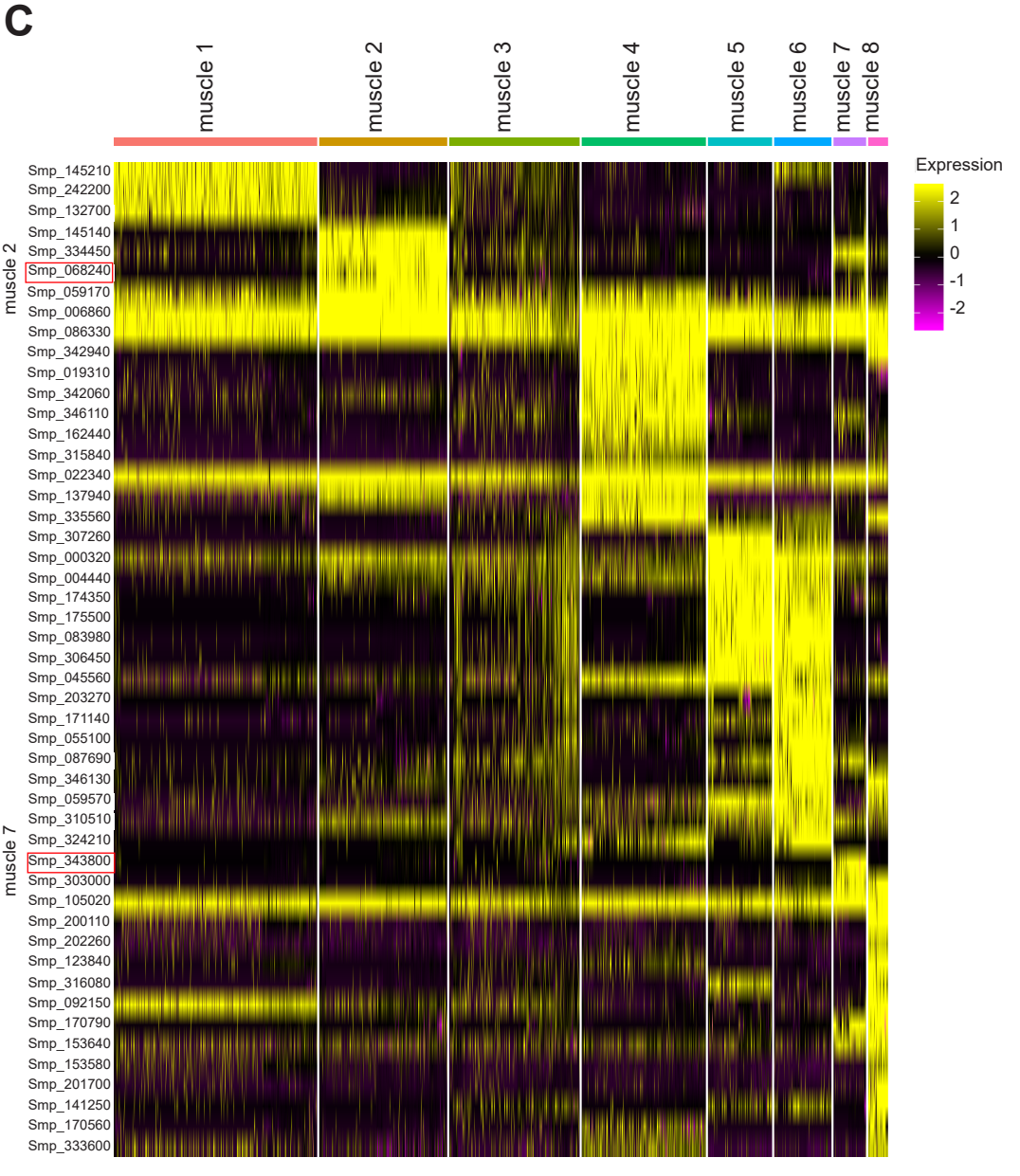
C
muscle 1
muscle 2
muscle 3
muscle 4
muscle 5
muscle 6
muscle 7
muscle 8
Expression
2
1
0
-1
-2
muscle 2
muscle 7
Smp_145210
Smp_242200
Smp_132700
Smp_145140
Smp_334450
Smp_068240
Smp_059170
Smp_006860
Smp_086330
Smp_342940
Smp_019310
Smp_342060
Smp_346110
Smp_162440
Smp_315840
Smp_022340
Smp_137940
Smp_335560
Smp_307260
Smp_000320
Smp_004440
Smp_174350
Smp_175500
Smp_083980
Smp_306450
Smp_045560
Smp_203270
Smp_171140
Smp_055100
Smp_087690
Smp_346130
Smp_059570
Smp_310510
Smp_324210
Smp_343800
Smp_303000
Smp_105020
Smp_200110
Smp_202260
Smp_123840
Smp_316080
Smp_092150
Smp_170790
Smp_153640
Smp_153580
Smp_201700
Smp_141250
Smp_170560
Smp_333600

FIGURE 5.6: Schistosome muscles display complex heterogeneity.

(A) For each of 4 different muscle cluster-specific genes: (top left) WISH of head, (top right) double FISH of region of head indicated to the left with cluster specific gene (green) and the general muscle marker *tropomyosin2* (*tpm2*, orange), (middle left) WISH of body, (middle right) double FISH of region of body indicated to the left with cluster-specific gene (green) and tpm2 (orange), and (bottom) UMAP plot. (B) Double FISH with the indicated combination of muscle cluster-specific markers. (C) Heatmap of the expression of the most uniquely expressed genes from the 8 muscle clusters grouped by cluster number. The “muscle 2” and “muscle 7” cluster-specific genes shown in (A) are labeled and indicated by a red rectangle. Each row represents a gene and each column represents a cell. Clusters are indicated on the top of the panel. Nuclei: blue. Scale bars, all FISH: 10 μm, all colorimetric WISH: 100 μm. UMAP plots are colored by gene expression (blue = low, red = high). Heatmaps are colored by gene expression (purple = low, yellow = high).

Figure 5.7

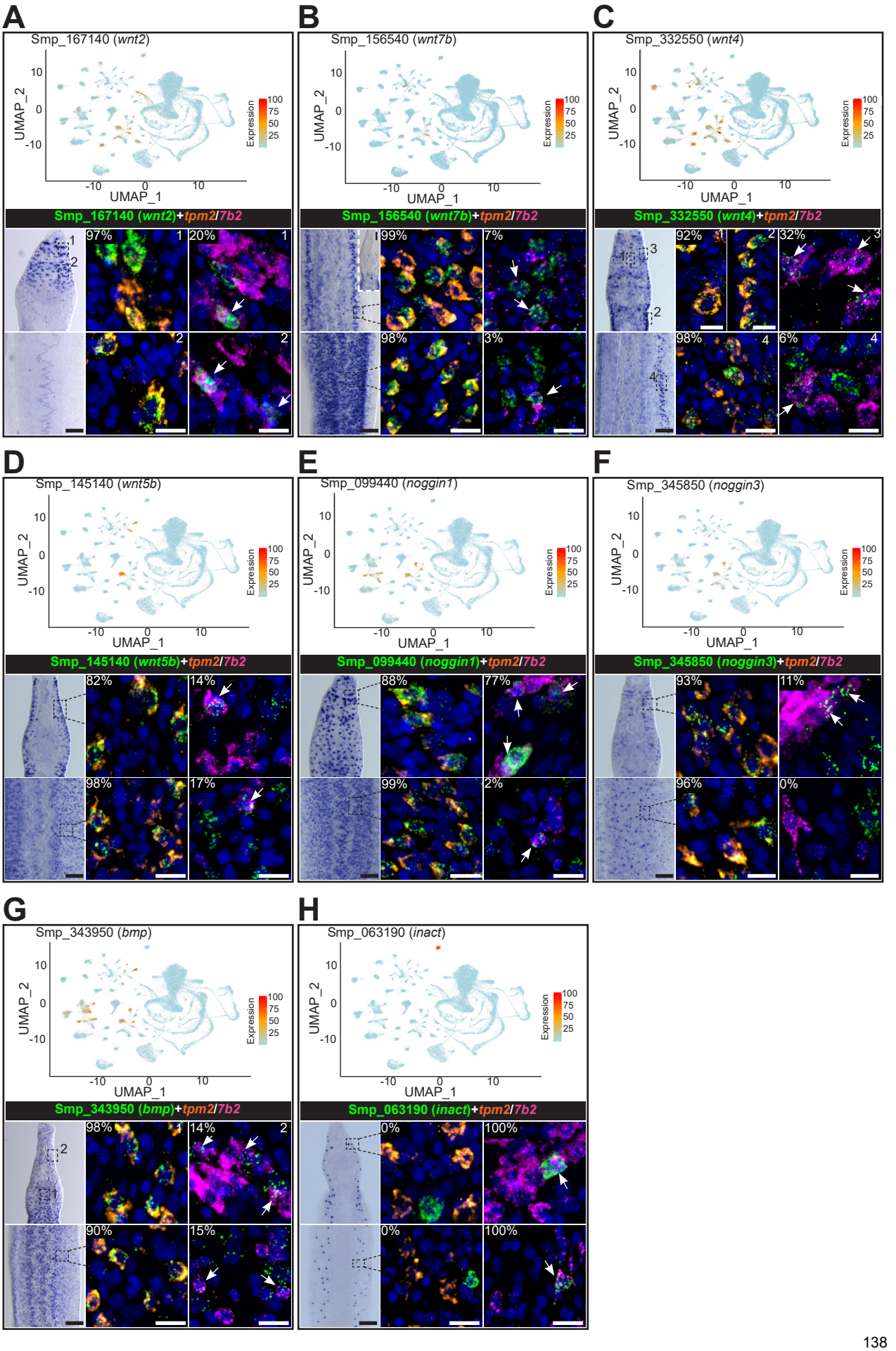
A
Smp_167140 (wnt2)
Smp_167140 (wnt2)+tpm2/7b2
B
Smp_156540 (wnt7b)
Smp_156540 (wnt7b)+tpm2/7b2
C
Smp_332550 (wnt4)
Smp_332550 (wnt4)+tpm2/7b2
D
Smp_145140 (wnt5b)
Smp_145140 (wnt5b)+tpm2/7b2
E
Smp_099440 (noggin1)
Smp_099440 (noggin1)+tpm2/7b2
F
Smp_345850 (noggin3)
Smp_345850 (noggin3)+tpm2/7b2
G
Smp_343950 (bmp)
Smp_343950 (bmp)+tpm2/7b2
H
Smp_063190 (inact)
Smp_063190 (inact)+tpm2/7b2
UMAP_1
UMAP_2
Expression

FIGURE 5.7: Morphogen homologs are expressed in schistosome muscles and neurons.

(A-H) (top) UMAP plots, (middle left) WISH of head, (middle middle) double FISH of region indicated to the left with muscle-specific gene *tpm2*, (middle right) or the neuron-specific gene *7b2*, (bottom left) WISH of body, (bottom middle) double FISH of region indicated to the left with muscle-specific gene *tpm2*, (bottom right) or the neuron-specific gene *7b2* for (A-D) wnt pathway genes or (E-H) tgfβ pathway genes. Percentage in upper left corner of micrographs indicates percent of co-expression of the indicated gene with either *tpm2* or *7b2*. All cells were counted from three different animals. Nuclei: blue. Scale bars, all FISH: 10 μm. all WISH: 100 μm. UMAP plots are colored by gene expression (blue = low, red = high).

Figure 5.8

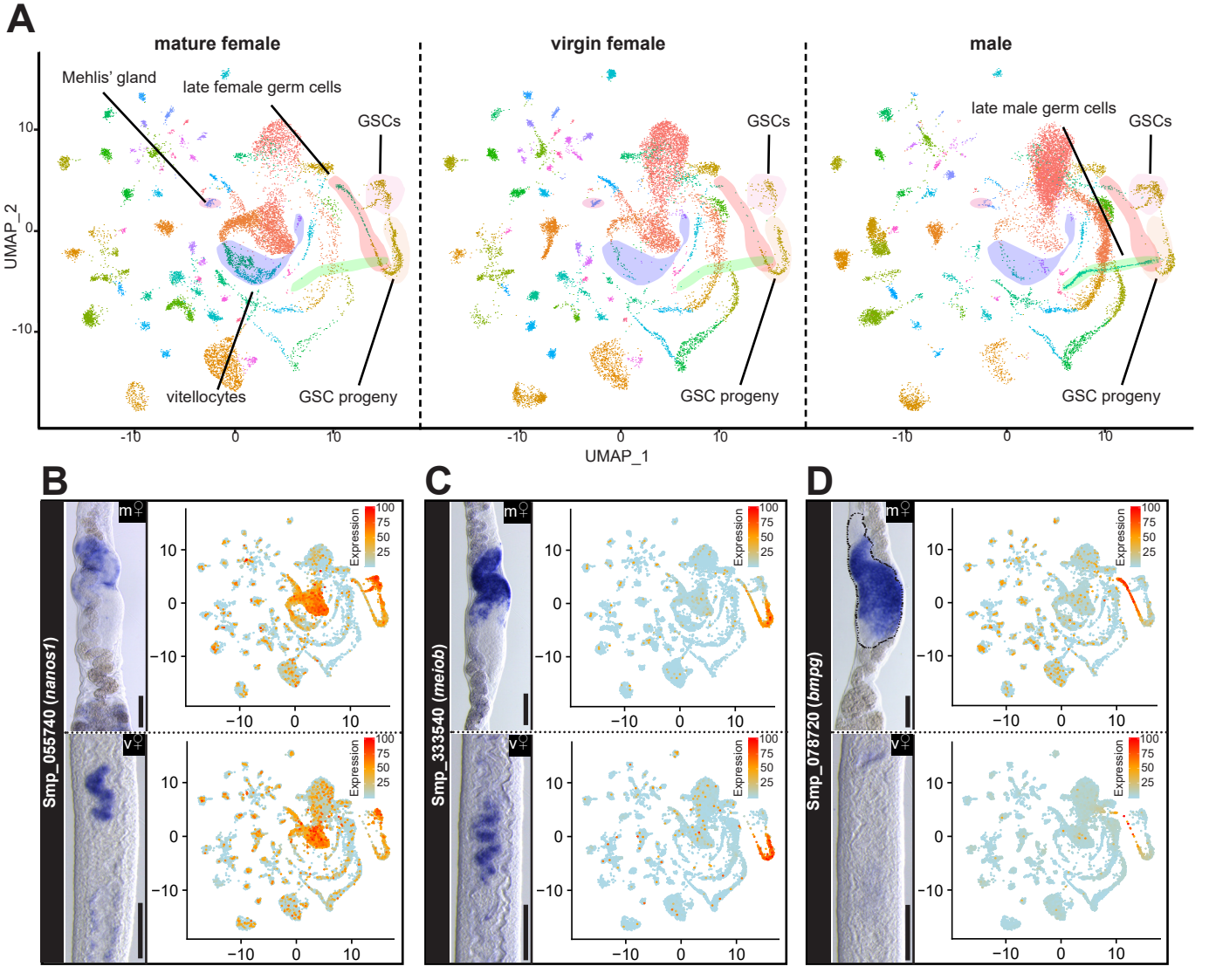
A
mature female
virgin female
male
Mehlis' gland
late female germ cells
late male germ cells
GSCs
vitellocytes
GSC progeny
UMAP_1
UMAP_2
B
C
D
Smp_055740 (nanos1)
Smp_333540 (meiob)
Smp_078720 (bmpg)
m♀
v♀
Expression
100
75
50
25

FIGURE 5.8: The germ lineage in schistosome ovaries.

(A) UMAP plots of all clusters split by parasite sex. Sexual tissues are labeled. (B-D) (top) WISH and UMAP plot of gene expression of indicated gene in sexually mature females (m♀) (top) and in virgin females (v♀) (bottom) for the “GSCs” marker *nanos1* (B), the “GSC progeny” marker *meiob* (C), and the “late female germ cells” marker *bmpg* (D). Dashed line indicates boundary of ovary. Scale bars, 100μm. UMAP plots are colored by gene expression (blue = low, red = high).

Figure 5.9

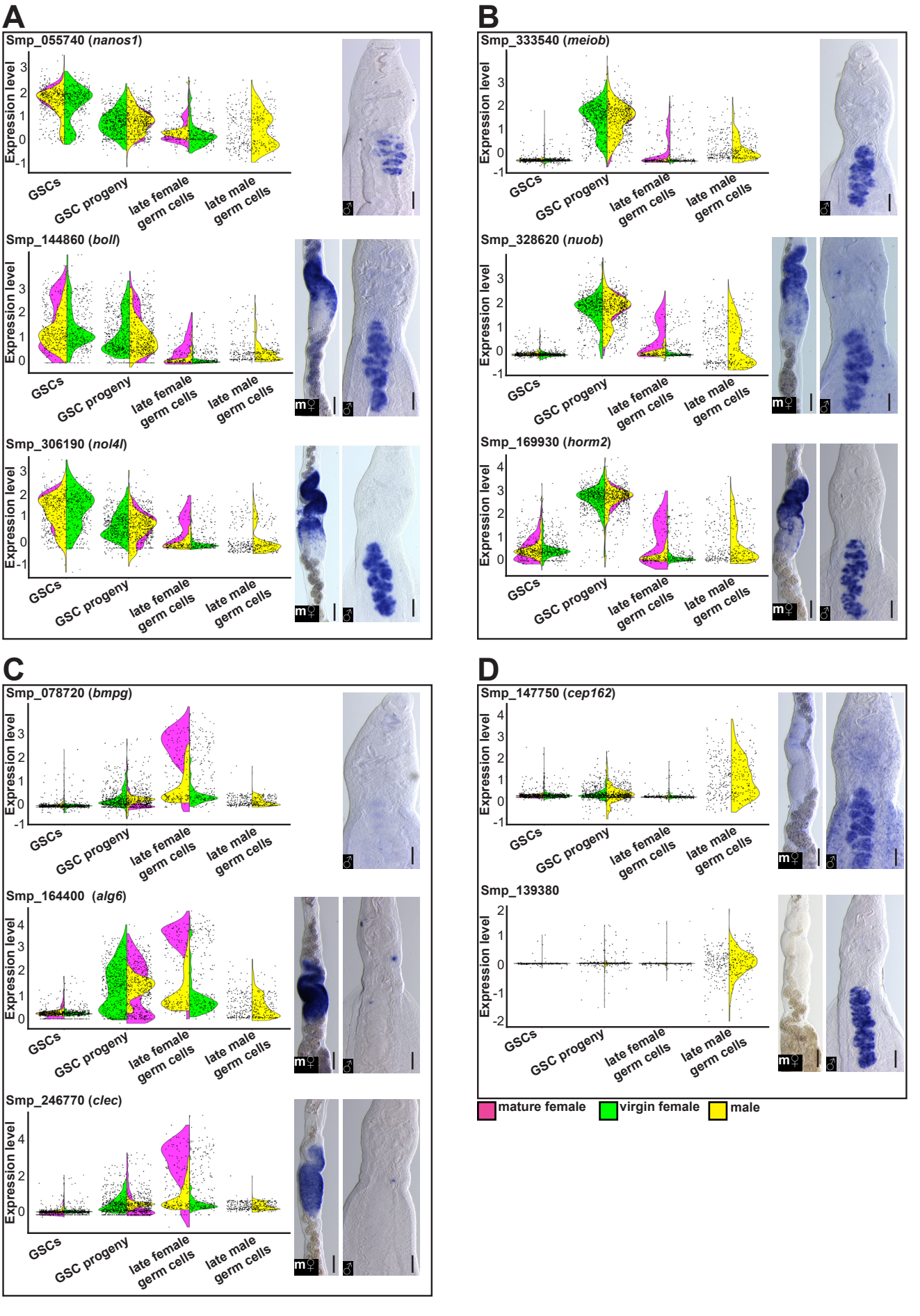
A
Smp_055740 (nanos1)
Smp_144860 (boll)
Smp_306190 (nol4l)
B
Smp_333540 (meiob)
Smp_328620 (nuob)
Smp_169930 (horm2)
C
Smp_078720 (bmpg)
Smp_164400 (alg6)
Smp_246770 (clec)
D
Smp_147750 (cep162)
Smp_139380
Expression level
GSCs
GSC progeny
late female germ cells
late male germ cells
mature female
virgin female
male

FIGURE 5.9: Additional germline tissue-specific genes.

(A-D) For the (A) “GSCs”-enriched genes nanos1, boll, and nol4l, (B) “GSC progeny”-enriched genes *meiob*, *nuob*, and *horm2*, (C) “late female germ cells”-enriched genes *bmpg*, *alg6*, and *clec*, and (D) “late male germ cells”-enriched genes *cep162* and *Smp_139380*: (left) violin plots showing gene expression levels across the indicated clusters colored by sex (mature female = magenta, virgin female = green, male = yellow) and (middle and right) WISH of the indicated gene in the (middle) ovary of sexually mature females (m♀) and (right) testes of males (♂). Scale bars, all 100 μm.

Figure 5.10

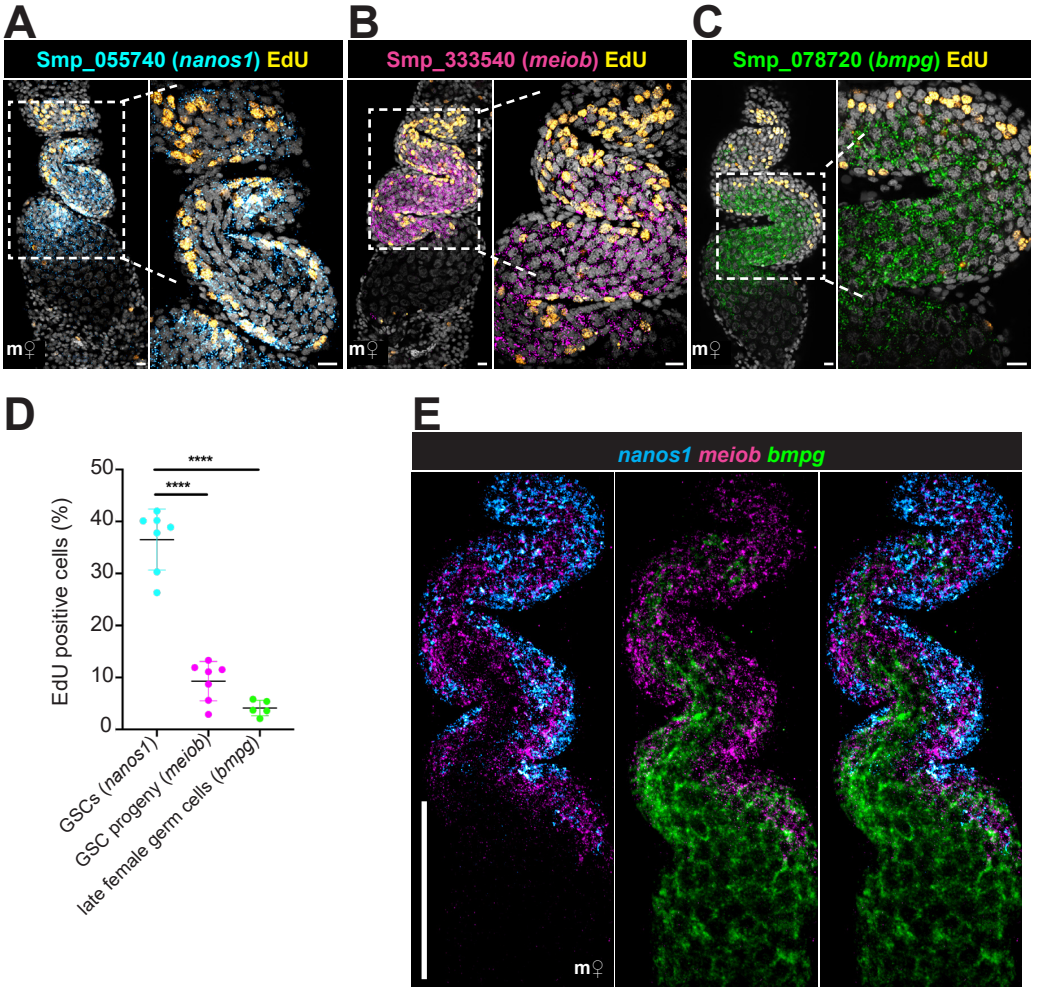
A
Smp_055740 (nanos1) EdU
B
Smp_333540 (meiob) EdU
C
Smp_078720 (bmpg) EdU
m♀
D
EdU positive cells (%)
50
40
30
20
10
0
****
****
GSCs (nanos1)
GSC progeny (meiob)
late female germ cells (bmpg)
E
nanos1 meiob bmpg
m♀

FIGURE 5.10: Description of germ lineage in schistosome ovary.

(A-C) FISH of the GSC marker *nanos1* (cyan) (A), the “GSC progeny”-enriched gene *meiob* (magenta) (B), or the “late female germ cells”-enriched gene *bmpg* (green) (C) in conjunction with a 30-minute EdU pulse (orange) to label the actively proliferating cells of the ovary of a sexually mature female (m♀). Nuclei: grey. (D) Graph showing quantification of percentage of *nanos1*$^{+}$, *meiob*$^{+}$, or *bmpg*$^{+}$ cells that are EdU^{+} following a 30-minute EdU pulse. (E) Triple FISH of *nanos1*, *meiob* and *bmpg* in the ovary of a sexually mature female (m♀). Scale bars, all 100 μm. **** $p < 0.0001$ (one-way ANOVA test).

Figure 5.11

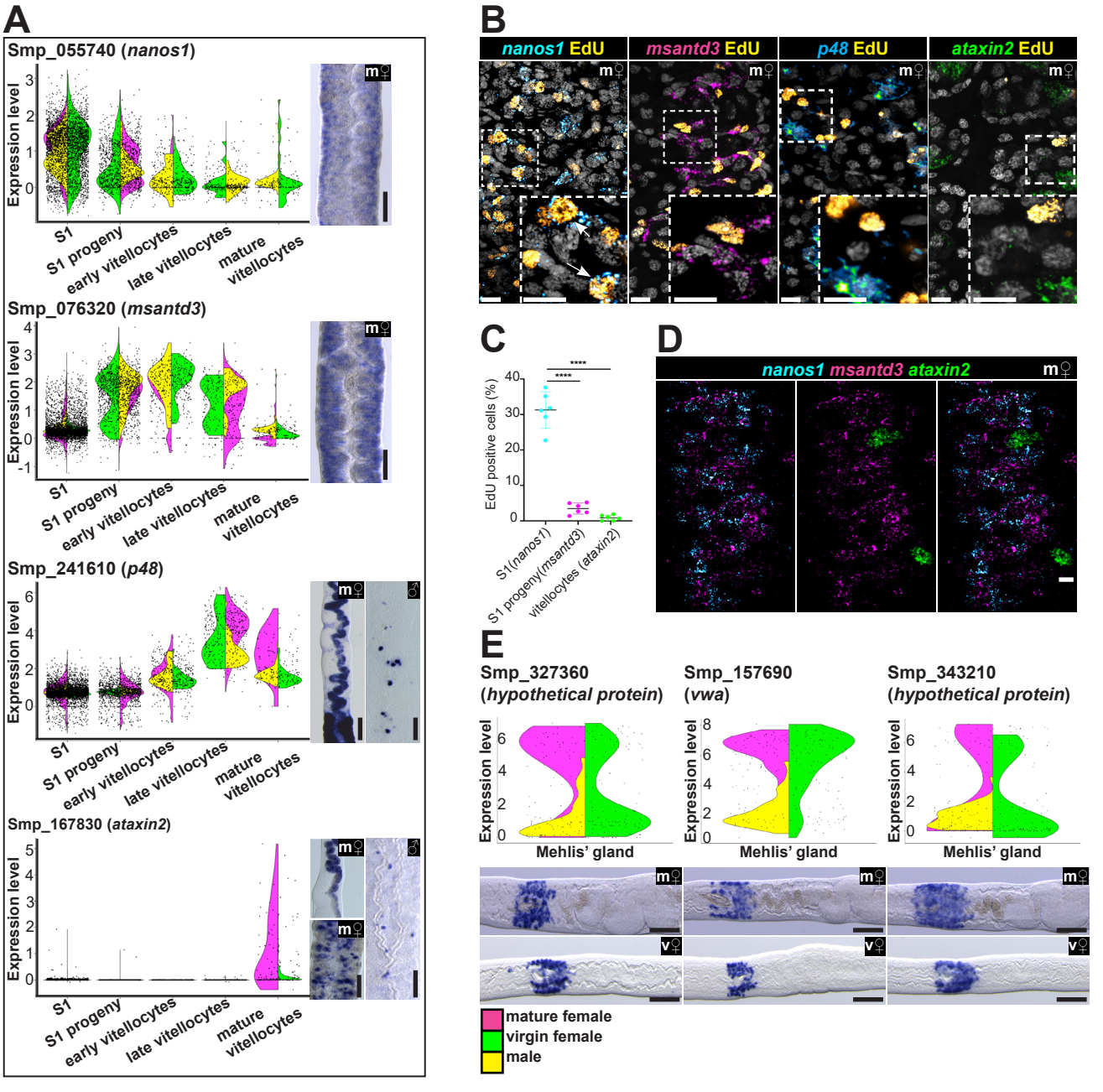
A
Smp_055740 (nanos1)
Smp_076320 (msantd3)
Smp_241610 (p48)
Smp_167830 (ataxin2)
Expression level
S1
S1 progeny
early vitellocytes
late vitellocytes
mature vitellocytes
B
nanos1 EdU
msantd3 EdU
p48 EdU
ataxin2 EdU
C
EdU positive cells (%)
S1 (nanos1)
S1 progeny (msantd3)
vitellocytes (ataxin2)
D
nanos1 msantd3 ataxin2
E
Smp_327360 (hypothetical protein)
Smp_157690 (vwa)
Smp_343210 (hypothetical protein)
Mehlis' gland
mature female
virgin female
male

FIGURE 5.11: Description of germ lineage in schistosome vitellaria.

(A-B) For the “S1” marker *nanos1*, the “S1 progeny” marker *msantd3*, the “late vitellocytes” marker *p48*, and the “mature vitellocytes” marker *ataxin2*: (A) (left) violin plots showing gene expression levels across the indicated clusters colored by sex (mature female = magenta, virgin female = green, male = yellow) and (right) WISH of the indicated gene in the vitellaria of mature females (m♀) and the midline of males (♂) as indicated on the image or (B) FISH for the indicated gene with EdU labeling of proliferative cells (orange) in the vitellaria of a sexually mature female. Nuclei: grey. (C) Graph showing quantification of percentage of *nanos1*$^{+}$, *msantd3*$^{+}$, or *ataxin2*$^{+}$ cells that are EdU+ following a 30-minute EdU pulse. (D) Representative micrograph of triple FISH of *nanos1*, *msantd3*, and *ataxin2* in the vitellaria of a sexually mature female. (E) For the “Mehlis’ gland” marker *Smp_327360*, *vwa*, and *Smp_343210*: (top) violin plots showing gene expression levels in the “Mehlis’ gland” cluster colored by sex (mature female = magenta, virgin female = green, male = yellow) and (bottom) WISH of the indicated gene in region anterior to the ovary in sexually mature females (m♀) and virgin females (v♀) as indicated on the image. Scale bars, A, E, 100 μm; B, D, 10 μm. **** $p < 0.0001$ (one-way ANOVA test).

Figure 5.12

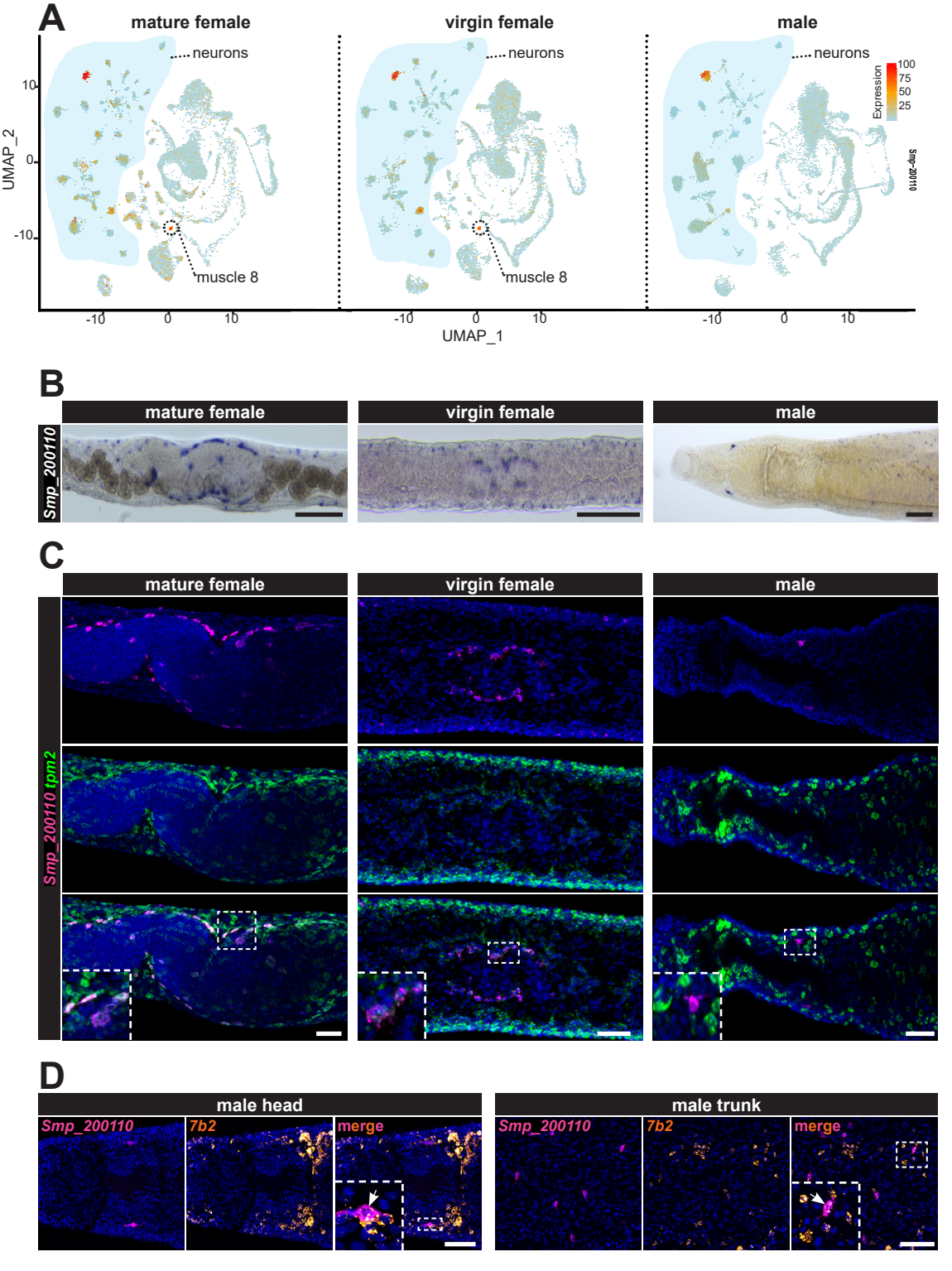
A
mature female
virgin female
male
neurons
muscle 8
UMAP_2
UMAP_1
Expression
Smp_200110
B
mature female
virgin female
male
Smp_200110
C
mature female
virgin female
male
Smp_200110 tpm2
D
male head
male trunk
Smp_200110
7b2
merge

FIGURE 5.12: Description of a female-specific muscle type.

(A) UMAP plot showing expression of the “muscle 8” marker *Smp_200110* in mature female (left), virgin female (middle) but not near male gonads (right). (B) WISH of *Smp_200110* in mature female (left), virgin female (middle) and male (right). (C) Double FISH of *Smp_200110* (magenta) and the general muscle marker *tpm2* (green). Left and middle insets highlight co-expression of *Smp_200110* and *tpm2* around the ovary in mature and virgin female parasites. Right inset highlights lack of co-expression of *Smp_200110* and *tpm2* in male parasites. (D) Double FISH of *Smp_200110* (magenta) and general neuronal marker *7b2* (orange) in the (left) head and (right) trunk of male parasites. Insets show co-expression of *Smp_200110* and *7b2* through the male. UMAP plots are colored by gene expression (blue = low, red = high). Scale bars, B, 100 μm; C, D, 50 μm.

Figure 5.13

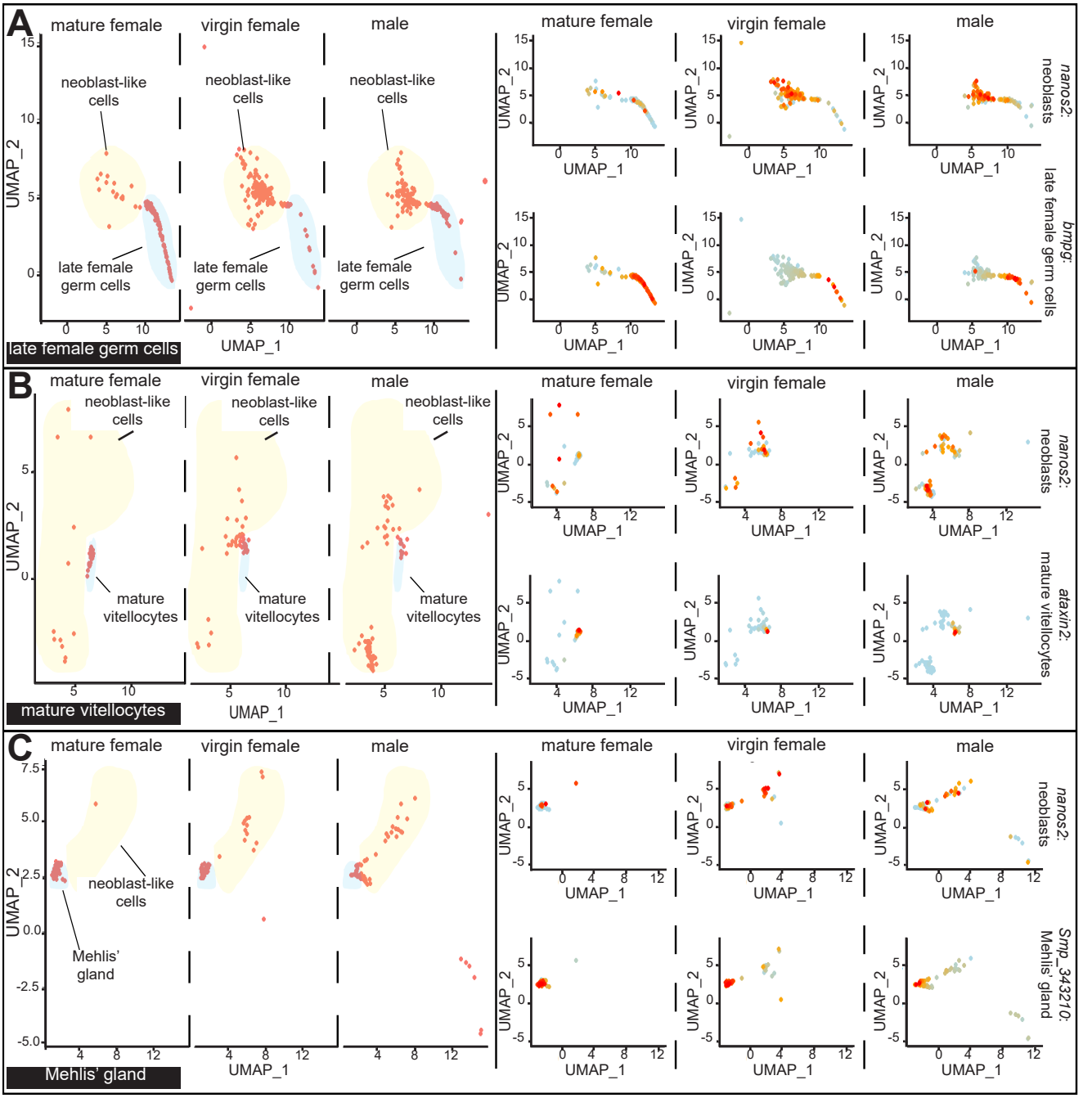
A
mature female
virgin female
male
neoblast-like cells
late female germ cells
late female germ cells
UMAP_1
UMAP_2
nanos2: neoblasts
bmpg: late female germ cells
B
mature vitellocytes
ataxin2: mature vitellocytes
C
Mehlis' gland
Smp_343210: Mehlis' gland

FIGURE 5.13: Male cells in female reproductive tissues.

(A-C) (Left) UMAP plot showing all cells in the indicated cluster split by parasite sex and maturity. (top right) UMAP plot showing the expression of the neoblast marker *nanos2* in the indicated cluster split by parasite sex and maturity and (bottom right) UMAP plot showing the expression of the cluster marker in the indicated cluster split by parasite sex and maturity for (A) “late female germ cells”, (B) “mature vitellocytes” and (C) “Mehlis’ gland”. UMAP plots are colored by gene expression (blue = low, red = high).

Figure 6.1

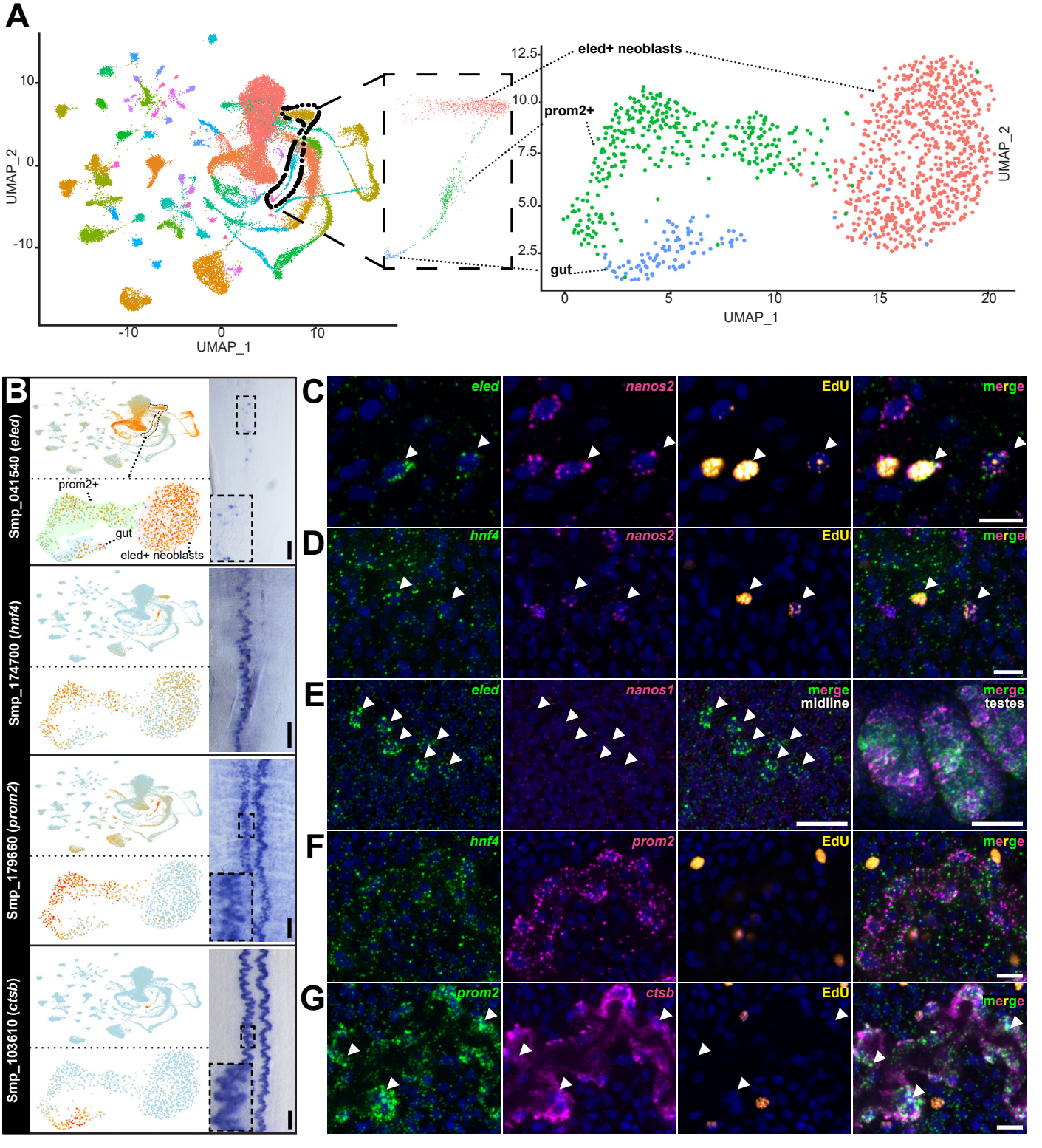
A
UMAP_2
UMAP_1
eled+ neoblasts
prom2+
gut
B
Smp_041540 (eled)
Smp_174700 (hnf4)
Smp_179660 (prom2)
Smp_103610 (ctsb)
C
D
E
F
G
eled
nanos2
hnf4
nanos1
prom2
ctsb
EdU
merge
merge midline
merge testes

FIGURE 6.1: A putative schistosome gut lineage.

(A) Schematic of the re-clustering of the putative gut lineage from the single cell RNAseq data. (B) UMAP plots of the expression pattern of the indicated gene on the (top) original dataset or the (bottom) re-clustered dataset, and (right) a colorimetric WISH of a male parasite's trunk for *eled*, *hnf4*, *prom2*, and *ctsb*. Insets: magnifications of dashed boxes. (C) Double FISH of *eled* and the neoblast marker *nanos2* in EdU^+ proliferative cells. Arrows indicate triple-positive cells. (D) Double FISH of *hnf4* and *nanos2* in EdU^+ proliferative cells. Arrows indicate triple-positive cells. (E) Double FISH of *eled* and the GSC marker *nanos1*. Arrows indicate single-positive *eled*$^+$ cells along the midline. (F) Double FISH of *hnf4* and *prom2*. (G) Double FISH of *prom2* with the gut marker *ctsb*. Arrows indicate foci of high *prom2* expression and low *ctsb* expression. Nuclei: blue. Scale bars, 10 μm.

Figure 6.2

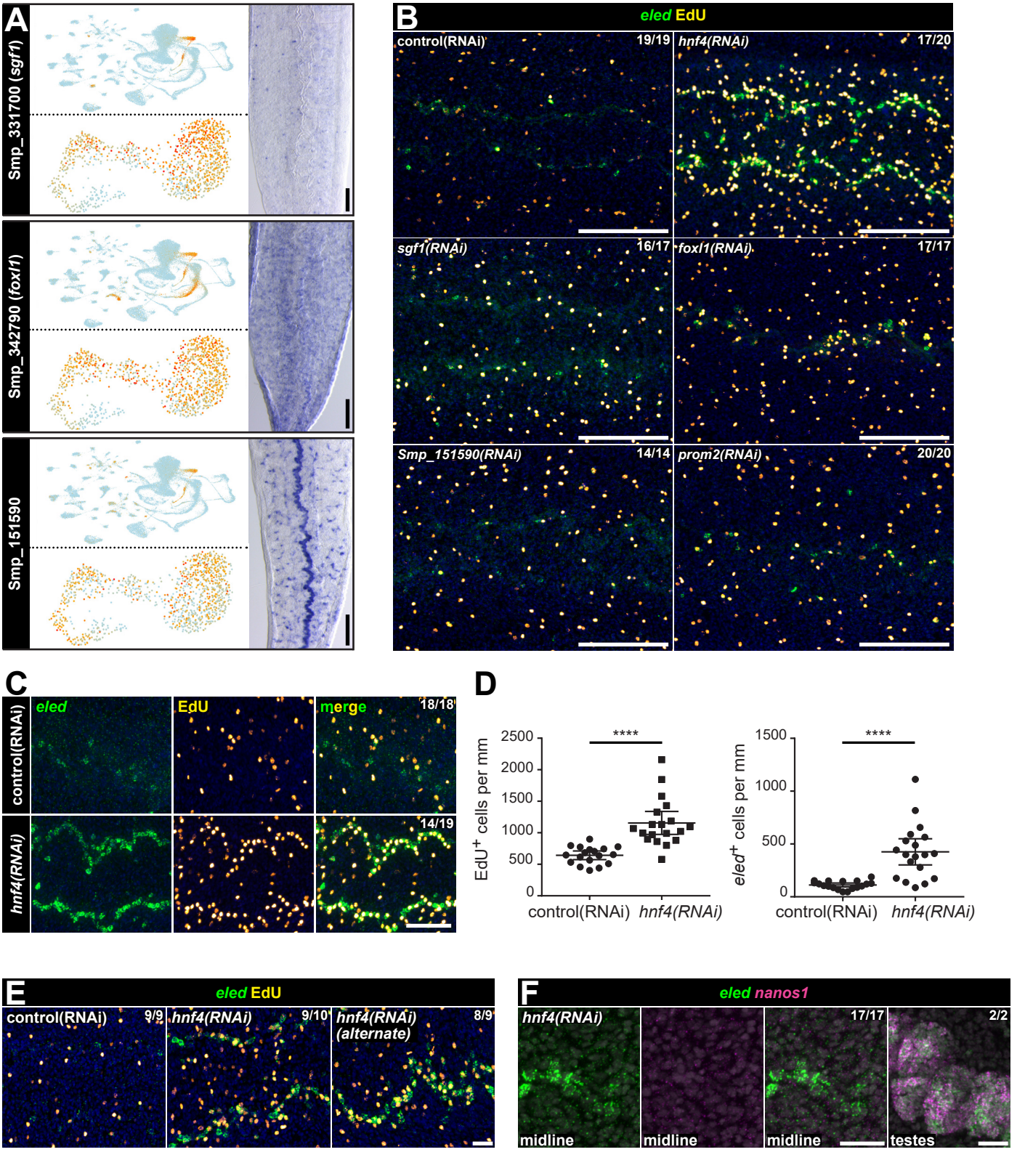
A
Smp_331700 (sgf1)
Smp_342790 (foxl1)
Smp_151590
B
eled EdU
control(RNAi) 19/19
hnf4(RNAi) 17/20
sgf1(RNAi) 16/17
foxl1(RNAi) 17/17
Smp_151590(RNAi) 14/14
prom2(RNAi) 20/20
C
control(RNAi)
hnf4(RNAi)
eled
EdU
merge
18/18
14/19
D
EdU+ cells per mm
2500
2000
1500
1000
500
0
****
control(RNAi)
hnf4(RNAi)
eled+ cells per mm
1500
1000
500
0
****
control(RNAi)
hnf4(RNAi)
E
eled EdU
control(RNAi) 9/9
hnf4(RNAi) 9/10
hnf4(RNAi) (alternate) 8/9
F
eled nanos1
hnf4(RNAi)
midline
midline
17/17
midline
2/2
testes

FIGURE 6.2: An RNAi screen identifies hnf4 as a regulator of eled+ neoblasts.

(A) For each of the "*eled*$^+$ neoblast"-enriched genes *sgf1*, *foxl1*, and *Smp_151590*: UMAP plots of the expression pattern of the indicated gene on the (top) original and (bottom) re-clustered dataset from Fig. S12A, and (right) WISH of the indicated gene. (B) FISH of *eled* with EdU pulse detection showing the location of *eled*$^+$ neoblasts (green) and EdU$^+$ proliferative cells (yellow) in the indicated RNAi condition. RNAi target gene name is indicated in the upper left. $n \geq 14$ parasites, two biological replicates. (C) FISH and EdU labeling showing the expression of *eled* (green) and EdU$^+$ proliferative cells (yellow) in control or *hnf4(RNAi)* animals. $n = \geq 18$ parasites, two biological replicates. (D) Graphs showing quantification of the number of EdU$^+$ proliferative cells or *eled*$^+$ cells per mm of parasite from (C) in either control(RNAi) or *hnf4(RNAi)* animals. (E) FISH of eled with EdU pulse detection showing the location of *eled*$^+$ neoblasts (green) and EdU$^+$ proliferative cells (yellow) in either control RNAi conditions ("control RNAi"), *hnf4* RNAi conditions ("*hnf4(RNAi)*"), or *hnf4* RNAi conditions using a separate, non-overlapping construct ("*hnf4(RNAi)* (alternate)"). $n \geq 9$ parasites, one biological replicate. (F) Double FISH of *eled* and *nanos1* demonstrating no co-expression along the parasite's midline but strong co-expression of *eled* and *nanos1* in reproductive organs like the testes in *hnf4* RNAi conditions. $n =$ 17 *hnf4(RNAi)* animals from two biological replicates. The number of parasites similar to the representative images is indicated in the upper-right of each panel. Nuclei: blue (B, C, E) or grey (F). Scale bars, A, B, 100 μm; E, F, 20 μm. UMAP plots are colored by gene expression (blue = low, red = high). **** $p < 0.0001$ (Welch's t-test).

Figure 6.3

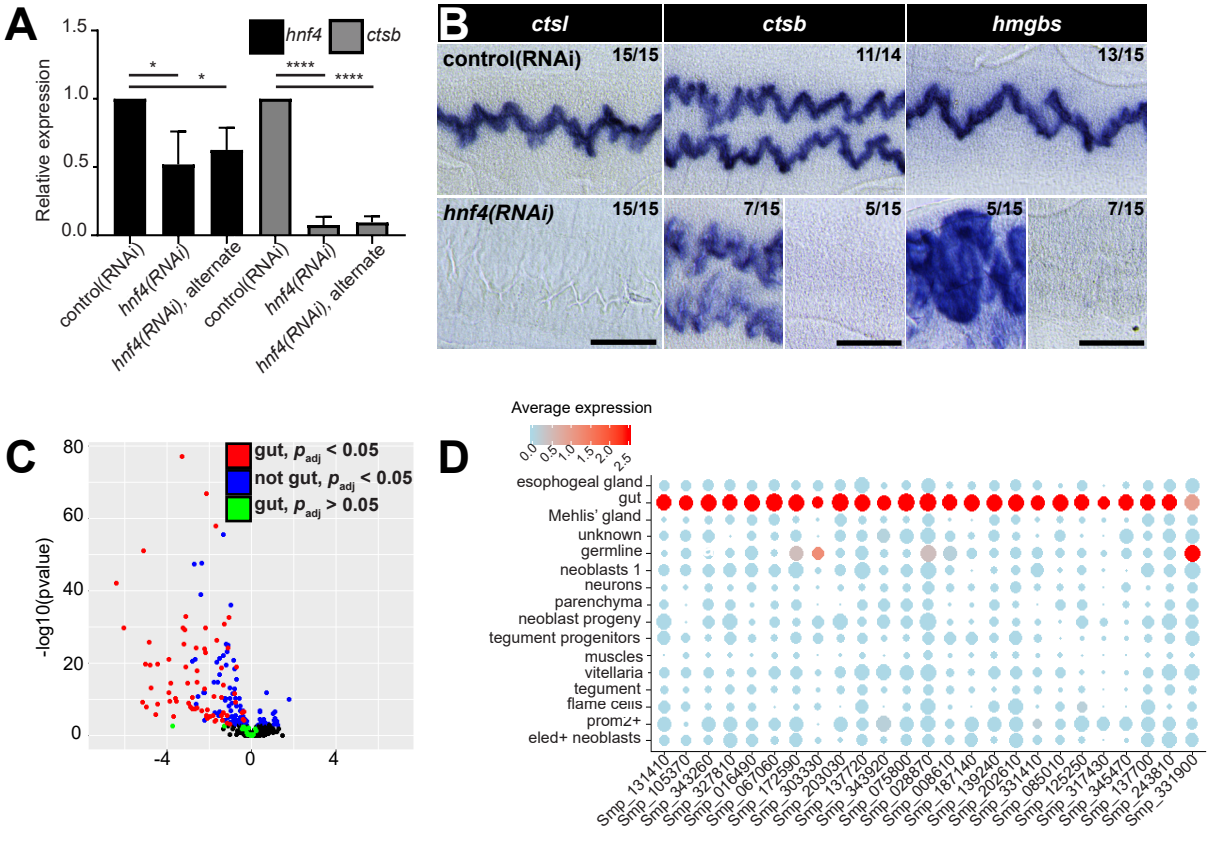
A
hnf4
ctsb
Relative expression
1.5
1.0
0.5
0.0
*
*
****
****
control(RNAi)
hnf4(RNAi)
hnf4(RNAi), alternate
control(RNAi)
hnf4(RNAi)
hnf4(RNAi), alternate
B
ctsl
ctsb
hmgbs
control(RNAi)
15/15
11/14
13/15
hnf4(RNAi)
15/15
7/15
5/15
5/15
7/15
C
gut, p_adj < 0.05
not gut, p_adj < 0.05
gut, p_adj > 0.05
-log10(pvalue)
80
60
40
20
0
-4
0
4
D
Average expression
0.0
0.5
1.0
1.5
2.0
2.5
esophogeal gland
gut
Mehlis' gland
unknown
germline
neoblasts 1
neurons
parenchyma
neoblast progeny
tegument progenitors
muscles
vitellaria
tegument
flame cells
prom2+
eled+ neoblasts
Smp_131410
Smp_105370
Smp_343260
Smp_327810
Smp_016490
Smp_067060
Smp_172590
Smp_303330
Smp_203030
Smp_137720
Smp_343920
Smp_075800
Smp_028870
Smp_008610
Smp_187140
Smp_139240
Smp_202610
Smp_331410
Smp_085010
Smp_125250
Smp_317430
Smp_345470
Smp_137700
Smp_243810
Smp_331900

FIGURE 6.3: hnf4 RNAi results in transcriptional gut abnormalities.

(A) Graph of relative quantification of *hnf4* mRNA (black) or *ctsb* mRNA (grey) as determined by qPCR in either "control(RNAi)", "*hnf4(RNAi)*", or "*hnf4(RNAi)* alternate" animals. Four biological replicates. (B) For the "gut"-specific genes *ctsl*, *ctsb* and *hmgbs*: WISH of the indicated gene in either control RNAi conditions or *hnf4* RNAi conditions. The number of parasites similar to representative images is indicated in the upper right of each panel. $n \geq 14$ parasites, three biological replicates. (C) Volcano plot of data from an RNAseq experiment comparing gene expression of control(RNAi) animals to that of *hnf4(RNAi)* animals. "gut", genes expressed in the "gut" cluster, "not gut", genes not expressed in the "gut" cluster. Significance determined as $p_{adj} < 0.05$ by Benjamini and Hochberg-corrected Wald test. (D) A dot-plot summarizing the cluster-specific expression of each of the top 25 down-regulated genes in *hnf4(RNAi)* animals. Cluster IDs are on the vertical axis and gene IDs are on the horizontal axis. Expression levels are colored by gene expression (blue = low, red = high). Percentage of cells in the cluster expressing the gene is indicated by the size of the circle (small = few, large = many). Scale bars, 100 μm. * $p < 0.05$, **** $p < 0.0001$ (Welch's t-test).

Figure 6.4

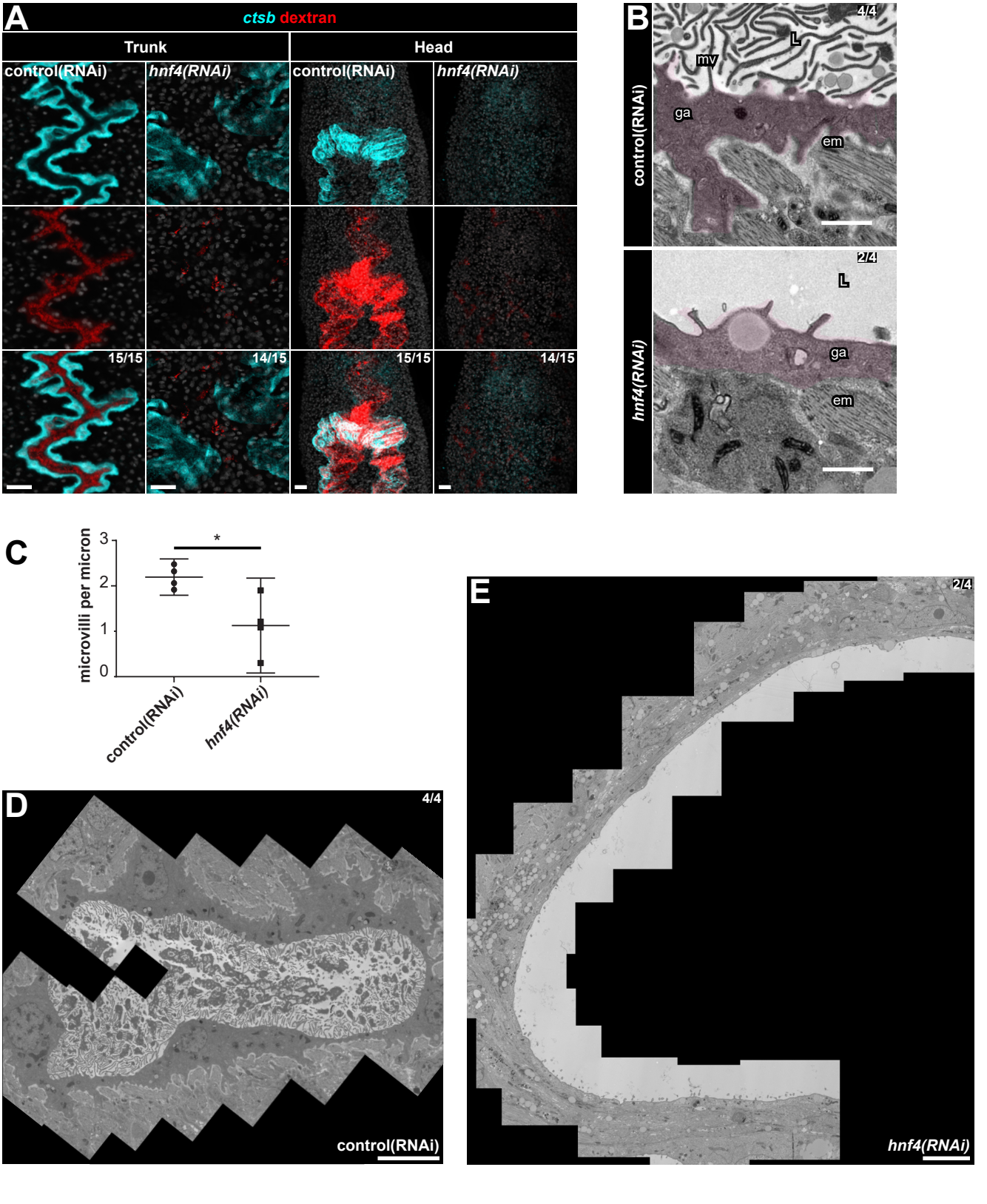
A
ctsb dextran
Trunk
Head
control(RNAi)
hnf4(RNAi)
control(RNAi)
hnf4(RNAi)
15/15
14/15
15/15
14/15
B
4/4
control(RNAi)
mv
L
ga
em
2/4
hnf4(RNAi)
L
ga
em
C
microvilli per micron
3
2
1
0
*
control(RNAi)
hnf4(RNAi)
D
4/4
control(RNAi)
E
2/4
hnf4(RNAi)

FIGURE 6.4: hnf4 RNAi results in structural gut abnormalities.

(A) FISH of the gut marker *ctsb* (cyan) and fluorescently-labeled dextran (red) in the gut lumen in the parasite's trunk (left two panels) or head (right two panels) in either control RNAi or *hnf4* RNAi conditions. *n* =15 animals, three biological replicates. (B) TEM micrographs showing gut of control(RNAi) and *hnf4(RNAi)* animals. 'mv' microvilli, 'ga' gastrodermis, 'L' lumen, 'em' enteric muscle. *n* = 4 parasites, two biological replicates. (C) Graph showing quantification of the number of microvilli per micron of gut surface from (B). Numbers are the average of four different sections of gut from each of four animals. (D-E) Stitched TEM micrographs from either control(RNAi) animals, or *hnf4(RNAi)* animals. *n* = 4 animals, two biological replicates. The number of parasites similar to representative images is indicated in the upper right of each panel. Nuclei: grey. Scale bars, A, 20 μm; B, D, E, 5 μm. * $p < 0.05$ (Welch's t-test).

Figure 6.5

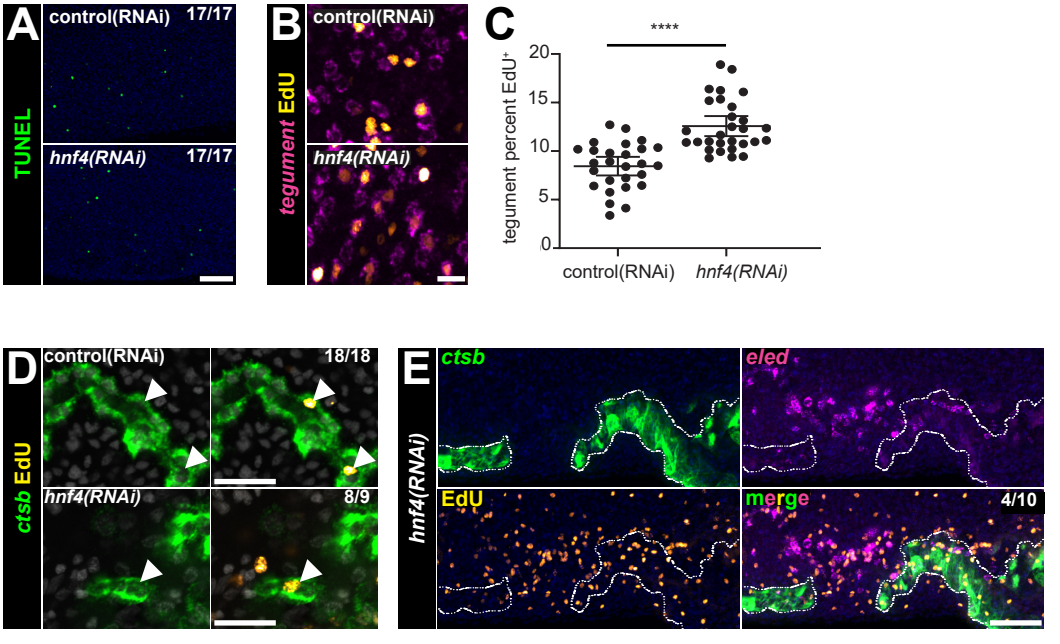
A
control(RNAi)
17/17
TUNEL
hnf4(RNAi)
17/17
B
control(RNAi)
tegument EdU
hnf4(RNAi)
C
****
tegument percent EdU+
20
15
10
5
0
control(RNAi)
hnf4(RNAi)
D
control(RNAi)
18/18
ctsb EdU
hnf4(RNAi)
8/9
E
ctsb
eled
hnf4(RNAi)
EdU
merge
4/10

FIGURE 6.5: hnf4 RNAi results in gut neoblast abnormalities.

(A) Fluorescent TUNEL experiment showing apoptotic cells (green) in either control RNAi or hnf4 RNAi conditions. *n* = 17 parasites, two biological replicates. (B) FISH with a pooled mix of four tegument-specific mRNAs (magenta) with detection of EdU after a 7-day pulse-chase showing the location of EdU^+ progeny cells (yellow) in either control RNAi or *hnf4* RNAi conditions. (C) Quantification of the percentage of tegument cells that are EdU^+ from (B). $n \geq 27$, three biological replicates. (D) FISH of the gut marker *ctsb* (green) with detection of EdU after a 7-day pulse-chase showing location of EdU^+ progeny cells (yellow) in either control RNAi or *hnf4* RNAi conditions. $n \geq 9$, two biological replicates. (E) Double FISH of the gut marker *ctsb* and *eled* with an EdU pulse showing the location of EdU^+ proliferative cells (yellow) in *hnf4* RNAi conditions. The dashed line indicates the approximate boundary of the residual gut-like tissue found in *hnf4(RNAi)* animals. The number of parasites similar to the representative image is indicated in the upper right of each panel. Nuclei: blue (A, B, E) or grey (D). Scale bars, A, E, 50 μm; B, 10 μm; D, 20 μm. **** $p < 0.0001$ (Welch's t-test).

Figure 6.6

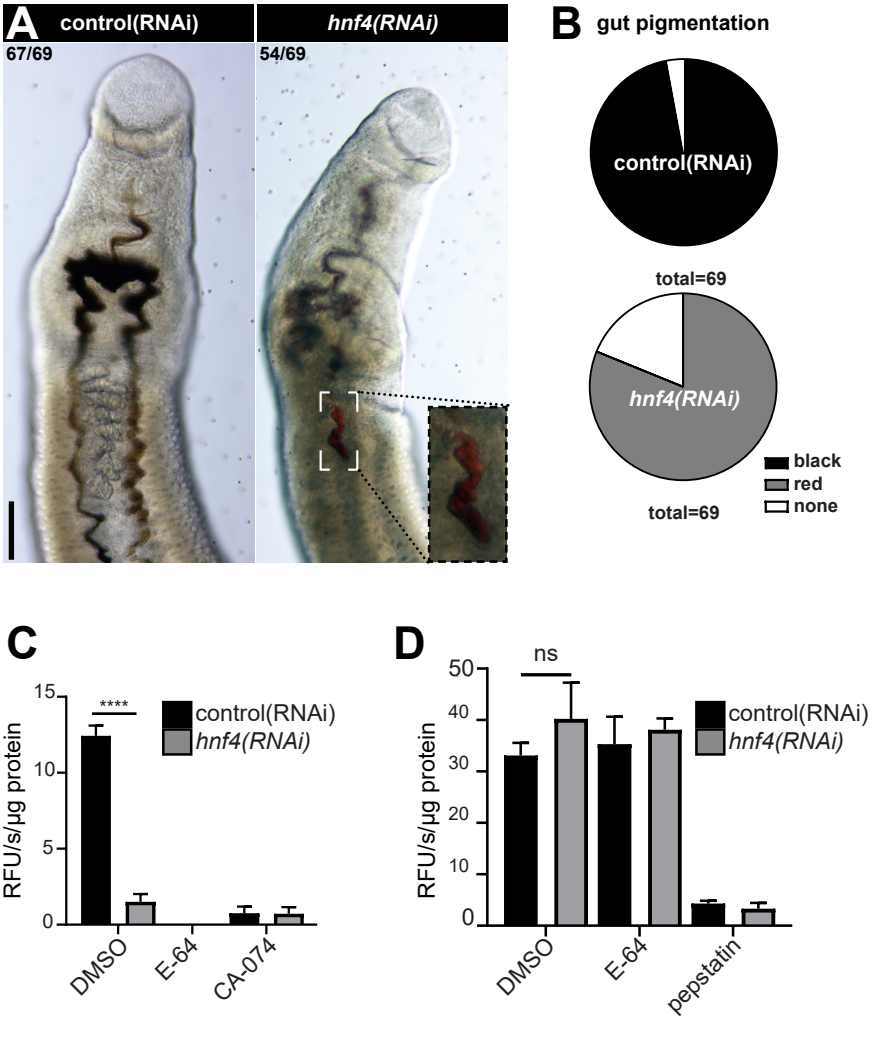
A
control(RNAi)
hnf4(RNAi)
67/69
54/69
B
gut pigmentation
control(RNAi)
total=69
hnf4(RNAi)
total=69
black
red
none
C
RFU/s/µg protein
15
10
5
0
****
control(RNAi)
hnf4(RNAi)
DMSO
E-64
CA-074
D
RFU/s/µg protein
50
40
30
20
10
0
ns
control(RNAi)
hnf4(RNAi)
DMSO
E-64
pepstatin

FIGURE 6.6: hnf4 is required for blood feeding.

(A) Brightfield images of control(RNAi) or *hnf4(RNAi)* animals cultured with red blood cells. Inset: magnification of boxed area. (B) Pie chart depicting the frequency of different gut pigmentation of animals from (A). *n* = 69 animals, three biological replicates. (C) Cathepsin activity of lysates from control(RNAi) or *hnf4(RNAi)* animals determined by cleavage of Z-FR-AMC with no inhibitor (DMSO), a broad cysteine protease inhibitor (E-64), or a cathepsin B-selective inhibitor (CA-074). *n* = 3, three biological replicates. (D) Graph of the aspartyl protease activity of lysates from control(RNAi) or *hnf4(RNAi)* parasites as determined by the ability to cleave the fluorogenic substrate, mca-GKPILFFRLK-K(dnp) in the presence of no inhibitor (DMSO), the general cysteine protease inhibitor E-64 (E-64), or the aspartyl protease inhibitor pepstatin A (pepstatin). Scale bars: 100μm.

Figure 6.7

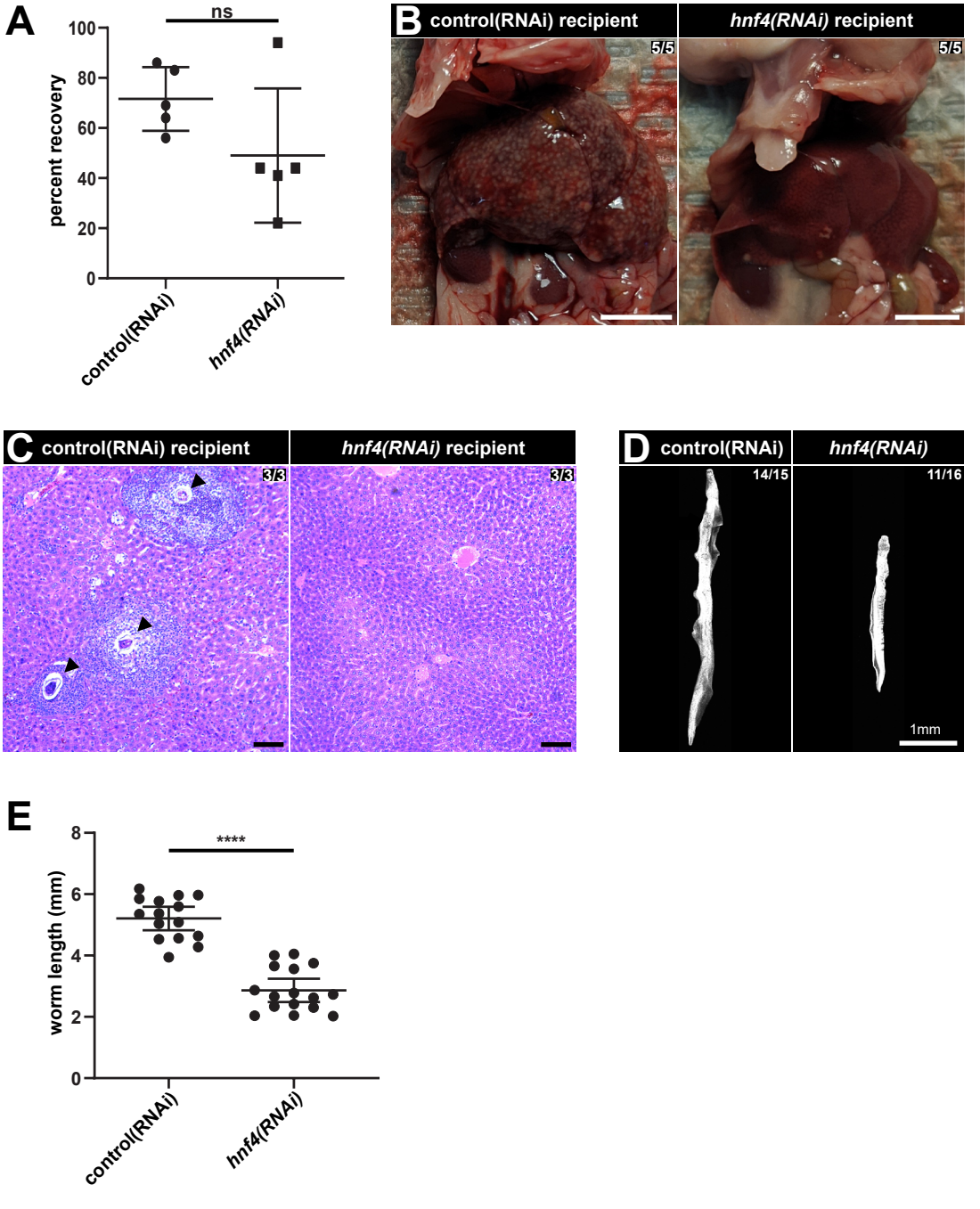
A
ns
100
80
60
40
20
0
percent recovery
control(RNAi)
hnf4(RNAi)
B
control(RNAi) recipient
hnf4(RNAi) recipient
5/5
5/5
C
control(RNAi) recipient
hnf4(RNAi) recipient
3/3
3/3
D
control(RNAi)
hnf4(RNAi)
14/15
11/16
1mm
E
****
8
6
4
2
0
worm length (mm)
control(RNAi)
hnf4(RNAi)

FIGURE 6.7: hnf4 is required for pathology.

(A) Graph quantifying the recovery rate of worms from transplant recipients. *n* = 5 recipients, two biological replicates. (B) Images of livers of mice 30 days after transplant with RNAi-treated parasites. *n* = 5 recipients, two biological replicates. (C), H&E-stained mouse liver sections 22 days post-transplant with RNAi-treated parasites. Arrows: granulomata. Sections from *n* = 3 recipients. (D) Parasites recovered from transplant recipients. *n* > 15 from three recipients. Nuclei: white. The number of mice/sections/parasites similar to the representative micrograph is in the upper left of each panel. (E) Graph showing quantification of male worm length from (D). *n* ≥ 15 animals, three separate recipients. Scale bars: B, 1 cm, C-D, 100μm. ns, not significant, **** $p < 0.0001$ (Welch's t-test).